

AWARD NUMBER: W81XWH-13-1-0193

TITLE: Clinical Development of Gamitrinib, a Novel Mitochondrial-Targeted Small Molecule Hsp90 Inhibitor

PRINCIPAL INVESTIGATOR: Dario C. Altieri

CONTRACTING ORGANIZATION: The Wistar Institute
Philadelphia, PA 19104

REPORT DATE: September 2016

TYPE OF REPORT: Annual

PREPARED FOR: U.S. Army Medical Research and Materiel Command
Fort Detrick, Maryland 21702-5012

DISTRIBUTION STATEMENT: Approved for Public Release;
Distribution Unlimited

The views, opinions and/or findings contained in this report are those of the author(s) and should not be construed as an official Department of the Army position, policy or decision unless so designated by other documentation.

REPORT DOCUMENTATION PAGE				Form Approved OMB No. 0704-0188	
Public reporting burden for this collection of information is estimated to average 1 hour per response, including the time for reviewing instructions, searching existing data sources, gathering and maintaining the data needed, and completing and reviewing this collection of information. Send comments regarding this burden estimate or any other aspect of this collection of information, including suggestions for reducing this burden to Department of Defense, Washington Headquarters Services, Directorate for Information Operations and Reports (0704-0188), 1215 Jefferson Davis Highway, Suite 1204, Arlington, VA 22202-4302. Respondents should be aware that notwithstanding any other provision of law, no person shall be subject to any penalty for failing to comply with a collection of information if it does not display a currently valid OMB control number. PLEASE DO NOT RETURN YOUR FORM TO THE ABOVE ADDRESS.					
1. REPORT DATE (DD-MM-YYYY) September 2016		2. REPORT TYPE Annual		3. DATES COVERED (From - To) 1 Sep 2015 – 31 Aug 2016	
4. TITLE AND SUBTITLE Clinical Development of Gamitrinib, a Novel Mitochondrial-Targeted Small Molecule Hsp90 Inhibitor				5a. CONTRACT NUMBER	
				5b. GRANT NUMBER W81XWH-13-1-0193	
				5c. PROGRAM ELEMENT NUMBER	
6. AUTHOR(S) Dario C. Altieri email: daltieri@wistar.org				5d. PROJECT NUMBER	
				5e. TASK NUMBER	
				5f. WORK UNIT NUMBER	
7. PERFORMING ORGANIZATION NAME(S) AND ADDRESS(ES) The Wistar Institute 3601 Spruce Street Philadelphia, PA 19104-4265				8. PERFORMING ORGANIZATION REPORT NUMBER	
9. SPONSORING / MONITORING AGENCY NAME(S) AND ADDRESS(ES) U.S. Army Medical Research and Materiel Command Fort Detrick, Maryland 21702-5012				10. SPONSOR/MONITOR'S ACRONYM(S)	
				11. SPONSOR/MONITOR'S REPORT NUMBER(S)	
12. DISTRIBUTION / AVAILABILITY STATEMENT Approved for public release; distribution is unlimited.					
13. SUPPLEMENTARY NOTES					
14. ABSTRACT The past funding cycle of the above-referenced award has supported important advances in each of the milestones and specific tasks set forth in the original SOW. Work carried out during the last budget period focused on three experimental directions towards the accomplishments of the original specific aims. First, considerable progress has been made in the full preclinical characterization of Gamitrinib in anticipation of IND filing and human testing. Specifically, ADME (adsorption, distribution, metabolism and excretion) studies and a complete plasma distribution and pharmacokinetics profile of Gamitrinib in rats have been obtained. Second, we expanded the safety characterization of Gamitrinib in vitro and in vivo, and completed a non-GLP, 7 day repeated-dose study of Gamitrinib intravenous administration to Sprague-Dawley rats and Beagle dogs. These studies demonstrated encouraging drug-like properties and a favorable safety profile for Gamitrinib in vivo, with no systemic or organ toxicity in two animal species. Third, molecular studies have been carried out to further the characterization of Gamitrinib mechanism of action, antitumor efficacy in combination regimens, and the underlying role of its target, namely mitochondrial protein folding quality control in tumor progression. Supported by the present award and published in the premiere, peer-reviewed literature (<i>JCI</i> , <i>PLOS Biol</i> and <i>Cancer Cell</i>), these studies further validated the role of mitochondrial Hsp90s as important therapeutic targets in cancer, and established Gamitrinib as a first-in-class, subcellularly-directed anticancer agent.					
15. SUBJECT TERMS Mitochondria, oxidative phosphorylation, Hsp90, advanced prostate cancer, Gamitrinib					
16. SECURITY CLASSIFICATION OF:			17. LIMITATION OF ABSTRACT UU	18. NUMBER OF PAGES 74	19a. NAME OF RESPONSIBLE PERSON USAMRMC
a. REPORT U	b. ABSTRACT U	c. THIS PAGE U			19b. TELEPHONE NUMBER (include area code)

TABLE OF CONTENTS

	Page
1. Introduction	1
2. Keywords	1
3. Accomplishments	1
4. Impact	9
5. Changes/Problems	10
6. Products	10
7. Participants & Other Collaborating Organizations	11
8. Special Reporting Requirements	12
9. Appendices	12

1. **INTRODUCTION.** The present research project is designed to obtain a complete preclinical characterization (formulation studies, pharmacokinetics analysis, toxicology profile and identification and validation of suitable biomarkers) of Gamitrinib (GAMITRINIB), a first-in-class, mitochondrial-targeted small molecule inhibitor of Heat Shock Protein-90 (Hsp90) chaperones present in mitochondria. Extensive preliminary data in support of the application have demonstrated that Gamitrinib has a unique mechanism of action, selectively accumulating in mitochondria and inhibiting the ATPase activity of a pool of the molecular chaperone Hsp90 and its homolog TRAP-1 (TNFR-Associated Protein-1, TRAP-1) localized within the mitochondrial inner membrane and matrix. In turn, this causes catastrophic loss of protein folding quality control in mitochondria, collapse of tumor bioenergetics, massive activation of apoptosis and potent cytotoxic anticancer activity as single-agent or in combination, in vivo. As Hsp90 chaperones are selectively enriched in mitochondria of tumors, as opposed to normal tissues, Gamitrinib has shown good tolerability in preclinical xenograft and genetic cancer models, in vivo. The overarching goal of the proposal is to complete the preclinical characterization of Gamitrinib and support filing of an Investigational New Drug (IND) Application with the US Food and Drug Administration (FDA). The long-term goal of the proposal is to bring Gamitrinib to the clinic as a conceptually novel, first-in-class anticancer agent with a unique mechanism of action suitable for therapy of patients with advanced, castrate-resistant and metastatic prostate cancer.

2. **KEYWORDS.** Mitochondria, oxidative phosphorylation, Hsp90, metabolomics, advanced prostate cancer, Gamitrinib.

3. **ACCOMPLISHMENTS.**
 - **What were the major goals of the project?**
Consistent with the original SOW of the application, studies carried out during the past budget cycle examined the safety and ADME properties of Gamitrinib (i), plasma distribution and pharmacokinetics profile of intravenous infusion of Gamitrinib in rats (ii), and non-GLP 7-day repeated-dose toxicology studies of Gamitrinib in Sprague-Dawley rats and Beagle dogs (iii). In all of these studies, Gamitrinib was formulated in a novel Lipoid S-100®-based formulation identified and characterized in the previous budget cycle. The new Lipoid S-100® formulation provided optimal solubility of Gamitrinib, fully retained anticancer activity, and achievable high stock concentrations. In addition, molecular studies, we continued our in-depth characterization of Gamitrinib, including its unique mechanism of anticancer activity, and rational combination regimens potentially suitable for clinical testing in humans.
 - **What was accomplished under these goals?**
 1. Major activities.
We completed ADME and safety studies of Gamitrinib with respect to plasma protein binding, inhibition of cytochrome (CYP) P450 isoforms, stability in liver microsomes, and Caco-2 permeability assays. In addition, we examined the safety of Gamitrinib in a CEREP 44 safety panel, analysis of a cardiac profiler in cultured cells and potential inhibition of hERG currents by patch clamp methods in transfected cells. As indicated in the 2016 quarterly report for this award, we identified an optimal Lipoid S-100®-based formulation of Gamitrinib. Using this formulation, we completed a pharmacokinetics and plasma distribution profile of intravenous infusion of Gamitrinib in Sprague-Dawley rats. Third, we completed a non-GLP, 7-day repeated dose study of intravenous administration of Gamitrinib solubilized in the new Lipoid S-100®-based formulation in Sprague-Dawley rats and Beagle dogs with analysis of body weight changes and clinical-chemistry parameters of organ function.
 2. Specific objectives.
The specific objectives of these experiments were as follows. (1) **Establish the ADME and in vitro safety profile of Gamitrinib.** These studies were carried out using a combination of approaches to characterize the drug-like properties and preliminary safety of Gamitrinib in vitro and in vivo cell lines. (2) **Determine the complete pharmacokinetics and plasma distribution profile of intravenous administration of Gamitrinib.** The use of our novel, Lipoid S-100®-based formulation of Gamitrinib that provided complete drug solubilization, high stock concentrations, and fully retained anticancer activity enabled a detailed pharmacokinetics and plasma distribution profile of intravenous administration of Gamitrinib in rats. (3) **Non-GLP toxicology studies of Gamitrinib.** Utilizing the novel, Lipoid S-100®-based formulation, we carried out non-GLP, 7-day repeated dose studies of intravenous infusion of Gamitrinib in two animal species for a comprehensive evaluation of systemic toxicity and clinical chemistry parameters of organ function.

3. Significant Results.

- (1) **Establish the ADME and in vitro safety profile of Gamitrinib.** The following in vitro ADME studies addressing Cytochrome (CYP) 450 isoform inhibition, plasma protein binding, stability in human liver microsomes, and Caco-2 permeability were carried out to characterize the physico-chemical properties of Gamitrinib. To establish preliminary cardiac safety, Gamitrinib was evaluated for potential inhibition of relevant ion channel activities and of hERG currents in transfected cells by patch-clamp methods.

1.1. Cytochrome (CYP) P450 isoform inhibition.

At a concentration of 10 μ M Gamitrinib is not a significant inhibitor of CYP isoforms 1A2, A26, 2B6, 2C8, 2C9, 3A4, 3A4i, compared to the respective positive controls (Table 1). The positive controls used for each CYP substrate (in parenthesis) were Phenacetin (CYP1A2), Coumarin (CYP2A6), Bupropion (CYP2B6), Paclitaxel (CYP2C8), Diclofenac (CYP2C9), Midazolam (CYP3A4), and Testosterone (CYP3A4).

Table 1. CYP isoform inhibition. Data are expressed as IC₅₀ concentrations (μ M) for both Gamitrinib and the relevant positive control.

Compound	CYP1A2	CYP2A6	CYP2B6	CYP2C8	CYP2C9	CYP3A4	CYP3A4
Gamitrinib	32.96	25.48	18.07	8.77	1.09	0.15	0.27
Control	0.06	0.02	0.02	1.20	0.13	0.01	0.01

1.2. Plasma protein binding.

Gamitrinib is bound to plasma proteins by 99.3% with a recovery of 82.6% (Table 2).

Table 2. Gamitrinib binding to human plasma proteins.

Compound	Human Plasma % Bound	Human Plasma % Free Fraction	Human Plasma % Recovery	Replicates
Gamitrinib	99.3	0.70	82.6	n=3
Warfarin	98.32	1.68	88.38	n=3

1.3. Stability of Gamitrinib in human liver microsomes.

Gamitrinib has an intrinsic clearance (CL_{int}) from human liver microsomes of 3.3 ml/min/g of liver tissue, with an elimination rate constant of 0.0415 and a half-life (t_{1/2}) of 16.7 min (Table 3).

Table 3. Stability of Gamitrinib in human liver microsomes.

Compound	Elimination Rate Constant (k)	Half-life (t _{1/2}) (min)	Intrinsic Clearance (CL _{int}) (ml/min/g liver)
Gamitrinib	0.0415	16.7	3.30
Midazolam	0.0407	17.0	3.23

1.4. Caco-2 permeability assay.

Gamitrinib shows poor permeability across a continuous monolayer of Caco-2 cells with a P_{app}, A>B of 1.90 nm/sec, a P_{app}, B>A of 10.94 nm/sec and a P_{app} Efflux Ratio of 5.77 (Table 4).

Table 4. Permeability of Gamitrinib across a monolayer of Caco-2 cells.

Compound	P _{app} , A>B (nm/sec)	P _{app} , B>A (nm/sec)	P _{app} Efflux Ratio
Gamitrinib	1.90	10.95	5.77
Propranolol	186.12	162.49	0.87
Digoxin	5.47	114.80	21.0

1.5. Effect of Gamitrinib on cardiac ion channel activity (cardiac profiling)

Gamitrinib was tested in a cardiac profiling experiment to examine a potential inhibitory effect on ion channel activity relevant to heart conduction. In these studies, Gamitrinib (10 μ M) caused limited or negligible inhibition of Nav1.5, Kv4.3/KChIP2, Cav1.2, Kv1.5, KCNQ1/mink1, HCN4, and Kir2.1 (Table 11). At the same concentration of 10 μ M, Gamitrinib inhibited hERG channel activity by 37.9 \pm 1.7% (Table 5).

Table 5. Effect of Gamitrinib (% inhibition) on cardiac ion channel activity. Gamitrinib was used at 10 μ M in all assays.

Ion Channel	Nav1.5	Kv4.3	Cav1.2	Kv1.5	KCNQ1	hERG	HCN4	Kir2.1
Gamitrinib	22.3 \pm 4.3 N=6	6.8 \pm 2.2 N=8	12.2 \pm 1.5 N=8	6.6 \pm 1.3 N=8	22.5 \pm 1.1 N=8	37.9 \pm 1.7 N=8	-0.2 \pm 3.7 N=8	-7.3 \pm 3.4 N=8

1.6. Effect of Gamitrinib on hERG currents by patch clamp quantification.

Benzoquinone ansamycin antibiotics, including 17-AAG may inhibit hERG channel function. In the ion channel cardiac profiler presented in Table 5, Gamitrinib at 10 μ M inhibited hERG activity by 37%. To investigate this potential activity further, the effect of Gamitrinib on hERG currents was examined in transfected human cells by patch clamp methods. In these studies, Gamitrinib inhibited hERG currents with IC₅₀ of 3582 nM, compared to IC₅₀ of 21 nM of positive control, Terfenadine (Fig. 1).

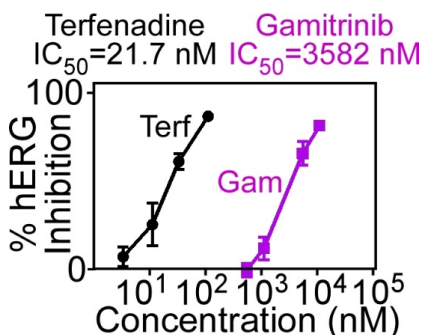


Figure 1. Effect of Gamitrinib or Terfenadine (positive control) on hERG currents. Cells transfected with hERG were exposed to the indicated, increasing concentrations of Gamitrinib or positive control Terfenadine and evaluated for hERG currents (n=6) by patch clamp methods. Data are mean \pm SEM. The IC₅₀ concentrations for both drugs are indicated.

- (2) **Determine the complete pharmacokinetics and plasma distribution profile of intravenous administration of Gamitrinib.** For these experiments, non-GLP grade Gamitrinib was solubilized in the new, Lipoid S-100®-based formulation and injected intravenously (5 mg/kg as bolus administration) in Sprague-Dawley rats (n=3) with determination of plasma distribution and complete pharmacokinetics profile using validated LC/MS detection methods.

2.1. Gamitrinib plasma distribution in rats.

The plasma concentrations of Gamitrinib (Table 6) were quantified at increasing time intervals between 0.083 and 24 h after intravenous injection using validated LC/MS methods (n=3).

Table 6. Plasma distribution after IV administration of Gamitrinib (5 mg/kg) in rats.

Time (h)	Concentration (ng/ml)			Mean	SD	CV (%)
	Rat 1	Rat 2	Rat 3			
0.083	622.199	526.229	674.432	607.620	75.16	12.4
0.25	180.951	211.686	211.686	173.767	41.97	24.2
0.5	106.381	114.230	114.230	95.938	25.19	26.3
1	71.445	65.903	65.903	64.446	7.82	12.1
2	46.657	43.125	43.125	39.889	8.82	22.1
4	36.816	34.776	34.776	33.499	4.10	12.3
24	11.946	10.511	10.511	10.941	10.94	8.0

2.2. Gamitrinib pharmacokinetics profile in rats.

The PK parameters of Gamitrinib administered intravenously at 5 mg/kg in Sprague-Dawley rats is presented in Table 7. Using a 2-compartment model, Gamitrinib has an average AUC of 976 ng*h/ml, a t_{1/2} of 12.2 \pm 1.5 h, excellent distribution with a steady-state volume of distribution of 65.4 L/Kg, and a medium to slow clearance of 85.6 ml/min/Kg (Table 7). Importantly, the metabolism of Gamitrinib in vivo differed from that of 17-AAG, as there was no generation of the metabolite 17-allylgeldanamycin (17-AG) at any time point after IV administration in rats.

Table 7. PK parameters of Gamitrinib after i.v. infusion (5 mg/kg) in Sprague-Dawley rats.

	$t_{1/2}$ (h)	C ₀ (ng/ml)	AUC _{Last} (ng*h/ml)	AUC _{Inf} (ng*h/ml)	AUC Extr (%)	V _z (L/Kg)	V _{ss} (L/Kg)	CL (ml/min/Kg)	MRT (h)
Mean	12.2	1175.8	783.1	976.0	19.8	91.11	65.4	85.6	5.49
SD	1.55	357.6	71.3	68.3	2.69	6.5	11.0	5.85	0.07
CV	12.7	30.4	9.1	7.0	13.6	18.1	16.8	6.8	1.3

The PK profile of Gamitrinib after IV infusion in Sprague-Dawley rats is shown in Figure 2.

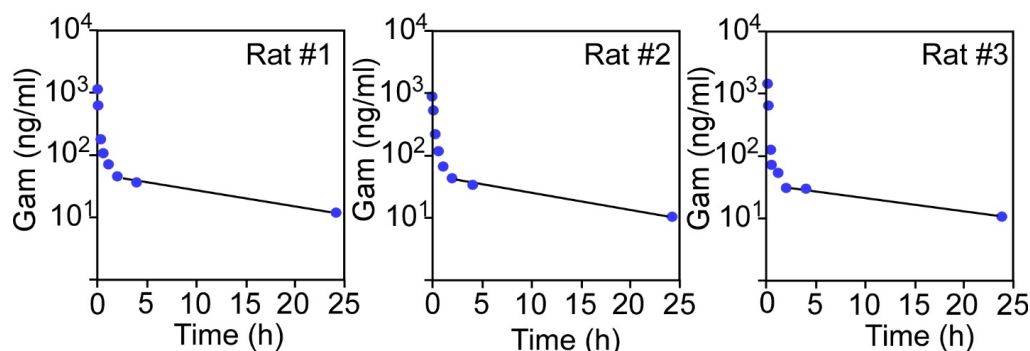


Figure 2. PK profile of Gamitrinib in after IV administration (5 mg/kg). Gamitrinib was solubilized in the new Lipoid S-100®-based formulation and injected intravenously in Sprague-Dawley rats (n=3). Gamitrinib concentrations were quantified at the indicated time intervals after infusion using validated LC/MS methods. Data are analyzed using a two-compartment model.

- (3) **IND-directed non-GLP toxicology studies of Gamitrinib in two animal species.** Gamitrinib was evaluated in a non-GLP 7-day repeated dose toxicology study by intravenous injection (IV) in Sprague-Dawley rats and Beagle dogs. For these studies, Gamitrinib was solubilized in the new Lipoid S-100®-based formulation and administered IV every other day (day: 1, 3, 5 and 7) as a 30-min infusion at a rate of 0.1 ml/min. The protocol for Beagle dogs included a pre-medication safety step with IV administration of Diphenhydramine (0.2 ml, 50 mg/ml) immediately before Gamitrinib infusion. The individual dose levels and animal groups are shown in Table 8. The dose of Gamitrinib of 5 mg/kg (rats) or 1.25 mg/kg (dogs) corresponds to therapeutically active doses (7.5-10 mg/kg) that inhibit xenograft tumor growth in mice.

Table 8. Dose levels in non-GLP 7-day repeated-dose studies of Gamitrinib IV administration in two animal species.

Animal Species	Gamitrinib dose (mg/kg/i.v.)
Sprague-Dawley Rats	
Group 1	No Treatment -Lipoid S-100® formulation
Group 2	1 mg/kg
Group 3	5 mg/kg (<i>therapeutically active dose in xenograft</i>)
Beagle Dogs	
Group 1	No Treatment - Lipoid S-100® formulation
Group 2	0.25 mg/kg
Group 3	1.25 mg/kg (<i>therapeutically active dose in xenograft</i>)

The results of these studies demonstrated that IV administration of Gamitrinib in two animal species was feasible, and devoid of systemic or organ toxicity. Animals were inspected twice daily according to protocol specifications, and exhibited no changes in behavior, gait, activity or food intake. Gamitrinib treatment did not affect body weight or parameters of kidney, liver, coagulation or bone marrow function. The electrolytes and metabolic profiles in the various animal groups were unremarkable. There were no animal deaths or unscheduled euthanasia in any of the treatment groups. Necropsies performed at the end of the experiments showed no findings in either animal species in the various groups.

A summary of the clinical-chemistry and metabolic parameters of a 7-day non-GLP repeated dose study of intravenous infusion of Gamitrinib in Sprague-Dawley rats is shown in Figure 3. As shown in Figure 3, Gamitrinib treatment did not affect animal body weight (Figure 3A) or clinical chemistry parameters of kidney function (Figure 3B), liver function (Figure 3C), metabolism (Figure 3D), and bone marrow and coagulation function (Figure 3E). In this study, the Gamitrinib dose of 5 mg/kg was considered the No Observed Adverse Event Level (NOAEL).

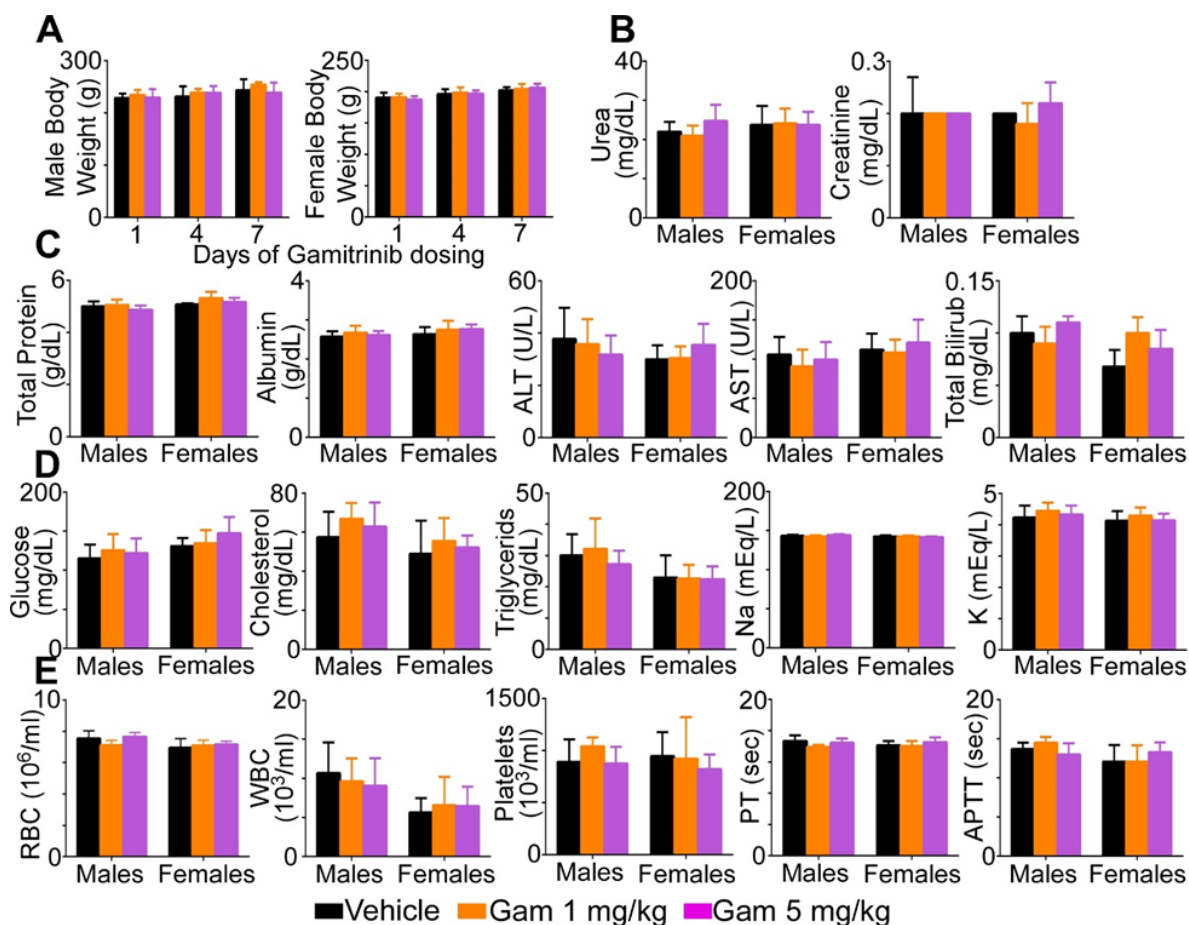


Figure 3. A 7-day non-GLP repeated-dose study of intravenous administration of Gamitrinib to Sprague-Dawley rats. The individual treatment groups are indicated. Animals were inspected for changes in body weight (A) as well as clinical-chemistry parameters of kidney function (B), liver function (C), metabolism (D), and bone marrow and coagulation function (E).

A summary of the clinical chemistry and metabolic parameters of a 7-day non-GLP repeated dose study of intravenous infusion of Gamitrinib in Beagle dogs is shown in Figure 4. In this study, the Gamitrinib dose of 1.25 mg/kg was considered the No Observed Adverse Event Level (NOAEL).

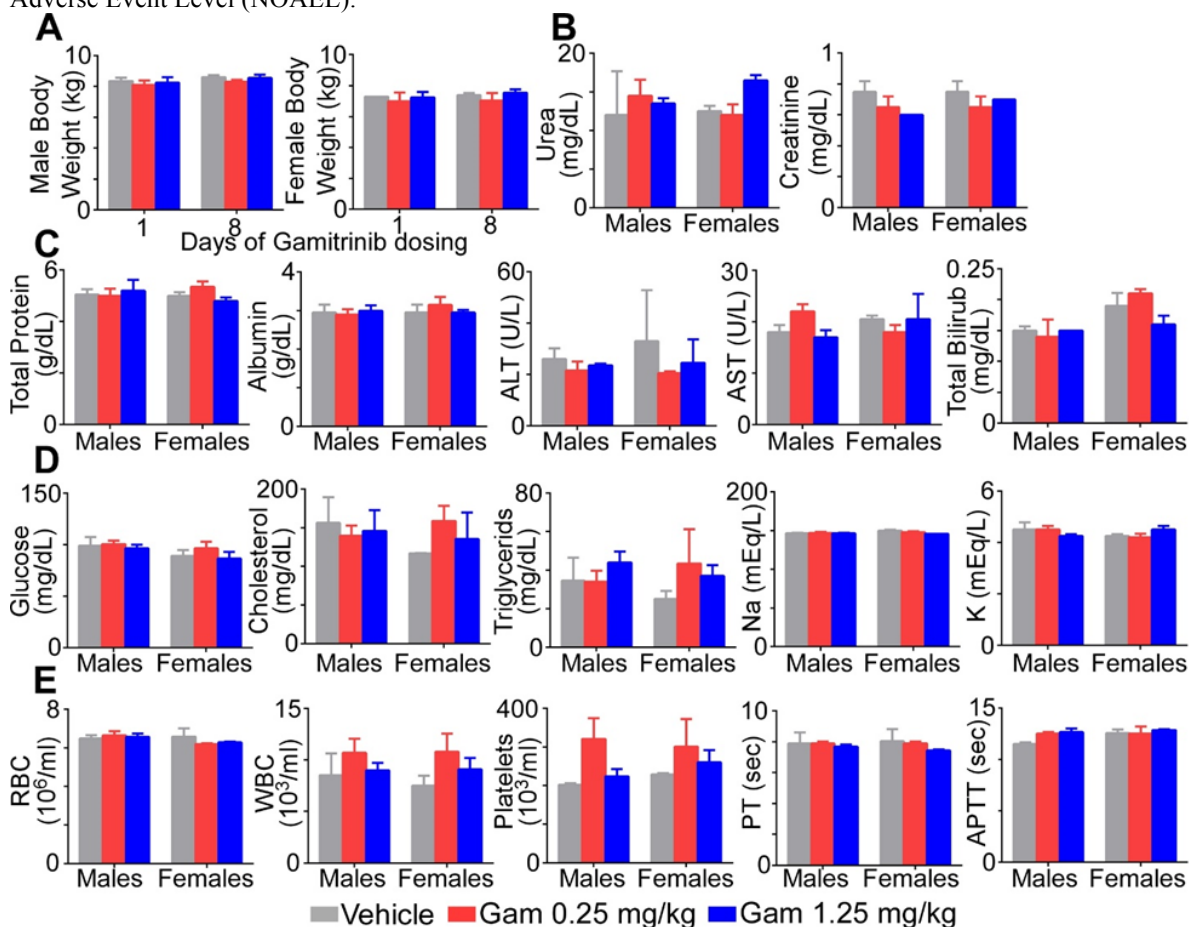


Figure 4. A 7-day non-GLP repeated-dose study of intravenous administration of Gamitrinib to Beagle dogs. The individual treatment groups are indicated. Animals were inspected for changes in body weight (A) and clinical-chemistry parameters for kidney function (B), liver function (C), metabolism (D), and bone marrow and coagulation function (E).

4. Other Achievements.

Consistent with the objective of the present application to bring Gamitrinib to the clinic, we carried out parallel molecular studies to characterize the Gamitrinib pathway in cancer and its requirement for tumor maintenance and progression. In a first set of experiments, we explored the impact of mitochondrial bioenergetics in mechanisms of cancer drug resistance. For these studies, we focused on a model of BRAF V600E mutant melanoma, a condition frequently associated with tumor dormancy and high metastatic propensity. We found that melanoma cell types exploit mitochondrial biogenesis, an intrinsic cellular stress response and increased mitochondrial oxidative phosphorylation to become resistant to small molecule inhibitors of MAPK (*Zhang et al J Clin Invest, 2016*). Conversely, treatment of these cells with Gamitrinib suppressed oxidative phosphorylation, blocked tumor bioenergetics, inhibited mitochondrial biogenesis and potently synergized with MAPK inhibitors to produce enhanced anticancer activity in xenograft disease models (*Zhang et al J Clin Invest, 2016*). These results extend our previous findings that Gamitrinib synergizes with small molecule PI3K inhibitors in eradicating genetically heterogeneous tumors, and opens the possibility of novel drug combination regimens of Gamitrinib plus MAPK inhibitors for the targeting of drug-resistant and metastatic tumors in the clinic.

In a second series of experiments, we set up a high-throughput proteomics screen to identify novel regulators of mitochondrial protein folding quality control, which is the target of Gamitrinib in tumors. In these studies, we isolated ClpP, a subunit of the mitochondrial protease complex, ClpXP as a novel molecule implicated in mitochondrial bioenergetics and tumor maintenance (*Seo et al PLoS Biol, 2016*). Structurally a member of the AAA+ proteases, ClpXP has been implicated in protein folding quality control in mitochondria via proteolytic removal of misfolded or aggregated proteins. Consistent with the results of our proteomics screen, we identified a novel role of ClpXP in regulating the stability and function of mitochondrial oxidative phosphorylation Complex II subunit, SDHB in tumor cells. Functionally, defects in SDHB folding due to ClpXP targeting impaired oxidative phosphorylation, reduced overall ATP production and activated stress signals of cellular starvation and autophagy in tumor cells. In addition, ClpXP depletion caused oxidative stress in tumor cells with increased mitochondrial production of toxic superoxide. In turn, this inhibited tumor cell proliferation, suppressed cell motility, and blocked disease dissemination in a liver metastasis model, in vivo. Conversely, addition of mitochondrial-targeted antioxidants restored tumor cell proliferation and invasion under conditions of ClpXP targeting (*Seo et al PLoS Biol, 2016*). Analysis of public databases, as well as primary tumor samples, revealed that ClpXP was ubiquitously upregulated in disparate human cancers, correlating with shortened overall patient survival (*Seo et al PLoS Biol, 2016*).

Finally, we studied mitochondrial mechanisms of tumor adaptation in response to stress conditions of the microenvironment, and we focused on hypoxia as an important driver of more aggressive disease traits. In these experiments, we found that exposure of tumor cells to severe hypoxia (0.5% O₂ for 24-48 h) resulted in recruitment of active, i.e. Ser473-phosphorylated Akt to mitochondria. The requirements of this pathway were elucidated, and involved the production of reactive oxygen species by hypoxic tumor cells, and Hsp90-dependent mitochondrial pre-protein import (*Chae et al Cancer Cell, 2016*). Based on these results, we next carried out a genome-wide, state-of-the-art SILAC proteomics screening to identify phosphorylation changes in the mitochondrial proteome between normoxic and hypoxic conditions. We found that tumor cells exposed to hypoxia exhibited a discrete Akt gene signature in mitochondria, which included the pyruvate dehydrogenase kinase-1 (PDK1) as a novel Akt phosphorylation substrate. Using a collection of biochemical approaches, we demonstrated that mitochondrial Akt phosphorylates PDK1 on a novel Thr346 site, in vivo, resulting in downstream phosphorylation and inhibition of its substrate, the pyruvate dehydrogenase complex (PDC). Consistent with these findings, activation of Akt-PDK1 signaling in hypoxia shut down oxidative phosphorylation in favor of glycolysis, prevented the induction of apoptosis, and dampened oxidative stress associated with a defective mitochondrial electron transport chain. Functionally, this pathway sustained continuous tumor cell proliferation in face of severe hypoxia, and Akt phosphorylation of PDK1 specifically “marked” mitotic cells in the context of intracranial glioblastoma (GBM) in mouse models as well as primary human specimens (*Chae et al Cancer Cell, 2016*). To map the implications of this pathway in vivo, we next generated an antibody to Thr346 phosphorylated PDK1, and examined a large cohort of primary GBM tumors. In this retrospective study, Akt-phosphorylated PDK1 segregated with other markers of aggressive disease in human GBM samples, including unmethylated MGMT promoter, wild type IDH1 status, and increased HIF1 α expression, correlating with shortened overall survival in patient cohorts (*Chae et al Cancer Cell, 2016*).

- **What opportunities for training and professional development has the project provided?**

The present application is not designed to provide a training and professional development environment. Nothing to report.

- **How were the results disseminated to communities of interest?**

The mechanistic studies on the further characterization of Gamitrinib anticancer activity have been published in the premiere, peer-reviewed literature (*J Clin Invest* 126:1384-1356, 2016; *PLoS Biol* 14(7):e1002507. doi: 10.1371/journal.pbio.1002507; *Cancer Cell* 30:257-272).

- **What do you plan to do during the next reporting period to accomplish the goals?**

Based on the significant advances of the past budget cycle, new experiments are proposed for the next budget period to complete the IND-directed toxicology evaluation of Gamitrinib in two animal species. These studies will involve a 28-day GLP study of twice weekly intravenous administration of Gamitrinib to Sprague-Dawley rats or Beagle dogs with 14-day recovery period (rodents). The proposed protocol for the studies in rats is summarized in Table 9 and will include a higher dose of Gamitrinib of 10 mg/kg twice weekly (group 4) for potential identification of maximum tolerated dose (MTD).

Table 9. A 28-day GLP study of IV Gamitrinib in rats with 14-day recovery period.

Group No.	Test Material	Dose Level (mg/kg/day)	Dose Volume (mL/kg)	Dose Concentration (mg/mL)	Number of Animals			
					Main Study		Recovery Study	
					Males	Females	Males	Females
1	Control Article	0	5	0	10	10	5	5
2	Gamitrinib	1	5	0.2	10	10	0	0
3	Gamitrinib	5	5	1	10	10	0	0
4	Gamitrinib	10	5	2	10	10	5	5

Group No.	Test Material	Dose Level (mg/kg/day)	Dose Volume (mL/kg)	Dose Concentration (mg/mL)	Number of Animals	
					Toxicokinetic Study	
					Males	Females
1	Control Article	0	5	0	3	3
2	Gamitrinib	1	5	0.2	9	9
3	Gamitrinib	5	5	1	9	9
4	Gamitrinib	10	5	2	9	9

For these experiments, test and control articles will be administered via IV injection using an infusion pump (target at least 30 minutes, the actual start and stop times of dose administration will be recorded in the study record) to the cannula twice weekly from days 1 to 29 (e.g., days 1, 4, 8, 11, 15, 18, 22, 25, 29). In the event that a cannula is no longer exteriorized, dose administration will be via intravenous injection to the tail vein. The change in the dose administration site will be documented in the study records. The dose volume for each animal will be based on the most recent body weight measurement. The first day of dosing will be designated as Day 1 (exception: alternate animals used for replacement after Day 1 will assume the day of the animal being replaced). The dosing formulations will be stirred continuously during dose administration.

The experimental protocol for the planned GLP studies of Gamitrinib IV administration in Beagle dogs is summarized in Table 9.

Table 9. A 28-day GLP study of IV Gamitrinib in Beagle dogs.

Group No.	Test Material	Dose Level (mg/kg/day)	Dose Volume (mL/kg)	Dose Concentration (mg/mL)	Number of Animals			
					Main Study		Recovery Study	
					Males	Females	Males	Females
1	Control Article	0	5	0	3	3	2	2
2	Gamitrinib	0.25	5	0.05	3	3	0	0
3	Gamitrinib	1.25	5	0.25	3	3	0	0
4	Gamitrinib	3.33	5	0.67	3	3	2	2

The test and control articles will be administered via IV infusion twice weekly from days 1 to 29 (e.g., days 1, 4, 8, 11, 15, 18, 22, 25, 29) into a suitable peripheral vein using an infusion pump connected to a temporary indwelling catheter followed by a 0.9% sodium chloride injection flush of 0.5 mL (target 30 minutes, the actual start and stop times of dose administration will be recorded in the study record). The saphenous vein may be used for dosing, if necessary. The dose volume for each animal will be based on the most recent body weight measurement. The animals will be temporarily restrained for dose administration and will not be sedated. The first day of dosing will be designated as Day 1 (exception: alternate animals used for replacement after Day 1 will assume the day of the animal being replaced). As a premedication step, diphenhydramine will be administered pre-treatment (intravenous 0.2 mL, 50 mg/mL with a 0.5 mL saline flush before and after) to limit potential pseudoallergic reaction(s). The dosing catheter may be used for this injection. It may also be administered post-treatment if injection site reactions warrant. The decision to administer diphenhydramine post-treatment will be made by the Study Director in conjunction with the veterinary staff. Dosing occasions, dose volumes, and lot number information will be maintained in the study records.

Dosing holidays may be given as warranted by clinical signs, body weight losses, or other indications of severe toxicity. The duration of any dosing holiday and the animal(s) affected will be documented in the study records.

4. IMPACT

- **What was the impact on the development of the principal disciplines of the project?**

The studies summarized above had considerable impact on the principal disciplines of the project. First, we completed an extensive, detailed ADME and safety profile of Gamitrinib. In anticipation of IND filing, these studies demonstrated that Gamitrinib has encouraging drug-like properties, is not a significant inhibitor of the main detoxification system in humans (CYP isoforms) is highly bound to plasma proteins and has negligible intestinal absorption, further validating the proposed intravenous form of administration in humans. Using a combination of cardiac profiling studies and direct patch clamp experiments in transfected cells, we further ruled out that Gamitrinib is a meaningful inhibitor of hERG channel function as well as other cardiac ion channels, reducing the risk of QT syndrome in humans. The development of a new, non-toxic Lipoid S100®-based formulation of Gamitrinib proved instrumental in the further preclinical characterization of this agent, in vivo. As anticipated in the 2015 progress report for this award, our formulation development studies identified an optimal solubilization strategy for Gamitrinib based on a Lipoid S100® emulsificant. Studies conducted during the last budget cycle validated this approach and demonstrated that Lipoid S100®-based formulation of Gamitrinib is non-toxic, enables high stock concentrations of the agent, reduces the concentration of DMSO in the drug solution from 75% to 2%, and provides fully retained anticancer activity against different tumor types. Using the Lipoid S100® formulation, we reached a comprehensive plasma distribution and pharmacokinetics profile of intravenous administration of Gamitrinib in rats. These studies confirmed the favorable drug-like properties of Gamitrinib, and, importantly, uncovered a much longer half-life ($t_{1/2}$) of this agent than 17-AAG (approximately 12 h). In addition, these studies, demonstrated that the metabolism of Gamitrinib differs radically from that of 17-AAG, as there is no generation of the active metabolite, 17-AG at any time after IV administration of Gamitrinib to rats. This unique metabolic profile may reduce drug-drug interactions in vivo, and prevent the fast clearance that is typical of 17-AAG. Finally, we demonstrated that intravenous administration of Gamitrinib in the new Lipoid S100®-based formulation to two animal species (Sprague-Dawley rats and Beagle dogs) is feasible, with no weight loss or other signs of systemic or organ toxicity.

- **What was the impact on other disciplines?**

The results summarized above had significant impact for other disciplines, in particular for two areas of basic and translational cancer research: (1) The validation of the mitochondrial pool of Hsp90 as a novel, drugable cancer therapeutic target, and, (2) the preclinical development of Gamitrinib as a first-in-class, *subcellularly-directed* anticancer agent. Despite considerable expectations, the clinical experience with chemically diverse small molecule Hsp90 inhibitors has been disappointing. Tested in a large number of phase I and phase II trials, administration of single-agent 17-AAG, or several others, non-GA-based Hsp90 inhibitors was feasible, but produced limited to no clinical benefit, with stable disease in a small number of patients as often the best response. Most combination trials of Hsp90 therapy plus cytotoxics or targeted agents have been equally disappointing, falling short of their endpoints, and carrying significant toxicities, including treatment-related deaths. The identification of a mitochondrial-localized pool of Hsp90 essential for tumor maintenance together with the observation that none of the Hsp90 inhibitors currently in the clinic has the ability to accumulate in mitochondria may explain these negative results in the clinic. Instead, Gamitrinib has been engineered to selectively target the mitochondrial pool of Hsp90 for cancer therapeutics. Accordingly, Gamitrinib has a first-in-class combinatorial structure containing the Hsp90 ATPase inhibitory backbone of 17-AAG coupled to the mitochondrial-targeted moiety of triphenylphosphonium. Although the subcellular delivery of antioxidants inside mitochondria has long been proposed as therapy for cardiovascular diseases, the idea that a similar approach could be pursued or even considered for cancer therapy has not, to the best of our knowledge, previously considered. As summarized in this progress report, the synthesis and preclinical characterization of Gamitrinib validates this tenet, and brings to the forefront a novel approach of *subcellularly-targeted, organelle-directed* cancer drug discovery. Despite its ability to disable multiple, fundamental mechanisms of tumor cell proliferation, survival and bioenergetics, Gamitrinib therapy is well tolerated, in vivo, reflecting a unique wiring of this pathway in tumors, and anticipating a promising therapeutic window for use in humans. The results presented here validate these observations, and demonstrate that Gamitrinib has encouraging drug-like properties, a favorable safety profile and could be administered to two animal species with no signs of systemic or organ toxicity. Taken together, these findings reinforce the uniqueness of Gamitrinib as a novel therapeutic agent unlike any other Hsp90 inhibitor or anticancer drug previously developed.

- **What was the impact on technology transfer?**

The Gamitrinib development program is currently protected by one issued composition of matter patent and two other submitted patent applications. There has been no additional patent filing during the past budget period.

- **What was the impact on society beyond science and technology?**

These studies may open new, concrete prospect for the management of patients with advanced prostate cancer. Although early-stage prostate cancer is successfully managed and these patients are offered a range of options, more advanced disease settings carry significant morbidity and mortality due to disease dissemination to bones and visceral organs, with limited, if any, meaningful therapeutic options. The identification of a novel mechanism of *spatiotemporal* mitochondrial bioenergetics that supports metastasis, and the characterization of Gamitrinib as an inhibitor of multiple pathways of tumor maintenance orchestrated in mitochondria, suggests a novel therapeutic strategy of simultaneously disrupting multiple key

pathways of tumor cell proliferation, survival and bioenergetics, in patients with advanced, castrate-resistant and metastatic prostate cancer.

5. CHANGES/PROBLEMS.

- **Changes in approach and reasons for change.**

We do not expect problems or deviations in protocol to complete the IND-enabling characterization of Gamitrinib during the next budget cycle. The 28-day toxicology studies in two animal species planned for the next budget cycle build on the successful experience with the non-GLP studies where intravenous administration of Gamitrinib was feasible, and without signs of organ or systemic toxicity. As the chemical synthesis and quality control evaluation of Gamitrinib is under fee-for-service contract with Albany Molecular Research International (AMRI), we also do not expect problems or delays in the production and characterization of GLP-grade Gamitrinib for these studies. Finally, we do not anticipate problems or delays in preparing the required documentation of the preclinical development of Gamitrinib for regulatory review by the US FDA in support of the proposed, first-in-human clinical trial of Gamitrinib in patients with advanced cancer.

- **Actual or anticipated problems or delays and actions or plans to resolve them.**

We do not anticipate problems or delays in completing the planned 28-day toxicology studies of Gamitrinib formulated in the new Lipoid S100®-based formulation in two animal species.

- **Changes that had a significant impact on expenditures.**

None reported

- **Significant changes in use or care of human subjects, vertebrate animals, biohazards, and/or select agents.**

None reported

6. PRODUCTS

- **Publications, conference papers, and presentations**

Journal Publications

1. Zhang, G., Frederick, D. T., Wu, L., Wei, Z., Krepler, C., Srinivasan, S., Chae, Y. C., Xu, X., Choi, H., Dimwamwa, E., Ope, O., Shannan, B., Basu, D., Zhang, D., Guha, M., Xiao, M., Randell, S., Sproesser, K., Xu, W., Liu, J., Karakousis, G. C., Schuchter, L. M., Gangadhar, T. C., Amaravadi, R. K., Gu, M., Xu, C., Ghosh, A., Xu, W., Tian, T., Zhang, J., Zha, S., Liu, Q., Brafford, P., Weeraratna, A., Davies, M. A., Wargo, J. A., Avadhani, N. G., Lu, Y., Mills, G. B., Altieri, D. C., Flaherty, K. T., and Herlyn, M. (2016) Targeting mitochondrial biogenesis to overcome drug resistance to MAPK kinase inhibitors. *J Clin Invest* 126:1384-1356. PMCID: PMC4855947.
2. Seo, J. H., Rivadeneira, D. B., Caino, M. C., Chae, Y. C., Speicher, D. W., Tang, H.-Y., Vaira, V., Bosari, S., Palleschi, A., Rampini, P., Kossenkov, A. V., Languino, L. R., and Altieri, D. C. (2016) The mitochondrial unfoldase-peptidase complex ClpXP controls bioenergetics stress and metastasis. *PLoS Biol* 14(7):e1002507. doi: 10.1371/journal.pbio.1002507. PMID 27389535. PMCID In Progress.
3. Chae, Y. C., Vaira, V., Caino, M. C., Tang, H.-Y., Seo, J. H., Kossenkov, A. V., Ottobri, L., Martelli, C., Lucignani, G., Bertolini, I., Locatelli, M., Bryant, K. G., Ghosh, J. C., Lisanti, S., Ku, B., Bosari, S., Languino, L. R., Speicher, D. W., and Altieri, D. C. (2016) Mitochondrial Akt regulation of hypoxic tumor reprogramming. *Cancer Cell* 30:257-272. PMID: 27505672 DOI: 10.1016/j.ccell.2016.07.004. PMCID In Progress.

Books or other non-periodical, one-time publications

Not applicable

Other publications, conference papers, and presentations

Not applicable

Websites or other Internet sites.

Not applicable

Technologies or techniques.

High-throughput drug screen of the combination of Gamitrinib plus small molecule inhibitors of MAPK pathway, ADME, pharmacokinetics and toxicology studies in two animal species.

Inventions, patent applications, and/or licenses.

Not applicable

Other Products

Not applicable

7. PARTICIPANTS & OTHER COLLABORATING ORGANIZATIONS

- **What individuals have worked on the project?**

Name:	Dario C. Altieri, M.D.
Project Role:	Principal Investigator
Researcher Identifier (e.g. ORCID ID):	
Nearest person month worked:	2
Contribution to Project:	Dr. Altieri coordinated and oversaw all of the studies of preclinical development of Gamitrinib, including ADME and safety studies, pharmacokinetics profiling and toxicology evaluation of intravenous administration of Gamitrinib to two animal species. Dr. Altieri also led the molecular studies for the characterization of the Gamitrinib pathway as a cancer therapeutic target
Funding Support:	In addition to the present award, these studies are also supported by NIH NCI CA78810 and CA14004. There is no scientific or budgetary overlap with any of these grants.

Name:	Young Chan Chae, Ph.D.
Project Role:	Postdoctoral Fellow
Researcher Identifier (e.g. ORCID ID):	
Nearest person month worked:	6
Contribution to Project:	Dr. Chae participated in the characterization of Gamitrinib formulation development and the testing of the new, Lipoid S-100®-based formulation for solubility and retained anticancer activity against tumor cell lines
Funding Support:	In addition to the present award, these studies are also supported by NIH NCI CA78810 and CA140043. There is no scientific or budgetary overlap with any of these grants.

Name:	Qin Liu, Ph.D.
Project Role:	Biostatistician
Researcher Identifier (e.g. ORCID ID):	
Nearest person month worked:	1
Contribution to Project:	As Director of the Biostatistics Unit of the Wistar Cancer Center Dr. Liu reviewed power of analysis, sample size calculations and provided statistical input for in vivo validation experiments of Gamitrinib anticancer activity.
Funding Support:	In addition to the present award, these studies are also supported by NIH NCI CA140043. There is no scientific or budgetary overlap with this grant.

Name:	Sarah Vunck, Ph.D., Scott Sanderson
Project Role:	Research Scientist, Project Coordinator –Charles River Laboratory
Researcher Identifier (e.g. ORCID ID):	
Nearest person month worked:	1
Contribution to Project:	As Research Scientist and Project Coordinator for the Gamitrinib development team, Dr. Vunck and Mr. Sanderson oversaw the non-GLP preclinical evaluation of Gamitrinib in a 7-day repeated dose study in Sprague-Dawley rats and Beagle dogs.
Funding support:	Present award.

- **Has there been a change in the active other support of the PD/PI(s) or senior/key personnel since the last reporting period?**
Nothing to report.

- **What other organizations were involved as partners?**

Albany Molecular Research International (AMRI)
Location: Albany, NY
Chemical synthesis and quality control of non-GLP and GLP grade Gamitrinib

Alliance Pharmaceuticals
Location: Malvern, PA
ADME and pharmacokinetics studies of Gamitrinib

Eurofins Panlab
Location: St. Charles, MO
Cardiac Profiler evaluation of Gamitrinib

GenScript
Location: Piscataway, NJ
hERG current analysis in transfected cells by patch clamp techniques

Organization: Charles River Laboratory
Location: Spencerville, OH
Contribution: Preclinical characterization of Gamitrinib in Sprague rats.

8. SPECIAL REPORTING REQUIREMENTS

Nothing to report

9. APPENDICES

PDFs are attached for papers identified in #6 of this report.

Targeting mitochondrial biogenesis to overcome drug resistance to MAPK inhibitors

Gao Zhang,¹ Dennie T. Frederick,² Lawrence Wu,¹ Zhi Wei,³ Clemens Krepler,¹ Satish Srinivasan,⁴ Young Chan Chae,¹ Xiaowei Xu,⁵ Harry Choi,¹ Elaida Dimwamwa,¹ Omotayo Ope,¹ Batool Shannan,¹ Devraj Basu,^{6,7} Dongmei Zhang,⁸ Manti Guha,⁴ Min Xiao,¹ Sergio Randell,¹ Katrin Sproesser,¹ Wei Xu,⁹ Jephrey Liu,⁹ Giorgos C. Karakousis,¹⁰ Lynn M. Schuchter,⁹ Tara C. Gangadhar,⁹ Ravi K. Amaravadi,⁹ Mengnan Gu,³ Caiyue Xu,¹ Abheek Ghosh,¹ Weiting Xu,³ Tian Tian,³ Jie Zhang,³ Shijie Zha,³ Qin Liu,¹ Patricia Brafford,¹ Ashani Weeraratna,¹¹ Michael A. Davies,¹² Jennifer A. Wargo,¹³ Narayan G. Avadhani,⁴ Yiling Lu,¹⁴ Gordon B. Mills,¹⁴ Dario C. Altieri,¹ Keith T. Flaherty,^{15,16} and Meenhard Herlyn¹

¹Molecular and Cellular Oncogenesis Program, The Wistar Institute, Philadelphia, Pennsylvania, USA. ²Division of Surgical Oncology, Massachusetts General Hospital Cancer Center, Boston, Massachusetts, USA. ³Department of Computer Science, New Jersey Institute of Technology, Newark, New Jersey, USA. ⁴Department of Animal Biology, School of Veterinary Medicine, University of Pennsylvania, Philadelphia, Pennsylvania, USA. ⁵Department of Pathology and Laboratory Medicine, Hospital of the University of Pennsylvania, Philadelphia, Pennsylvania, USA. ⁶Department of Otorhinolaryngology – Head and Neck Surgery, Perelman School of Medicine, University of Pennsylvania, Philadelphia, Pennsylvania, USA. ⁷Veterans Administration Medical Center, Philadelphia, Pennsylvania, USA. ⁸Department of Obstetrics and Gynecology, Perelman School of Medicine, University of Pennsylvania, Philadelphia, Pennsylvania, USA. ⁹Abramson Cancer Center, Department of Medicine, and ¹⁰Department of Surgery, Hospital of the University of Pennsylvania, Philadelphia, Pennsylvania, USA. ¹¹Tumor Microenvironment and Metastasis Program, The Wistar Institute, Philadelphia, Pennsylvania, USA. ¹²Department of Melanoma Medical Oncology, Division of Cancer Medicine, ¹³Department of Surgical Oncology, and ¹⁴Department of Systems Biology, The University of Texas MD Anderson Cancer Center, Houston, Texas, USA. ¹⁵Department of Medicine, Harvard Medical School, Boston, Massachusetts, USA. ¹⁶Division of Medical Oncology, Massachusetts General Hospital Cancer Center, Boston, Massachusetts, USA.

Targeting multiple components of the MAPK pathway can prolong the survival of patients with BRAF^{V600E} melanoma. This approach is not curative, as some BRAF-mutated melanoma cells are intrinsically resistant to MAPK inhibitors (MAPKi). At the systemic level, our knowledge of how signaling pathways underlie drug resistance needs to be further expanded. Here, we have shown that intrinsically resistant BRAF-mutated melanoma cells with a low basal level of mitochondrial biogenesis depend on this process to survive MAPKi. Intrinsically resistant cells exploited an integrated stress response, exhibited an increase in mitochondrial DNA content, and required oxidative phosphorylation to meet their bioenergetic needs. We determined that intrinsically resistant cells rely on the genes encoding TFAM, which controls mitochondrial genome replication and transcription, and TRAP1, which regulates mitochondrial protein folding. Therefore, we targeted mitochondrial biogenesis with a mitochondrion-targeted, small-molecule HSP90 inhibitor (Gamitrinib), which eradicated intrinsically resistant cells and augmented the efficacy of MAPKi by inducing mitochondrial dysfunction and inhibiting tumor bioenergetics. A subset of tumor biopsies from patients with disease progression despite MAPKi treatment showed increased mitochondrial biogenesis and tumor bioenergetics. A subset of acquired drug-resistant melanoma cell lines was sensitive to Gamitrinib. Our study establishes mitochondrial biogenesis, coupled with aberrant tumor bioenergetics, as a potential therapy escape mechanism and paves the way for a rationale-based combinatorial strategy to improve the efficacy of MAPKi.

Introduction

Cutaneous melanoma is a devastating disease, with a 10-year survival rate of less than 10% in patients diagnosed with stage IV melanoma (1). Approximately 50% of melanoma patients' tumors harbor a BRAF^{V600} mutation, resulting in constitutively activated MAPK signaling (2). Selective MAPK inhibitors (MAPKi) directly target the

MAPK pathway and significantly improve the overall and progression-free survival of patients with BRAF-mutant melanomas (3–8). Despite the clinical efficacy of targeted therapies, the initial tumor regression often precedes a rapid tumor relapse caused by the survival of residual tumor cells and the subsequent acquisition of drug resistance. The core mechanisms of acquired resistance encompass reactivation of the MAPK and PI3K/AKT signaling pathways (9).

Notably, approximately 10% to 15% of patients with BRAF-mutated melanomas do not respond to initial treatment with targeted therapies, and approximately 40% to 50% of patients experience stable or partial responses at best, suggesting that intrinsic resistance is a major hurdle to effectively eradicate all tumor cells. Genetically, accumulating evidence has suggested that *FOXD3*, *ERBB3*, *BCL2A1*, *PDK1*, *PGC1A*, *MITF*, and *NF1* underlie intrinsic resistance to targeted therapies (10–14).

Conflict of interest: K.T. Flaherty has received consulting fees from GlaxoSmithKline (GSK), Roche, and Novartis. G.B. Mills serves as a consultant for AstraZeneca, Blend Therapeutics, Critical Outcome Technologies Inc., HanAI Bio Korea, Illumina, Nuevolution, Pfizer, Provista Diagnostics, Roche, SignalChem Lifesciences, Symphogen, and Tau Therapeutics; owns stock in Catena Pharmaceuticals, PTV Healthcare Capital, Spindle Top Capital; and has received research funding from Adelson Medical Research Foundation, AstraZeneca, Critical Outcome Technologies Inc., GSK, and Illumina.

Submitted: May 4, 2015; **Accepted:** February 18, 2016.

Reference information: *J Clin Invest.* 2016;126(5):1834–1856. doi:10.1172/JCI82661.

Table 1. List of MitoBiogenesis signature

Category	Symbol	Synonyms
Coactivators of mitochondrial biogenesis	<i>PPARGC1A</i>	PPAR γ , coactivator 1 α
	<i>PPARGC1B</i>	PPAR γ , coactivator 1 β
	<i>PPRC1</i>	PPAR γ , coactivator-related 1
Nuclear respiratory factors	<i>NRF1</i>	Nuclear respiratory factor 1
	<i>NFE2L2</i>	Nuclear factor erythroid-derived 2-like 2
Other regulators of mitochondrial biogenesis	<i>ESRRA</i>	Estrogen-related receptor α
Mitochondrial transcription factors	<i>TFAM</i>	Mitochondrial transcription factor A
	<i>TFB1M</i>	Mitochondrial transcription factor B1
	<i>TFB2M</i>	Mitochondrial transcription factor B2
mtDNA replication factors	<i>POLGA</i>	mtDNA polymerase catalytic subunit
	<i>POLGB</i>	mtDNA polymerase accessory subunit
	<i>Twinkle</i>	T7-like mtDNA helicase
Mitochondrial membrane Integrity	<i>PHB1</i>	Prohibitin
	<i>PHB2</i>	Prohibitin 2
Mitochondrial fission mediators	<i>DRP1</i>	Dynamin-related protein 1
	<i>FIS1</i>	Mitochondrial fission 1 protein
Mitochondrial fusion mediators	<i>MFN1</i>	Mitofusin 1
	<i>MFN2</i>	Mitofusin 2

Abnormal metabolic reprogramming is a unique mechanism by which cancer cells not only adapt to the microenvironment but also generate energy (15). The Warburg effect illustrates that aerobic glycolysis is the predominant metabolic pathway for cancer cells to produce energy. However, slow-cycling melanoma cells that are characterized by high expression levels of the histone demethylase *JARID1B* predominantly utilize oxidative phosphorylation (OxPhos) to generate ATP and are intrinsically resistant to multiple signaling inhibitors (16, 17). A subset of human melanoma cell lines with high expression levels of *PGC1A* are less glycolytic and rely more heavily on mitochondrial OxPhos to generate ATP (18). When BRAF-mutated melanoma cells were treated with vemurafenib, the *MITF/PGC1A* signaling axis was upregulated, resulting in metabolic reprogramming toward OxPhos and conferring intrinsic resistance to BRAF inhibitors (13). Similarly, the treatment of leukemia cells with tyrosine kinase inhibitors also altered the metabolic state of surviving cells that remained sensitive to oligomycin-A, which targeted mitochondrial respiration (19).

Understanding which signaling pathway(s) are premier therapeutic targets for overcoming drug resistance remains largely elusive. Mitochondrial biogenesis is a biological process involving the formation of new mitochondria due to the regulation of mitochondrial fusion and fission. Numerous nuclear genome- and mitochondrial genome-encoding factors are controlling mitochondrial biogenesis in response to stress stimuli (20). Here, we

focus on the mitochondrial biogenesis signature and investigate its role in mediating resistance to MAPKi. We address the molecular basis of this novel resistance mechanism, which is tightly coupled to aberrant tumor bioenergetics. Furthermore, we show that the small-molecule inhibitor Gamitrinib, which targets mitochondrial HSP90-directed (or TRAP1-directed) protein folding, is effective in circumventing mitochondrial biogenesis. By overcoming both intrinsic and acquired resistance, we can progress toward the long-term goal of eliminating all malignant cells as a precondition for achieving cures.

Results

BRAF-mutated melanoma cell lines with lower expression of mitochondrial biogenesis and mitochondrial mass at the basal level were more resistant to MAPKi. We first consulted the current literature and curated a list of 18 genes that are essential for controlling mitochondrial biogenesis to compose the gene signature “Mito-Biogenesis.” Specifically, these genes are: (a) nuclear respiratory factors (*NRF1* and *NFE2L2* or *NRF2*) and PGC-1 family coactivators (*PPARGC1A* or *PGC1A*, *PPARGC1B* or *PGC1B*, *PPRC1*, and *ESRRA*), which coordinately control mitochondrial transcription specificity factors (*TFAM*, *TFB1M*, and *TFB2M*) (21); (b) *POLGA*, *POLGB*, and *Twinkle*, which collectively regulate mitochondrial transcription, mitochondrial DNA (mtDNA) replication, and packaging in the mitochondrial genome (22); (c) prohibitin 1 (*PHB1*) and prohibitin 2 (*PHB2*), which reside in the inner mitochondrial membrane to safeguard mitochondrial quality control (23); and (d) *MFN1*, *MFN2*, *DRP1*, and *FIS1*, which regulate mitochondrial fusion and fission (ref. 24 and Table 1).

We then sought to determine whether MitoBiogenesis is one of the defining features that distinguish melanoma from other cancer types. Toward this goal, we analyzed genome-wide gene expression data for 947 human cancer cell lines collected for the Cancer Cell Line Encyclopedia (CCLE) project (25). In order to identify gene sets that are only enriched in melanoma, we compared melanoma cell lines with nonmelanoma cancer cell lines and performed gene set enrichment analysis (GSEA). Not surprisingly, the analysis showed that “BRAF Targets,” “MEK Targets,” “Melanogenesis,” and “Lysosome” were among the top 10 ranked gene sets that were enriched in melanoma (Supplemental Figure 1; supplemental material available online with this article; doi:10.1172/JCI82661DS1). “MitoBiogenesis,” however, was not identified among those top-10-ranked gene sets. This led us to test our alternative hypothesis that MitoBiogenesis is enriched only in a subset of melanoma cell lines. We were able to separate 61 CCLE human melanoma cell lines into 2 subgroups: higher and lower expression of MitoBiogenesis (Figure 1A). Next, we obtained 16 additional mitochondrial gene sets from the Molecular Signatures Database (MSigDB) and investigated their correlations with MitoBiogenesis. For each cell line, we performed single-sample GSEA (ssGSEA) in order to calculate the enrichment score for each gene set. “KEGG Glycolysis and Gluconeogenesis” and “KEGG Oxidative Phosphorylation” were also included as controls. The analysis revealed that MitoBiogenesis was clustered with 16 MSigDB mitochondrial gene sets (Figure 1B).

Furthermore, we performed the Illumina genome-wide gene expression experiment to profile 10 of our own BRAF-mutated melanoma cell lines. ssGSEA revealed that 4 of 10 cell lines,

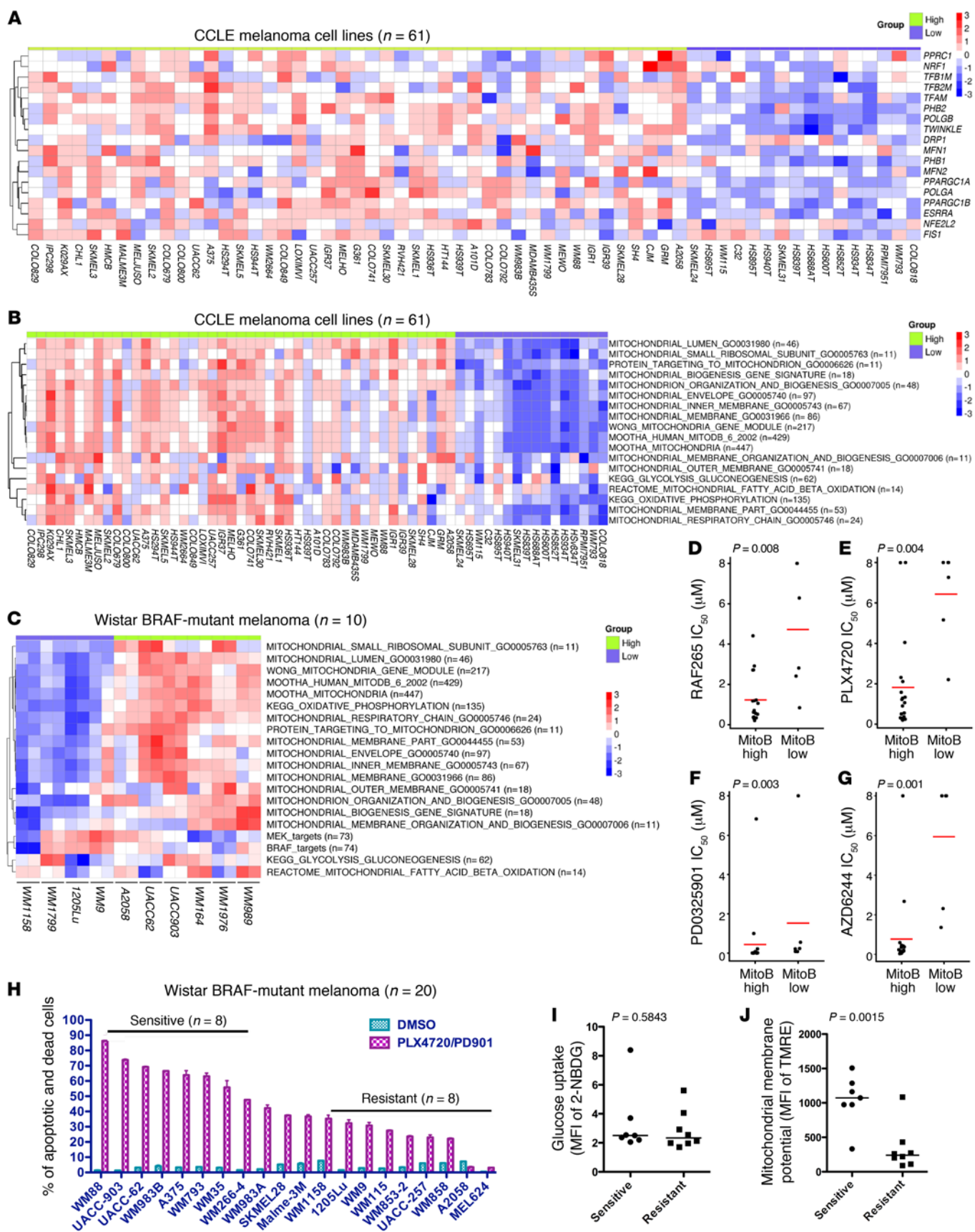


Figure 1. BRAF-mutated melanoma cells with lower mitochondrial biogenesis and mass at the basal level are resistant to MAPKi. (A)

Heatmap of microarray data for MitoBiogenesis in 61 CCLE melanoma cell lines. **(B and C)** Heatmaps of enrichment scores for 16 mitochondrial gene sets, 2 metabolic gene sets, and 2 MAPK pathway gene sets in 61 CCLE **(B)** and 10 Wistar Institute **(C)** melanoma cell lines. **(D–G)** Drug IC_{50} of CCLE BRAF-mutated melanoma cell lines RAF265 **(D)**, PLX4720 **(E)**, PD0325901 **(F)**, and AZD6244 **(G)**. A 2-sample *t* test was used to determine the *P* values in **D–G**. **(H)** Percentage of PSVue 643⁺ cells in each BRAF-mutated melanoma cell line treated with DMSO or MAPKi for 72 hours. **(I and J)** Mean fluorescence intensity (MFI) of 2-NBDG **(I)** and MitoTracker Red **(J)** in melanoma cell lines. Data were normalized to the MFI derived from the unstained sample of each cell line. **(H–J)** *n* = 3; data represent 2 independent experiments. A 2-tailed, unpaired *t* test was used to determine the *P* values in **H** and **I**. MitoB, MitoTracker B. Horizontal bars in panels **D–J** denote the mean of each group.

including WM1158, WM1799, 1205Lu, and WM9, had lower expression of MitoBiogenesis, in which all mitochondrial gene sets were expressed at a lower level (Figure 1C).

Drug-sensitivity data on 4 MAPKi were available for CCLE BRAF-mutated melanoma cell lines, including 2 BRAF inhibitors, RAF265 and PLX4720, as well as 2 MEK inhibitors, PD0325901 and AZD6244. Therefore, we tested whether there is any correlation between MitoBiogenesis expression and drug sensitivities. Interestingly, our analysis showed that BRAF-mutated melanoma cell lines with lower expression of MitoBiogenesis had a significantly higher drug IC_{50} for all 4 inhibitors, suggesting that these cell lines were more resistant to MAPKi (Figure 1, D–G).

Next, we treated 20 of our own BRAF-mutated melanoma cell lines with PLX4720 plus PD0325901 for 72 hours. We classified these cell lines into “sensitive” (*n* = 8) and “resistant” (*n* = 9) subgroups on the basis of the degree of apoptosis and cell death induced by PLX4720 plus PD0325901 treatment (Figure 1H). This result demonstrated the heterogeneous responses of the melanoma cell lines to MAPKi. For 9 cell lines in the “resistant” group, 6 were profiled by genome-wide gene expression array experiments, and the analysis showed that 5 of 6 cell lines, including WM1158, 1205Lu, WM9, WM115, and A2058, had lower expression levels of MitoBiogenesis (Figure 1, B and C). For 8 cell lines in the “sensitive” group, 7 were profiled by genome-wide gene expression array experiments, and the analysis showed that 6 of 7 cell lines, including WM88, UACC-903, UACC-62, WM983B, A375, and WM266-4, had higher expression levels of MitoBiogenesis (Figure 1, B and C).

Subsequently, we tried to correlate drug sensitivities with the glycolytic capacities and the levels of mitochondrial mass of these cell lines, respectively. The glucose uptake assay did not reveal a statistically significant difference between 2 subgroups, suggesting that the glycolytic capacity was not correlated with drug sensitivity (Figure 1I). Intriguingly, “resistant” cell lines had a significantly lower mitochondrial membrane potential than that of “sensitive” cell lines and hence a lower level of mitochondrial mass (Figure 1J).

Taken together, our data demonstrated that a subgroup of BRAF-mutated melanoma cell lines with lower expression of MitoBiogenesis and mitochondrial mass at the basal level was more resistant to MAPKi.

Patients with higher expression of MitoBiogenesis and tumor metabolism had worse overall survival. To interrogate the expression of MitoBiogenesis in tumor biopsies derived from patients with malignant melanoma, we performed ssGSEA in 2 independent cohorts of patients, including 470 patients listed in The Cancer Genome Atlas (TCGA) with skin cutaneous melanoma (SKCM) and 104 patients with melanoma (Gene Expression Omnibus [GEO] database accession number GSE46517). The analysis of MitoBiogenesis expression showed that there were 2 subgroups of patients’ tumors in each data set (Figure 2, A and B, and refs. 26, 27). This extended analysis from cell lines to patients’ tumors confirmed our hypothesis that MitoBiogenesis is highly expressed in a subset of, but not in all, melanoma cell lines or patients’ tumors.

We next explored the clinical association of MitoBiogenesis expression with patients’ overall survival rates using TCGA SKCM data set. The Kaplan-Meier survival analysis showed that patients with higher expression of MitoBiogenesis in their tumors had a worse overall survival than did patients with lower expression of MitoBiogenesis (Figure 2C).

Because *PPARGC1A* (*PGC1A*) is a master regulator of MitoBiogenesis, we also separated TCGA melanoma patients into 2 subgroups on the basis of their *PGC1A* expression levels. Consistent with the previous finding, patients with higher expression levels of *PGC1A* had a worse overall survival outcome (Figure 2D and ref. 18).

Similarly, we subdivided TCGA melanoma patients into 4 subgroups on the basis of expression of glycolysis and OxPhos gene sets in their tumors. Intriguingly, we found that a subgroup of patients (*n* = 25) whose tumor biopsies highly expressed both glycolysis and OxPhos had the worst prognosis (Figure 2E).

MAPKi regulated expression of MitoBiogenesis in BRAF-mutated melanomas. The finding that lower expression of MitoBiogenesis and mitochondrial mass was associated with drug resistance prompted us to investigate whether and how short-term treatment with MAPKi alters MitoBiogenesis. We conducted an Illumina genome-wide gene expression array experiment to profile 4 BRAF-mutated melanoma cell lines: UACC-62, WM989, and WM164, with higher expression of MitoBiogenesis, and WM9, with lower expression of MitoBiogenesis — all of which were treated with PLX4720. We also obtained publicly available genome-wide gene expression data for 4 more BRAF-mutated melanoma cell lines that had higher expression of MitoBiogenesis: SK-MEL-28, A375, Malme-3M, and COLO829, which were treated with vemurafenib or PD0325901.

The analysis of genome-wide gene expression data showed that MitoBiogenesis expression was inhibited by MAPKi in cell lines with higher expression of MitoBiogenesis, including UACC-62, WM989, WM164, SK-MEL-28, and A375, which were treated with PLX4720 or vemurafenib (Figure 3, A–C and Figure 4, A–C), and Malme-3M and COLO829, which were treated with PD0325901 (Supplemental Figure 2, A and B, and ref. 28). The analysis of time-course genome-wide gene expression data also revealed that PLX4720 increased MitoBiogenesis expression, as exhibited by WM9 cells that had lower expression of MitoBiogenesis (Figure 4C).

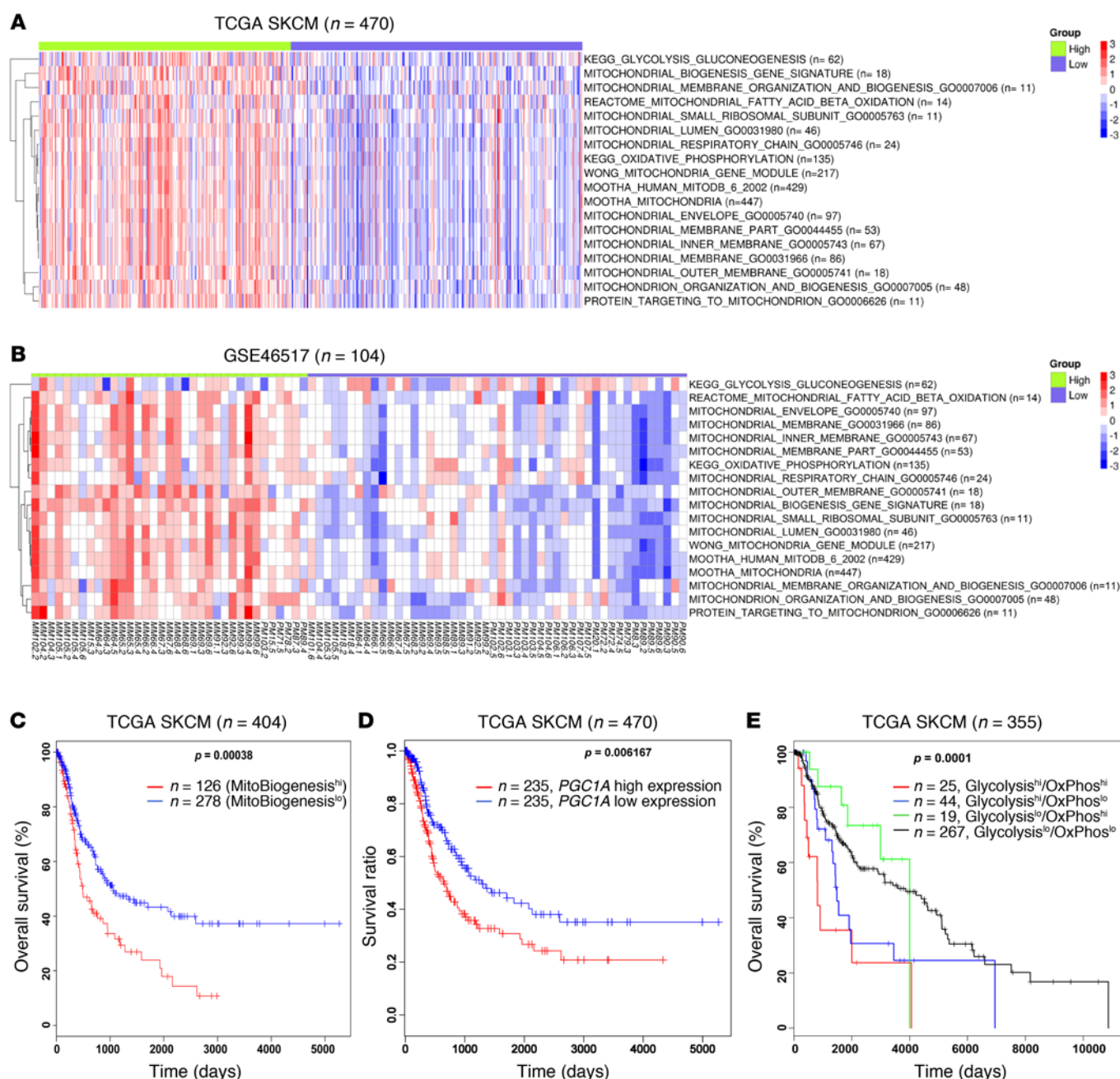


Figure 2. TCGA melanoma patients have a worse overall survival outcome if their tumors express high levels of MitoBiogenesis. (A and B) Heatmaps of enrichment scores for 16 mitochondrial gene sets and 2 metabolic genes in 470 TCGA melanoma patients (A) and 104 melanoma patients (GSE46517) (B). (C-E) Kaplan-Meier survival curves for TCGA melanoma patients who were divided into 2 subgroups of high and low expression of MitoTracker B (C), 2 subgroups of high and low expression of *PGC1A* (D), and 4 subgroups on the basis of their expression of 62 glycolytic and 135 OxPhos genes (E). *P* values in C-E were determined by log-rank test.

A quantitative real-time PCR (qRT-PCR) experiment confirmed that MAPKi blocked expression of MitoBiogenesis in A375 cells with higher expression of MitoBiogenesis, but upregulated MitoBiogenesis in WM793 and WM9 cells with lower expression of MitoBiogenesis (Table 2).

In summary, our data suggested that MAPKi suppressed MitoBiogenesis in melanoma cell lines with higher expression of MitoBiogenesis, resulting in a lower drug IC_{50} , and upregulated

MitoBiogenesis in melanoma cell lines with lower expression of MitoBiogenesis, leading to a higher drug IC_{50} .

To address the clinical implication of this phenomenon, we determined the expression levels of MitoBiogenesis in 18 BRAF-mutated melanoma patients' paired pre- and early-on treatment tumor biopsies that were procured between days 14 and 16 following the first dose of MAPKi (Table 3). Eight patients' early-on treatment tumor biopsies (Massachusetts

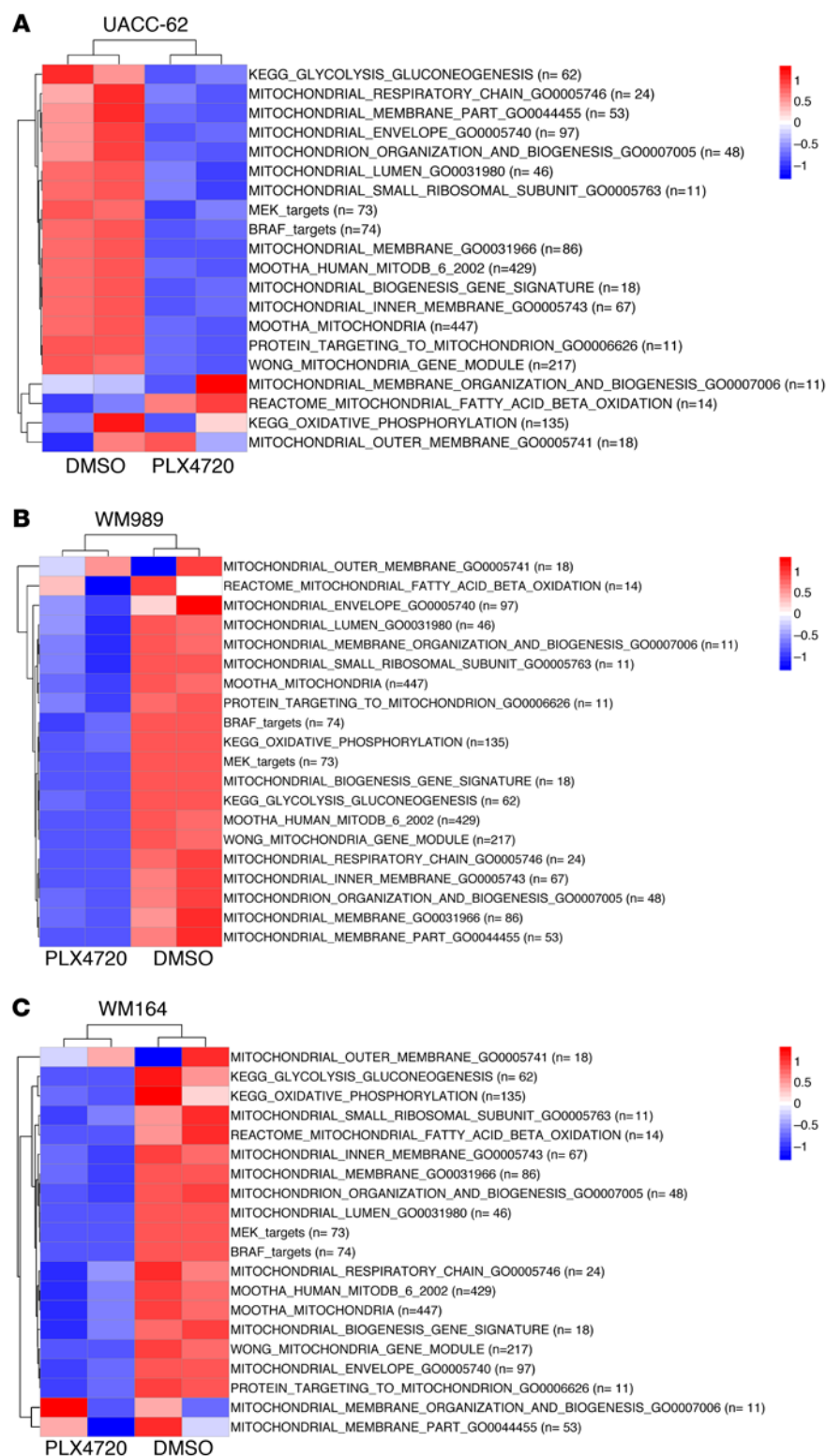


Figure 3. MAPKi regulate the expression of MitoBiogenesis in BRAF-mutated melanoma cell lines at the RNA level. Heatmaps of enrichment scores for 16 mitochondrial gene sets, 2 metabolic gene sets, and 2 MAPK pathway gene sets in UACC-62 (A), WM989 (B), and WM164 cells (C) treated with 10 μ M DMSO or PLX4720 for 96 hours.

tein import and macromolecular assembly; VDAC1, which is implicated as a gatekeeper for the transport of mitochondrial metabolites; TUFM, which is implicated in mitochondrial protein translation; and SOD2, which regulates the detoxification of ROS to protect against oxidative stress (Supplemental Table 1 and refs. 29–32). For SK-MEL-28 and A375 melanoma cells that were sensitive to MAPKi and had higher expression of MitoBiogenesis at the basal level, MAPKi downregulated the expression of ESRRA, NRF2, TUFM, TFAM, and PGC1 α/β (Figure 5, A–C). For WM9 cells that were resistant to MAPKi and had lower expression of MitoBiogenesis, MAPKi activated MitoBiogenesis, as evidenced by upregulation of PGC1 α , TFAM, NRF2, PHB1, PHB2, SOD2, and ESRRA (Figure 5D). We further showed that expression of ESRRA, TFAM, PHB1, PHB2, VDAC1, TUFM, HSP60, and SOD2 was upregulated in WM9 cells by PLX4720 or PLX4720 plus PD0325901 in a time-dependent manner (Figure 5, E and F).

MAPKi led to an increase in mtDNA content and mitochondrial mass in BRAF-mutated melanoma cells. Next, we focused on 3 key biological aspects of MitoBiogenesis, including mtDNA content, mitochondrial mass, and ROS.

For 3 intrinsically resistant melanoma cell lines (WM9, 1205Lu, and MEL624) treated with MAPKi, we found that the mtDNA content was significantly increased in surviving cells (Figure 6, A and B, and Supplemental Figure 3A). We also demonstrated that mitochondrial mass was significantly enhanced (Figure 6C and Supplemental Figure 3B). MAPKi significantly suppressed mitochondrial mass in 4 sensitive cell lines (A375, WM266-4, UACC-62, and 451Lu) (Supplemental Figure 3, C–F).

In 3 of 10 early-on treatment tumor biopsies derived from patients (MGH patients 7, 24, and 35), mtDNA content was significantly increased compared with that of the respective pretreatment tumor biopsies (Figure 6D). Furthermore, transcriptional factor A, mitochondrial (TFAM), a transcriptional regulator of mtDNA content, was significantly upregulated in these early-on treatment tumor biopsies (Table 4, Figure 6E, and ref. 33).

General Hospital [MGH] patients 6, 7, 10, 12, 24, 25, 34, and 42) showed a more than 55% increase in expression of 18 MitoBiogenesis genes (Table 4).

We also corroborated our genome-wide gene expression array and qRT-PCR data on SK-MEL-28, A375, and WM9 cells with immunoblotting data. We included 4 more mitochondrial proteins, including HSP60, which is implicated in mitochondrial pro-

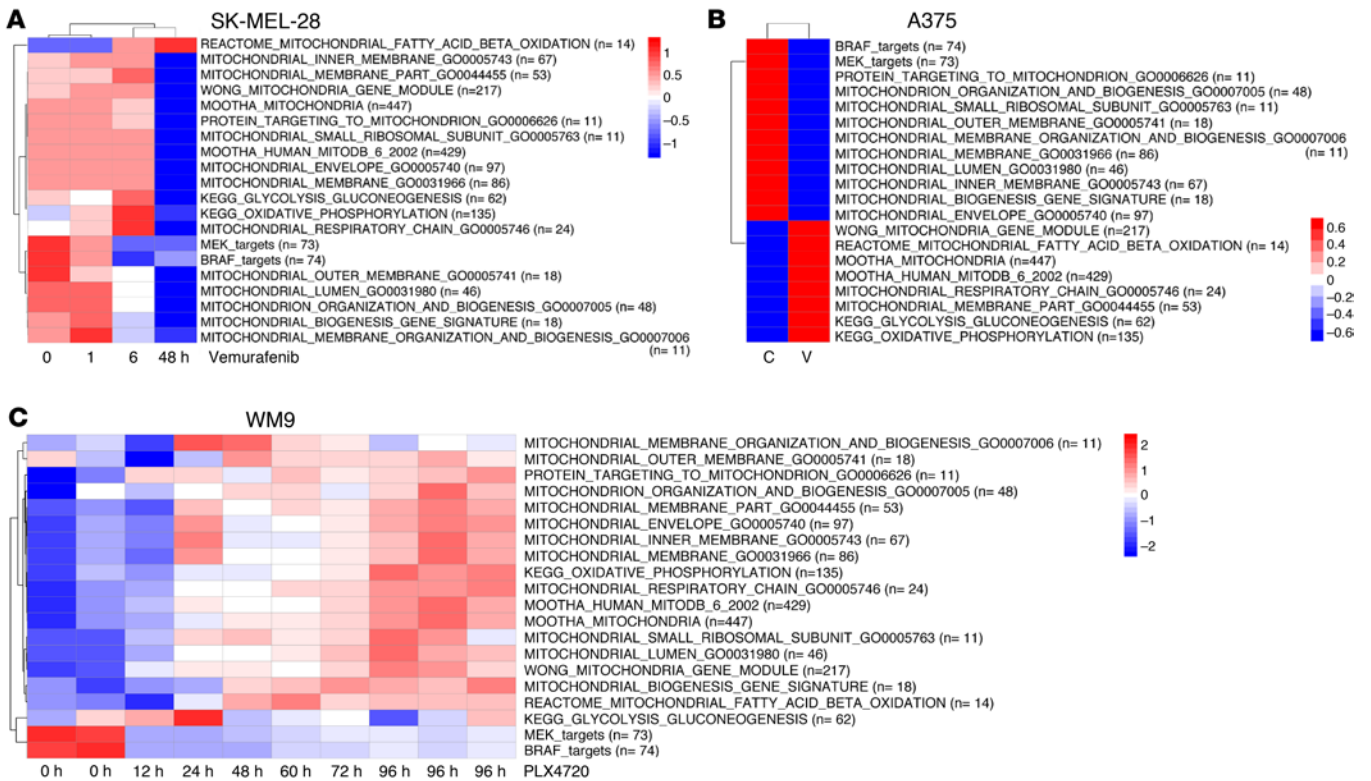


Figure 4. MAPKi regulate the expression of MitoBiogenesis in BRAF-mutated melanoma cell lines at the RNA level. Heatmaps of enrichment scores for 16 mitochondrial gene sets, 2 metabolic gene sets, and 2 MAPK pathway gene sets in SK-MEL-28 cells (A) treated with vemurafenib for 48 hours, in A375 cells (B) treated with the control and vemurafenib for 48 hours, and in WM9 cells (C) treated with 10 μ M PLX4720 for 96 hours. C, control; V, vemurafenib.

Finally, we showed that MAPKi resulted in a significant increase in ROS production in both WM9 and 1205Lu cell lines (Figure 6, F and G). The increase in ROS production was accompanied by an upregulation of the antioxidant gene superoxide dismutase 2 (SOD2) at both mRNA and protein levels (Figure 5, D–F, Figure 6H, and Supplemental Figure 3G). Using paired pre- and early-on treatment tumor biopsies, we demonstrated that the expression of SOD2 was increased in early-on treatment tumor biopsies (Figure 6I).

Taken together, our data showed that MAPKi substantially enhanced the expression of MitoBiogenesis in surviving cells in a

subset of BRAF-mutated melanoma cell lines or patients’ tumor biopsies that escaped short-term inhibition of the MAPK pathway.

MAPKi significantly induced OxPhos, lysosomes, and ATP-binding cassette transporters in melanoma cells with high expression of MitoBiogenesis that were slowly cycling. In each BRAF-mutated melanoma cell line that was tested, short-term treatment with MAPKi always led to the enrichment of surviving cells (Figure 1H). By testing WM9 and 1205Lu cell lines, we confirmed that surviving cells were arrested in the G₀/1 phase of the cell cycle (Supplemental Figure 4, A and B).

Table 2. Relative expression of 18 MitoBiogenesis genes in BRAF-mutant melanoma cell lines treated with MAPKi for 72 hours

Sample	PPARGC1A	PPARGC1B	PPRC1	ESRRA	NRF1	NFE2L2	TFAM	TFB1M	TFB2M	POLGA	POLGB	Twinkle	PHB1	PHB2	DRP1	FIS1	MFN1	MFN2
A375 PLX4720	18.5	0.9	0.4	0.8	0.4	0.2	0.3	0.1	0.4	0.4	0.3	0.9	0.5	0.7	0.2	0.6	0.5	0.4
WM793 PLX4720	38.5	3.5	2	3.3	3.4	1.7	1	0.6	1.6	3.1	1.4	0.9	1.5	1.3	1.6	3.1	1.8	1.7
WM9 PLX4720	68.5	4.2	6.5	11.7	3.5	0.9	3.3	0.6	1.9	3.9	2.4	3.3	3.1	2.3	3.6	5.8	6.9	4.8
WM9 PLX4720/ PD901	102.6	6.2	4.6	13	3.3	2.1	4.1	0.6	1.6	3.9	2.3	2.8	2.7	2.6	2.8	3.4	4.6	3.2

Red: ≥ 2 -fold increase; blue: ≤ 2 -fold decrease. Data were normalized to cells treated with DMSO.

Table 3. Clinical information for 24 BRAF-mutated melanoma patients treated at Massachusetts General Hospital

Patient	Mutation	Treatment	Dose (daily)	Response	Time to progression (mo)
2	BRAF	Vemurafenib	1,920 mg	PR (-60.5%)	8.5
4	BRAF	Vemurafenib	1,920 mg	PR (-56%)	3.5
5	BRAF	Vemurafenib	1,920 mg	SD (-27%)	6.5
6	BRAF	Dabrafenib + trametinib	Dabrafenib: 300 mg, trametinib: 2 mg	PR (-59.9%)	21
7	BRAF	Dabrafenib + trametinib	Dabrafenib: 300 mg, trametinib: 2 mg	CR (100%)	17, ongoing 47 mo
8	BRAF	Dabrafenib + trametinib	Dabrafenib: 300 mg, trametinib: 1.5 mg	PR (-30%)	3
9	BRAF	Dabrafenib + trametinib	Dabrafenib: 300 mg, trametinib: 2 mg	PR (-45%)	7
10	BRAF	Dabrafenib + trametinib	Dabrafenib: 300 mg, trametinib: 2 mg	SD (-13%)	3
11	BRAF	Dabrafenib + trametinib	Dabrafenib: 300 mg, trametinib: 2 mg	PR (-80%)	10
12	BRAF	Dabrafenib + trametinib	Dabrafenib: 300 mg, trametinib: 2 mg	PR (-88.9%)	12; stopped at 20 mo
13	BRAF	Dabrafenib + trametinib	Dabrafenib: 300 mg, trametinib: 2 mg	PR (-57.9%)	9; stroke
15	BRAF	Vemurafenib	1,920 mg	SD (-16.5%)	6
16	BRAF	Dabrafenib + trametinib	Dabrafenib: 300 mg, trametinib: 1 mg	SD (-19.5%)	11
19	BRAF	Dabrafenib + trametinib	Dabrafenib: 300 mg, trametinib: 2 mg	PR (-48.7%)	Ongoing; 36 mo
20	BRAF	Vemurafenib	1,920 mg	PR (-51.2%)	5
22	BRAF	Dabrafenib + trametinib	Dabrafenib: 300 mg, trametinib: 2 mg	PR (-42%)	3
24	BRAF	Vemurafenib	1,920 mg	PR (-53%)	2
25	BRAF	Dabrafenib + trametinib	Dabrafenib: 150 mg, trametinib: 2 mg	PR (-64%)	3
34	BRAF	LGX818 + MEK162	LGX818: 600 mg, MEK162: 45 mg	PR (-48.6%)	Stopped drug after 14 months; PD at 15 mo
35	BRAF	LGX818 + MEK162	LGX818: 600 mg, MEK162: 45 mg	SD (-22.8%)	Stopped after 7 mo; PD at 10 mo
38	BRAF	Vemurafenib	1,920 mg	SD (-24.9%)	4.3
40	BRAF	Vemurafenib	1,920 mg	SD	Stopped drug after 6 mo; PD at 9 mo
42	BRAF	LGX818 + MEK162	LGX818: 400 mg, MEK162: 60 mg	PR (-76.1%)	PD at 13 mo
43	BRAF	Vemurafenib	1,920 mg	CR (-81.5%)	13.4

PR, partial response; CR, complete response; SD, stable disease; PD, progressive disease.

In order to investigate the kinetics of cell division shown by surviving cells, prior to MAPKi treatment, we labeled an intrinsically resistant cell line, WM9, and 2 sensitive cell lines, A375 and WM266-4, with a cell proliferation fluorescent dye, CellTrace Violet. We tracked the fluorescence intensity of CellTrace Violet at multiple time points during the treatment and observed that, regardless of their expression of MitoBiogenesis and drug sensitivities, surviving cells in all 3 cell lines were dividing at a much slower rate than were control cells (Figure 7, A–C). Treatment with PLX4720 plus PD0325901 resulted in a much more pronounced slow-cycling phenotype compared with that observed with PLX4720 treatment, as demonstrated by surviving cells in WM9 and A375, but not WM266-4, cells (Figure 7, A–C).

Taken together, our data revealed that, although surviving cells were initially arrested in the $G_{0/1}$ phase, they were capable of slow proliferation in the presence of MAPKi.

By focusing on WM9 surviving cells, we decided to elucidate the molecular basis underlying the increase in MitoBiogenesis. We analyzed time-course Illumina genome-wide gene expression microarray data. GSEA revealed a striking temporal expression profile change. Forty-eight hours was a critical transition time point, at and beyond which 6 upregulated pathways, including “Oxidative Phosphorylation (OxPhos),” “Lysosome,” “Parkinson’s Disease,” “Alzheimer’s Disease,” “Huntington’s Disease,” and “ABC Transporters,” were identified as top pathways that were enriched in surviving cells (Figure 7D and Supplemental Table 1).

“MEK Targets,” “BRAF Targets,” and “Cell Cycle” emerged as the top-3-ranked downregulated pathways, confirming that PLX4720 inhibited the MAPK pathway and cell-cycle progression (Figure 7D and Supplemental Table 2).

To validate the results based on genome-wide gene expression data, we first performed a qRT-PCR experiment and showed that expression of *DUSP6* and *FOXM1* was suppressed by PLX4720 in surviving cells (Supplemental Figure 4, C and D). We also observed that in surviving cells, a continuous treatment with PLX4720 for 120 hours resulted in the upregulation of 5 representative mitochondrial respiratory chain subunits including *NDUFA8*, *SDHB*, *UQCRCB*, *MT-CO1*, and *ATP5G1*, which was accompanied by increased expression of *PDP2* and *TXNIP*, both of which were negative regulators of glycolysis (Figure 8A). Additionally, we demonstrated that the expression of 30 mitochondria respiratory chain complex subunits was substantially increased in surviving cells that escaped the 72-hour treatment with MAPKi (Figure 8B and Supplemental Figure 4E). Moreover, we showed that the expression of 3 representative respiratory chain subunits, *NDUFA8*, *MT-CO1*, and *COX7B*, was significantly upregulated in patients’ early-on treatment tumor biopsies compared with that seen in paired pretreatment tumor biopsies (Figure 8C). MAPKi upregulated 6 mitochondrial respiratory chain complex subunits, *NDUFB8*, *SDHA*, *SDHB*, *UQCRC2*, *COX II*, and *ATP5A*, at the protein level in surviving cells, which was accompanied by suppression of phospho-ERK (p-ERK), p-Rb, and p-S6 as well as upregulation of p27 and the DNA damage marker γ -H2AX (Figure

Table 4. Relative expression of 18 MitoBiogenesis genes in BRAF-mutant human melanoma patients' early-on treatment tumor biopsies

MGH patient ID	PPARGC1A	PPARGC1B	PPRC1	ESRRA	NRF1	NFE2L2	TFAM	TFB1M	TFB2M	POLGA	POLGB	Twinkle	PHB1	PHB2	DRP1	FIS1	MFN1	MFN2
2B	2.1	2.7	4.5	3.2	1.7	3.6	1.3	1.8	1.4	3.4	0.2	1.3	1.6	2.4	1.3	1.3	1.4	1.5
5B	1.0	1.1	1.1	1.5	0.6	1.5	1.6	0.7	2.5	1.6	0.4	0.3	1.1	1.3	0.5	0.6	0.8	0.9
6B	10.4	11.4	3.1	7.0	13.1	13.9	4.9	5.0	3.0	4.9	11.4	5.0	2.6	3.0	5.1	8.2	7.0	6.1
7B	4.9	24.7	3.9	16.5	9.1	6.9	5.0	8.3	2.8	4.1	3.2	4.1	2.9	5.9	5.4	3.7	6.9	5.0
9B	17.7	0.3	0.4	0.1	0.5	0.6	0.8	0.6	0.8	0.6	0.6	8.7	1.2	0.8	0.8	0.7	1.1	0.8
10B	12.1	28.1	5.5	3.6	11.2	1.6	1.6	2.5	2.4	6.1	10.8	1.1	1.0	1.7	12.0	7.5	8.9	2.0
11B	0.1	1.2	1.2	2.4	0.7	0.4	1.0	0.5	0.6	0.6	1.8	1.0	0.5	0.6	0.9	0.7	0.9	0.8
12B	29.0	14.5	4.2	24.6	3.4	0.7	4.6	1.2	0.7	5.5	1.0	1.6	0.6	0.9	3.6	1.6	3.2	2.9
13B	0.2	0.7	1.8	1.3	1.4	18.2	5.1	0.6	0.6	5.3	3.6	8.6	0.4	1.3	2.0	0.9	1.0	2.0
16B	0.1	1.7	2.8	5.2	1.2	0.7	0.5	0.6	0.2	0.9	0.3	0.4	0.2	1.2	1.1	0.8	1.0	0.8
24B	3.2	34.5	3.7	18.9	10.4	6.1	2.1	2.4	3.2	9.8	8.8	0.7	1.4	2.2	4.9	5.3	7.5	5.6
25B	4.1	22.8	7.3	8.9	15.2	1.4	3.3	7.8	5.7	3.2	3.9	1.5	5.8	4.9	5.7	7.3	8.0	2.8
34B	8.1	7.2	5.4	1.9	12.6	3.9	4.5	3.5	2.5	8.9	2.6	3.2	2.0	4.0	2.2	2.3	3.4	3.1
35B	0.3	3.6	3.6	7.5	2.1	2.5	2.5	2.2	2.1	0.6	1.9	1.8	1.3	1.8	1.7	2.4	1.6	2.7
38B	1.6	21.6	3.9	25.2	5.2	1.3	2.5	5.0	0.4	4.1	9.4	1.7	1.8	2.7	4.1	4.4	6.1	4.7
40B	0.3	1.6	1.8	0.5	0.2	0.4	0.5	1.4	0.2	0.7	0.4	0.8	0.5	0.9	1.0	0.7	0.7	0.6
42B	1.6	1.6	2.8	2.0	3.7	3.4	4.6	2.7	2.3	4.1	4.9	2.4	2.1	2.4	2.0	1.5	3.2	3.5
43B	0.4	1.1	1.4	1.1	0.9	1.2	1.6	1.7	0.9	2.2	1.2	1.2	0.9	1.4	0.8	0.9	1.1	0.9

Red: ≥ 2 -fold increase; blue: ≤ 2 -fold decrease. Data were normalized to each patient's pretreatment tumor biopsy.

8D). The increase in OxPhos in WM9 surviving cells was demonstrated by an increase in oxygen consumption, particularly maximal respiration (Figure 8, E and F).

In the late stage of autophagy, autophagosomes fuse with lysosomes to degrade captured cellular substrates or damaged organelles. Expression of LC3B-II was induced in WM9 surviving cells by MAPKi (Figure 5H), which was in line with the increase in autophagic flux as assessed by the ratio of mCherry over eGFP in WM9 cells expressing a fluorescent autophagy reporter construct, mCherry-EGFP-LC3B (Supplemental Figure 4F). Furthermore, expression of the ER stress genes *CHOP*, *GRP78*, *GRP94*, *ATF4*, *GADD34*, and *ERDJ4* was markedly induced in surviving cells (Supplemental Figure 4G). Together, our data showed that MAPKi induced a profound stress response program and upregulated the expression of MitoBiogenesis in surviving cells.

Finally, we confirmed that expression of the representative ATP-binding cassette (ABC) transporters *ABCC1*, *ABCG2*, *ABCC2*, and *ABCB5* was substantially upregulated by MAPKi in surviving cells (Supplemental Figure 4, H and I).

Altogether, our experiments identified and confirmed that OxPhos, ER stress, autophagy/lysosomes, and ABC transporters were strongly induced in surviving cells in which MitoBiogenesis was highly expressed. Our data also underscored the potential roles of these processes as a survival mechanism by which BRAF-mutated melanoma cells escape MAPKi.

Depletion of TFAM or TRAP1, but not PGC1A, inhibited MitoBiogenesis. Our next goal was to pinpoint which genes were essential for surviving cells. We performed 2 selective siRNA screens in WM9 cells by depleting 6 genes related to autophagy and ER stress response and 18 genes related to MitoBiogenesis and tumor bioenergetics and subsequently treating cells with PLX4720 plus PD0325901 (Supplemental Figure 5, A and B).

In the first siRNA screen, we tested the combination of MAPKi and siRNAs that inhibited the autophagy and ER stress response pathways. The autophagy inhibitor spautin-1 was included as a control. We observed that, although the combination of siRNAs targeting the autophagy-ER stress response and MAPKi indeed effectively led to a decrease in the autophagic flux that was enhanced by MAPKi alone (Supplemental Figure 5, C and E), MAPKi, combined with either siRNAs (with the exception of siRNA targeting VPS34) or the autophagy inhibitor spautin-1, was not able to trigger a significant induction of apoptosis and cell death (Supplemental Figure 5, D and F). These data suggested that, upon the dual inhibition of the autophagy-ER stress response and the MAPK pathway, surviving cells may activate other compensatory pathways. Another possibility was that the autophagy-ER stress response pathways did not necessarily affect the efficacy of MAPKi.

In the second siRNA screen, we focused on the combination of MAPKi and siRNAs targeting 8 MitoBiogenesis genes, *TRAP1*, 5 OxPhos genes, and 4 glycolytic genes. The mitochondrial HSP90 inhibitor Gamitrinib was included as a control. *TRAP1* is critical in directing mitochondrial protein folding to control central metabolic networks (34–36). Targeting *TRAP1*-directed protein folding in mitochondria with Gamitrinib inhibits both glycolysis and OxPhos in a diverse panel of cancer cell lines including melanomas (35). Gamitrinib is a metabolic poison that is cytotoxic to cancer cells in vitro and retards tumor growth in xenografts. Unlike the cytosolic HSP90 inhibitor 17-AAG, Gamitrinib specifically inhibited the expression of proteins related to OxPhos and MitoBiogenesis, but not the clients of cytosolic HSP90 (Supplemental Figure 5G).

Gamitrinib administered at 1 or 2.5 μM , in combination with MAPKi, resulted in a more remarkable induction of apoptosis and cell death compared with that observed with either Gamitrinib or

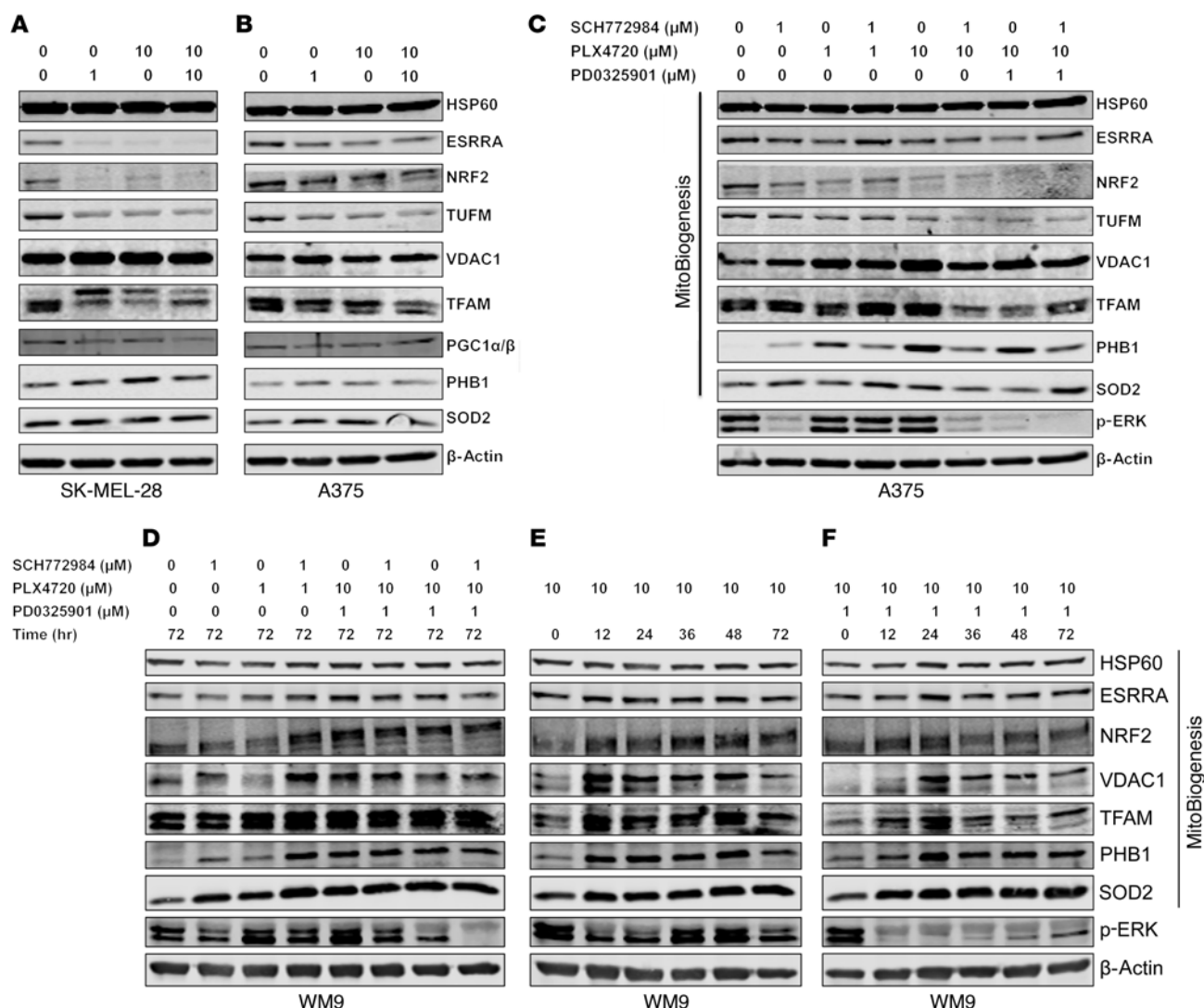


Figure 5. MAPKi regulate the expression of MitoBiogenesis in BRAF-mutated melanoma cell lines at the protein level. (A–F) Immunoblotting of proteins related to MitoBiogenesis and the MAPK pathway in SK-MEL-28 (A), A375 (B and C), and WM9 (D–F) cells treated with DMSO or the indicated MAPKi for 72 hours.

MAPKi alone (Figure 9A). Intriguingly, specific siRNAs targeting *TFAM*, *TRAP1*, *PPRC1*, and *ESRRA*, but not *PGC1A*, substantially augmented the efficacy of MAPKi and emerged as top hits. The effects of these siRNAs were comparable to those of Gamitrinib when administered at 1 or 2.5 μM (Figure 9A).

Next, we proved that siRNAs targeting *TRAP1* or *TFAM* suppressed the expression of MitoBiogenesis in surviving cells that was induced by MAPKi (Table 5 and Figure 9B). We also demonstrated that, although 2 siRNA clones targeting *PGC1A* were able to inhibit the expression of MitoBiogenesis in WM9 control cells, unexpectedly, these clones failed to further augment MAPKi-induced apoptosis and cell death (Figure 9A) and to inhibit the expression of MitoBiogenesis in WM9 surviving cells (Table 6).

It is known that the *PGC1A/PGC1B/PPRC1/NRF1/ESRRA* signaling axis is essential for the regulation of *TFAM* in order to drive mitochondrial biogenesis. Taken together, our data now pointed to a core network consisting of *PPRC1/ESRRA/TFAM* and demonstrated that the loss of each component of this net-

work augmented the increase in apoptosis and cell death when combined with MAPKi. Our data based on 2 siRNA clones targeting *TRAP1* and the mitochondrial HSP90 inhibitor Gamitrinib were consistent and of particular interest, because *TRAP1* was proven to be the target of Gamitrinib. Furthermore, our data suggested that there might be a switch in the regulation of mitochondrial biogenesis from *PGC1A* to *TFAM* and/or *TRAP1*, particularly in surviving cells.

Gamitrinib inhibited MitoBiogenesis and tumor bioenergetics. To identify the optimal combination therapy that would trigger a greater induction of apoptosis and cell death, we conducted an additional selective drug screen. In addition to Gamitrinib, we included (a) 2 mTOR inhibitors, rapamycin and BEZ235, because another mTOR inhibitor, AZD8055, inhibits OxPhos by suppressing *PGC1α* (37); (b) Phenformin, which has been implicated in inhibiting the mitochondrial respiratory complex I (17); (c) 2,4-dinitrophenol (2,4-DNP), which has been implicated as a mitochondrial uncoupler (13); and (d) the autophagy inhibitor spautin-1.

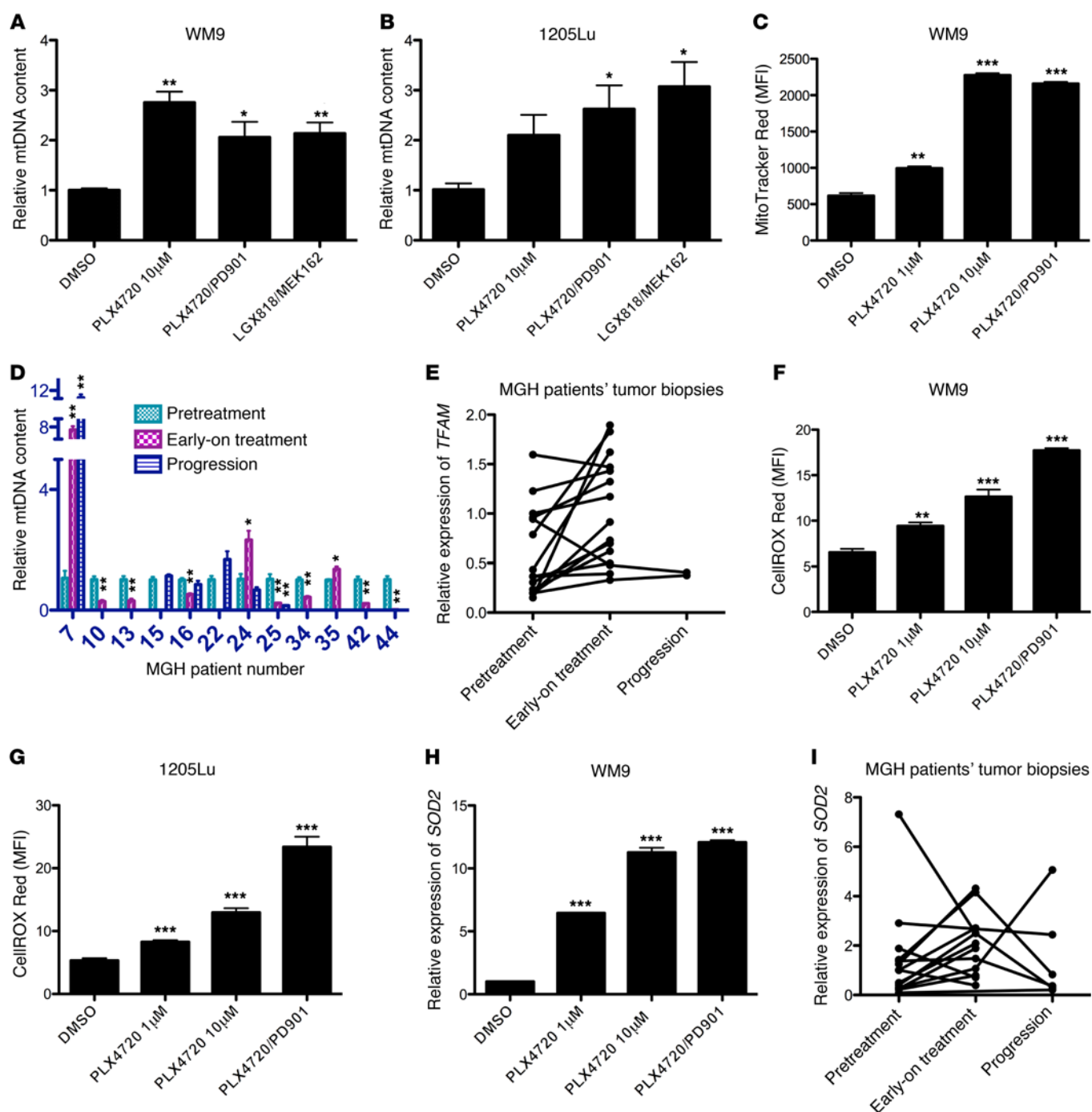


Figure 6. MAPKi increase mtDNA copy numbers, mitochondrial mass, ROS, and expression of *SOD2* in a subset of BRAF-mutated melanoma cell lines and patients' tumor biopsies. (A and B) Relative mtDNA copy numbers in WM9 (A) and 1205Lu (B) cells treated with DMSO or the indicated MAPKi for 72 hours. (C) MFI for MitoTracker Red in WM9 cells treated with DMSO or the indicated MAPKi for 72 hours. (D) Relative mtDNA copy numbers in patients' tumor biopsies. Each patient's pretreatment tumor biopsy was used as an internal control. (E) Relative gene expression of *TFAM* determined by qRT-PCR in patients' tumor biopsies. (F and G) MFI of CellROX Deep Red in WM9 (F) and 1205Lu (G) cells treated with DMSO or the indicated MAPKi for 72 hours. (H and I) Relative gene expression of *SOD2* determined by qRT-PCR in samples included in F and in patients' tumor biopsies (I). (A–C and F–H) $n = 3$ biological replicates; data are representative of 2 independent experiments. (E and I) The pretreatment tumor biopsy from MGH patient 5 was used as a control for all other samples. $n = 3$ technical replicates; data represent the average. (C, F, and G) Data were normalized to the MFI derived from the unstained sample in each experimental condition. $n = 3$ (biological replicates); data are representative of 2 independent experiments. (D, E, and I) $n = 3$ technical replicates. (A–D and F–H) $*P < 0.05$, $**P < 0.005$, and $***P < 0.0005$, by 2-tailed, unpaired t test.

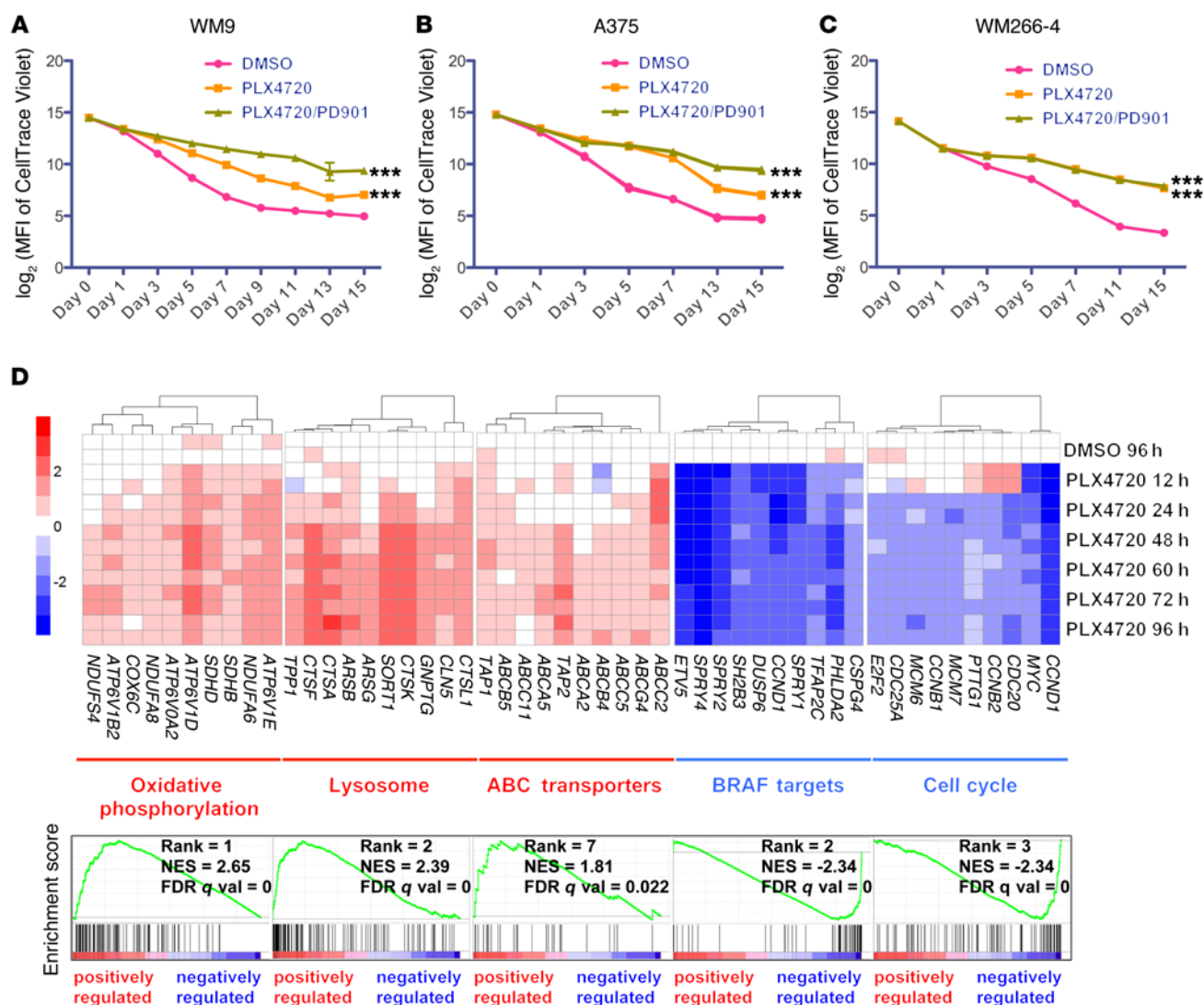


Figure 7. Surviving cells adopt a slow-growing phenotype and activate OxPhos, lysosomes, and ABC transporters in response to MAPKi. (A–C) Log₂ transformation of the MFI of CellTrace Violet in WM9 (A), A375 (B), and WM266-4 (C) cells treated with DMSO or the indicated MAPKi for 15 days. *n* = 3 biological replicates; data are representative of 2 independent experiments. ****P* < 0.0005, by 2-way ANOVA. (D) WM9 cells were treated with 10 μM DMSO or PLX4720, and cells were harvested at 12, 24, 48, 60, 72, and 96 hours for a time-course gene expression microarray study. Upper panel: heatmaps of 10 significantly altered genes chosen from each of 5 gene sets. Lower panel: GSEA plots of the 5 top-ranked gene sets shown in the upper panel. WM9 cells treated with DMSO for 96 hours were included as a control. NES, normalized enrichment score.

Our data showed that the combination of Gamitrinib or Phenformin and MAPKi led to a greater increase in apoptosis and cell death, outperforming other inhibitors (Figure 10A). We focused on Gamitrinib in subsequent studies, because our previous studies had explored the combination of Phenformin and MAPKi. However, the combination of Gamitrinib and MAPKi has not been investigated yet. This novel combination therapy was subsequently tested in 22 of our own BRAF-mutated melanoma cell lines, and we showed that it led to a greater increase in apoptosis and cell death than did MAPKi alone in many cell lines (Figure 10B).

The prolonged combination of Gamitrinib and PLX4720 substantially inhibited the viability of WM9 cells compared with that of cells treated with PLX4720 alone, suggesting that the upfront combination therapy was able to overcome the acquisition of drug resistance to PLX4720 (Figure 10C).

To gain mechanistic insights into this combination therapy, we conducted a reverse-phase protein array (RPPA) experiment. The analysis of RPPA data showed that Gamitrinib caused a significant reduction in expression of the mitochondrial respiratory chain complex subunits SDHA, SDHB, UQCRC2, ATP5H, and cyclophilin D, which were induced by MAPKi (Figure 10D and Supplemental Figure 6, A and B). The RPPA data were corroborated by immunoblotting data showing that all 5 mitochondrial respiratory chain complex subunits were downregulated by Gamitrinib (Figure 10E). Importantly, we demonstrated that Gamitrinib inhibited the expression of MitoBiogenesis that was enhanced by MAPKi (Table 7).

To elucidate the biological consequences of this combination therapy, we treated WM9 cells with a combination of Gamitrinib and MAPKi (PLX4720 plus PD0325901 or LGX818 plus MEK162)

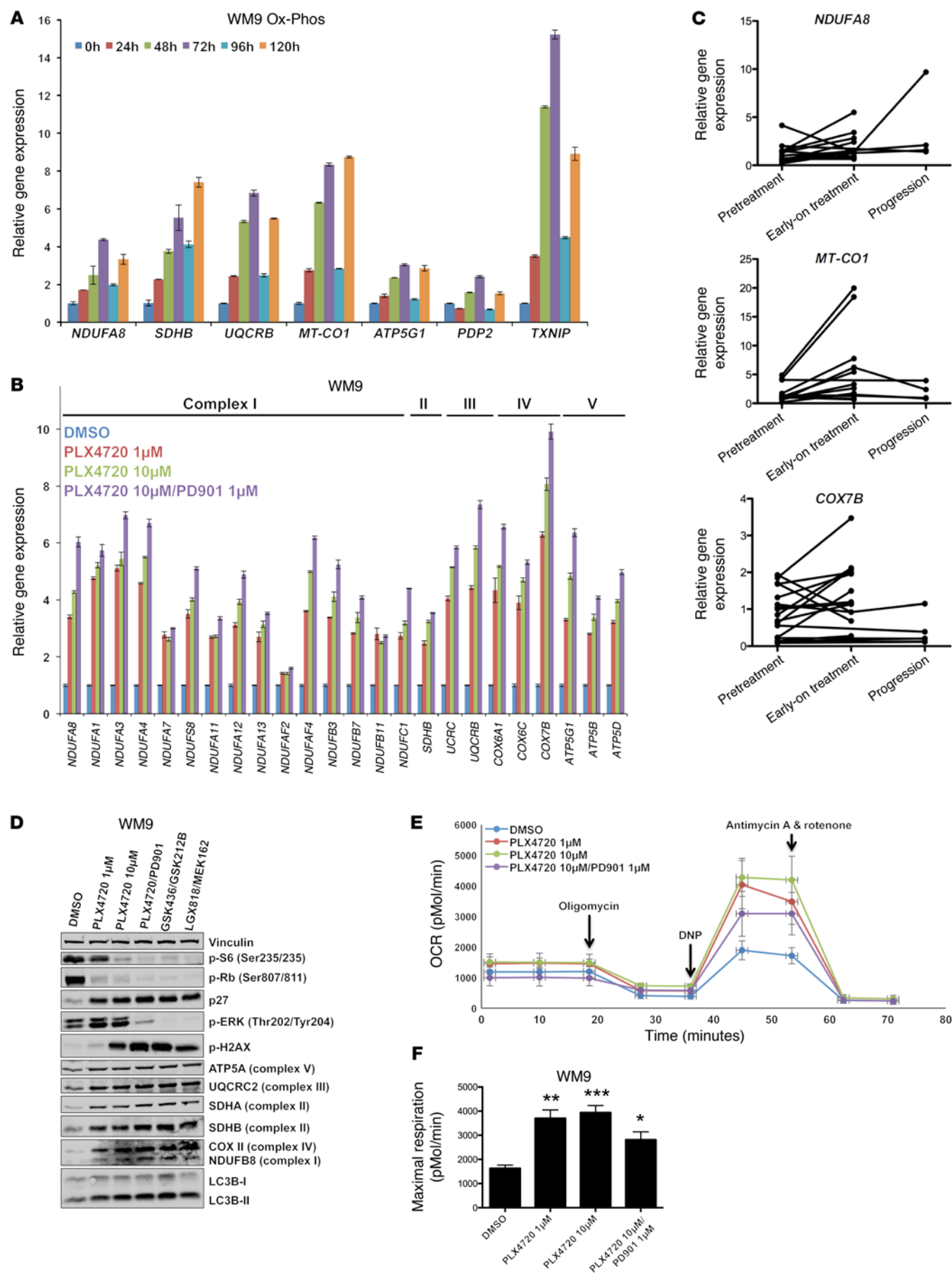


Figure 8. Surviving cells and patients' early-on treatment tumor biopsies highly express mitochondrial respiratory chain complex subunits and increase maximal respiration. (A–C) Relative gene expression of the indicated genes was determined by qRT-PCR in WM9 cells treated with 10 μ M PLX4720 for 120 hours and harvested at the indicated time points (A); in WM9 cells treated for 72 hours with DMSO or the indicated MAPKi (B); and in patients' tumor biopsies (C). $n = 3$ technical replicates; data are representative of 2 independent experiments. (C) The pretreatment tumor biopsy from MGH patient 2 was used as the baseline for all other samples. (D) Immunoblot analysis of proteins in WM9 cells treated with DMSO or the indicated MAPKi for 72 hours. (E) Mitochondrial respiration, indicated as the OCR of WM9 cells treated with the indicated MAPKi for 72 hours, was measured by a Seahorse XF24 Analyzer. Coupled and maximal respirations were determined by the sequential addition of oligomycin, DNP, and antimycin and rotenone, respectively. Data are representative of 4 biological replicates. (F) Maximal respiration measured in the samples in E. * $P < 0.05$, ** $P < 0.005$, and *** $P < 0.0005$, by 2-tailed, unpaired t test.

and found that the combination led to decreases in mtDNA content (Figure 11, A and B) and mitochondrial mass (Figure 11C). We also profiled the metabolic activities of WM9 cells that were treated with the combination of MAPKi (PLX4720, PLX4720 plus PD0325901, or LGX818 plus MEK162) and Gamitrinib by testing for real-time oxygen consumption rates (OCRs). Gamitrinib inhibited all key OCR parameters, including basal respiration, proton leak, ATP production, maximal respiration, and spare respiratory capacity, compared with what was seen in the control cells that were not treated with Gamitrinib (Figure 11, D and E, and Supplemental Figure 6C).

The combination of Gamitrinib and PLX4720 substantially downregulated the expression of *HK1*, *HK2*, *PDHE1*, *PDK1*, *PDK2*, *LDHA*, *PKM1*, *GLUT1*, and *GLUT3*, all of which are key regulators of aerobic glycolysis (Figure 10E and Figure 11F). This was in line with the decrease in the uptake of an analog of glucose, 2-NBDG, when WM9 cells were treated with the combination of Gamitrinib and PLX4720 (Figure 11G).

Collectively, RPPA and immunoblotting data also showed that Gamitrinib downregulated LC3B-II and p-S6 and upregulated p-AMPK α . The upregulation of p-AMPK α was indicative of metabolic stress, which was probably due to a decrease in the cellular ratio of ATP over ADP (Figure 10, D and E). In fact, the combination of Gamitrinib and PLX4720 led to a significant decrease in ATP production (Figure 11H).

The *M-MITF/PGC1A* signaling axis is important in regulating mitochondrial biogenesis and OxPhos in BRAF-mutated melanoma cells (13, 37). Although our data did not support a direct role of *PGC1A* in the regulation of MitoBiogenesis, we showed that in surviving cells, Gamitrinib downregulated both *PGC1A* and *M-MITF*, which were upregulated by MAPKi (Table 7 and Supplemental Figure 5D).

Taken together, our data not only showed that the combination of Gamitrinib and MAPKi phenocopied the combination of siRNAs targeting *TFAM* or *TRAP1* and MAPKi, but also demonstrated that targeting MitoBiogenesis was effective in improving the efficacy of MAPKi and preventing the acquisition of drug resistance to MAPKi. The finding that Gamitrinib was able to convert the survival into apoptosis and cell death prompted us to investigate the molecular mechanisms underlying the efficacy of the combination of Gamitrinib and MAPKi.

The combination of Gamitrinib and MAPKi resulted in mitochondrial dysfunction and inhibited tumor growth. The decrease in oxygen consumption demonstrated by melanoma cells that were treated with the combination of MAPKi and Gamitrinib suggested that mitochondrial respiration was inhibited and that the electron transport chain did not function properly. We hypothesized that the ROS production increased because electrons would leak from the electron transport chain and prematurely react with oxygen. Indeed, the combination of MAPKi and Gamitrinib led to a marked increase in ROS production compared with that of cells treated with MAPKi alone (Figure 12A). This indicated that the combination of Gamitrinib and MAPKi resulted in mitochondrial dysfunction and oxidative stress elevation.

For cells to survive under oxidative stress, SOD2 is normally induced to regulate the detoxification of mitochondrial ROS. Interestingly, the combination of Gamitrinib and MAPKi led to the upregulation of SOD2 compared with that observed in cells treated with MAPKi alone (Figure 12, B and C). By blocking oxidative stress with an ROS scavenger, *N*-acetyl-L-cysteine (NAC), we demonstrated that NAC markedly suppressed the apoptosis and cell death that were induced by the combination of Gamitrinib and MAPKi (Figure 12D). This suggested that enhancing oxidative stress beyond a tolerable threshold would determine how the combination of Gamitrinib and MAPKi causes the mitochondrial dysfunction that leads to apoptosis and cell death.

Next, we tested the *in vivo* efficacy of the combination of PLX4720 and Gamitrinib using 2 xenograft models bearing 1205Lu and WM9 melanoma cells. Because of its antimelanoma activity as a single agent (13), we first tested the antitumor activity of the combination of the mitochondrial uncoupler 2,4-DNP and PLX4720. Our data showed that 2,4-DNP failed to inhibit tumor growth and that the combination of 2,4-DNP and PLX4720 did not result in a greater effect when compared with PLX4720 in 1205Lu xenografts (Figure 12E and Supplemental Table 3). Next, we tested the antitumor activity of the combination of Gamitrinib and PLX4720 in both 1205Lu and WM9 xenografts. Gamitrinib administered at 15 mg/kg alone or combination with PLX4720 significantly impaired the tumor growth of 1205Lu and WM9 xenografts (Figure 12, F and G, and Supplemental Tables 4 and 5).

Targeting MitoBiogenesis and tumor bioenergetics was effective in a subset of acquired-resistance, BRAF-mutated tumor cells. Next, to investigate the clinical relevance of MitoBiogenesis and tumor bioenergetics in the context of acquired drug resistance, we analyzed genome-wide gene expression data available from 5 publicly available data sets (GEO GSE50535, GSE61992, GSE50509, GSE65185, and European Genome-Phenome Archive [EGA] EGAS00001000992) by performing ssGSEA, which collectively profiled paired pre- and post-treatment tumor biopsies from 153 melanoma patients whose BRAF-mutated tumors relapsed with MAPKi treatment.

In GSE50535, the expression of MitoBiogenesis, glycolysis and gluconeogenesis, and OxPhos was increased in the post-treatment tumor biopsy from patient 3 (Figure 13A). In GSE50509, the expression of MitoBiogenesis was increased in post-treatment tumor biopsies derived from patients 3, 4, 9, 10, 17, 18, 23, 28, and 30; the expression of glycolysis and gluconeogenesis

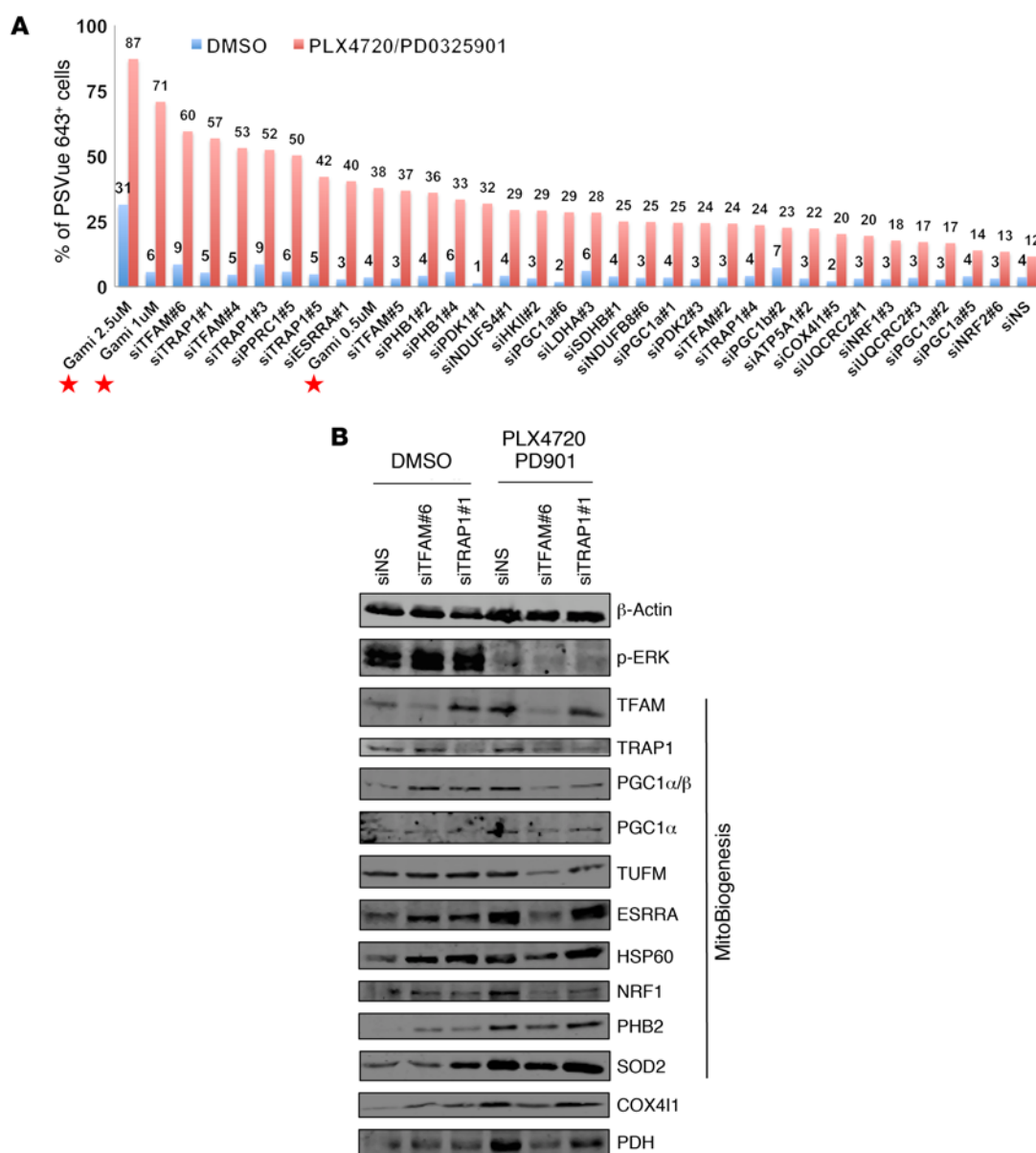


Figure 9. Knockdown of *TFAM* or *TRAP1* improves the efficacy of MAPKi. (A) Percentage of PSVue 643⁺ WM9 cells that were transfected with the indicated siRNA clone and treated with MAPKi for 72 hours. Cells transfected with siNS (nontargeting sequence) were included as a negative control. Gamitrinib, used at 0.5, 1, and 2.5 μM, is indicated by a red star in the graph. The average of 2 biological replicates was plotted, and data are representative of 2 independent experiments. Gami, Gamitrinib. **(B)** Immunoblot analysis of proteins in WM9 cells transfected with siTFAM or siTRAP1 and treated with DMSO or the indicated MAPKi for 72 hours.

genesis was increased in post-treatment tumor biopsies derived from patients 2, 3, 4, 7, 10, 14, 25, and 28; and the expression of OxPhos was increased in post-treatment tumor biopsies derived from patients 3, 7, 9, 10, 12, 18, 21, 25, 28, and 30 (Figure 13B). In GSE61992, the expression of MitoBiogenesis was increased in post-treatment tumor biopsies derived from patients 3, 4, 5, 6, 7, and 9; the expression of glycolysis and gluconeogenesis was increased in post-treatment tumor biopsies derived from patients 1, 2, 4, 6, 7, 9, and 10; and the expression of OxPhos was increased in post-treatment tumor biopsies derived from patients 1, 4, and 9 (Figure 13C). In GSE65185, the expression of MitoBiogenesis was increased in post-treatment tumor biopsies

derived from patients 1, 2, 3, 5, 8, 9, 10, 17, and 21; the expression of glycolysis and gluconeogenesis was increased in post-treatment tumor biopsies derived from patients 1, 2, 5, 6, 9, 10, 15, 17, 19, 20, 21, and 24; and the expression of OxPhos was increased in post-treatment tumor biopsies derived from patients 1, 2, 8, 9, 10, 15, 16, 17, 18, 19, 23, and 24 (Figure 13D). In EGAS00001000992, the expression of MitoBiogenesis was not increased in any of the post-treatment tumor biopsies from patients; the expression of glycolysis and gluconeogenesis was increased in the post-treatment tumor biopsy from patient 16; and the expression of OxPhos was increased in the post-treatment tumor biopsy from patient 25 (Supplemental Figure 7).

Table 5. Relative expression of 18 MitoBiogenesis genes in WM9 cells that were transfected with siTFAM or siTRAP1 and treated with MAPKi for 72 hours

siRNA	Drug	<i>PPARGC1A</i>	<i>PPARGC1B</i>	<i>PPRC1</i>	<i>NRF1</i>	<i>NFE2L2</i>	<i>ESRRA</i>	<i>TFAM</i>	<i>TFB1M</i>	<i>TFB2M</i>	<i>PHB1</i>	<i>PHB2</i>	<i>DRP1</i>	<i>FIS1</i>	<i>MFN1</i>	<i>MFN2</i>	<i>POLGA</i>	<i>POLGB</i>	<i>Twinkle</i>
siNS	DMSO	1.0	1.0	1.0	1.0	1.0	1.0	1.0	1.0	1.0	1.0	1.0	1.0	1.0	1.0	1.0	1.0	1.0	1.0
siTRAP1 #1	DMSO	1.5	1.6	0.4	1.0	0.2	2.0	13.3	5.6	5.5	0.6	3.1	1.9	2.1	1.8	1.6	0.003	1.2	0.015
siTFAM #6	DMSO	1.9	39.7	0.1	0.7	0.1	4.9	0.8	3.1	1.8	0.1	1.4	1.6	4.6	1.1	1.3	0.002	1.3	0.009
siNS	PLX4720/ PD901	393.0	457.1	2.3	6.2	9.1	81.6	14.5	3.3	4.0	35.2	17.1	10.2	14.3	15.9	15.3	0.000	1.6	0.007
siTRAP1 #1	PLX4720/ PD901	63.9	40.1	0.3	0.0	0.0	7.9	1.4	0.5	0.5	0.2	0.0	0.0	0.1	0.0	0.0	0.001	4.4	0.046
siTFAM #6	PLX4720/ PD901	133.7	4.3	0.7	1.1	10.2	15.3	2.4	1.0	1.3	9.8	2.0	2.1	0.9	0.5	0.7	0.000	1.8	0.001

Red: ≥ 2 -fold increase compared with cells transfected with siNS and treated with DMSO; blue: ≤ 2 -fold decrease compared with cells transfected with siNS and treated with the combination of 10 μ M PLX4720 and 1 μ M PD0325901.

Additionally, we performed immunohistochemical staining of TFAM, TRAP1, and MT-CO1 in paired pre- and post-treatment tumor biopsies. Compared with the paired pretreatment tumor biopsies, TFAM expression was substantially increased in 3 (University of Pennsylvania patient [Penn] 11-47, Penn 12-148, and Penn 503) of 9 post-treatment tumor biopsies (Figure 14A and Supplemental Table 6); TRAP1 expression was substantially increased in 3 (Penn 11-35, Penn 12-148, and Penn 503) of 9 post-treatment tumor biopsies (Figure 14B and Supplemental Table 6); and MT-CO1 expression was substantially increased in 1 early-on treatment tumor biopsy (MGH patient 24) as well as in 5 (MGH patients 9, 20, and 26 and Penn patients 11-3 and 578) of 18 post-treatment tumor biopsies (Figure 14C, Table 2, and Supplemental Table 6).

To investigate the prognostic values of mitochondrial biogenesis genes, we performed a Cox regression analysis and found that (a) patients with higher expression of *DNM1L*, *HSPD1*, or *VDAC1* in pretreatment tumor biopsies would likely experience faster disease progression; (b) patients with increased expression of *DNM1L* or *MFN1* in post-treatment tumor biopsies would likely experience slower disease progression; (c) patients with higher expression of *VDAC1* in pretreatment tumor biopsies would likely have a worse overall survival; and (d) patients with higher expres-

sion of *TUFM* in post-treatment tumor biopsies would likely have a worse overall survival (Supplemental Tables 7–10).

Finally, we tested whether cell lines with acquired resistance to BRAF-targeted therapies or immune checkpoint inhibitors are susceptible to Gamitrinib. All cell lines except WM4265-1 and WM4265-2 acquired resistance to MAPKi. WM4265-1 and WM4265-2 cell lines were established from 2 PDX models that were derived from 2 different brain metastatic lesions that were surgically removed from a patient after this patient continued to progress on multiple therapies including cisplatin, vinblastine, temozolomide, interleukin-2, interferon alfa-2b, ipilimumab, and pembrolizumab. In fact, Gamitrinib significantly induced apoptosis and cell death in 18 of 23 resistant cell lines (Figure 14D).

In conclusion, our data show that MitoBiogenesis and tumor bioenergetics are highly upregulated in a subset of resistant tumors. Our data suggest that patients who are refractory to MAPKi treatment may benefit from the addition of Gamitrinib to their second-line therapies to overcome acquired drug resistance (Figure 14E).

Discussion

In this study, we elucidated the role of MitoBiogenesis in mediating both intrinsic and acquired resistance to MAPKi. Our results demonstrate the existence of intrinsically resistant BRAF^{V600E} mel-

Table 6. Relative expression of 18 MitoBiogenesis genes in WM9 cells that were transfected with siPPARGC1 α and treated with MAPKi for 72 hours

siRNA	Drug	<i>PPARGC1A</i>	<i>PPARGC1B</i>	<i>PPRC1</i>	<i>NRF1</i>	<i>NFE2L2</i>	<i>ESRRA</i>	<i>TFAM</i>	<i>TFB1M</i>	<i>TFB2M</i>	<i>PHB1</i>	<i>PHB2</i>	<i>DRP1</i>	<i>FIS1</i>	<i>MFN1</i>	<i>MFN2</i>	<i>POLGA</i>	<i>POLGB</i>	<i>Twinkle</i>
siNS	DMSO	1.0	1.0	1.0	1.0	1.0	1.0	1.0	1.0	1.0	1.0	1.0	1.0	1.0	1.0	1.0	1.0	1.0	1.0
siPPARGC1 α #2	DMSO	0.2	0.3	0.5	0.3	0.5	0.1	0.6	0.5	0.7	1.1	0.5	0.5	0.8	0.5	0.9	1.7	1.0	0.5
siPPARGC1 α #5	DMSO	0.5	0.3	0.9	0.5	0.4	0.6	0.6	0.5	0.5	0.7	0.3	0.6	0.4	0.6	0.3	0.2	1.1	1.0
siNS	PLX4720/ PD901	4.1	8.1	4.1	2.5	1.4	4.4	2.6	2.1	3.3	1.8	2.6	3.7	3.3	3.7	5.8	5.3	4.1	3.1
siPPARGC1 α #2	PLX4720/ PD901	2.2	11.9	10.7	2.3	2.4	1.3	4.5	1.2	3.9	4.1	3.3	4.2	4.4	4.8	8.8	10.7	5.1	4.5
siPPARGC1 α #5	PLX4720/ PD901	8.0	4.0	4.7	2.1	2.4	3.6	2.9	2.5	4.6	3.3	2.3	3.3	4.5	3.8	8.6	5.3	6.0	4.6

Red: ≥ 2 -fold increase compared with cells transfected with siNS and treated with DMSO; blue: ≤ 2 -fold decrease compared with cells transfected with siNS and treated with the combination of 10 μ M PLX4720 and 1 μ M PD0325901.

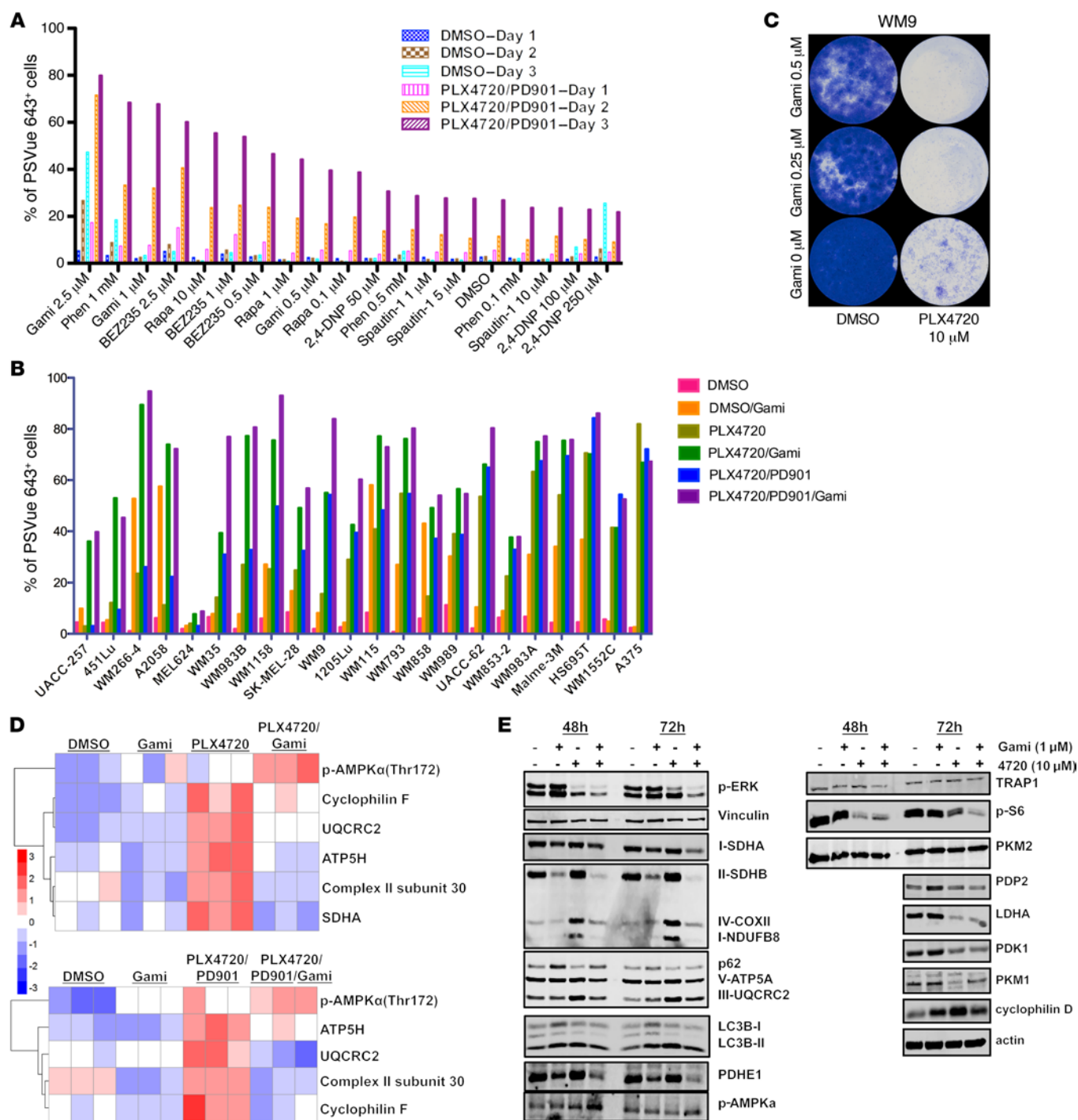


Figure 10. Gamitrinib suppresses MitoBiogenesis and tumor bioenergetics. (A) Percentage of PSVue 643⁺ WM9 cells treated with DMSO or the indicated MAPKi in combination with Gamitrinib (Gami), rapamycin (Rapa), Phenformin (Phen), BEZ235, 2,4-DNP, or Spautin-1 for 72 hours and harvested on days 1, 2, and 3 for FACS analysis. (B) Percentage of PSVue 643⁺ cells in 22 BRAF-mutated melanoma cell lines treated with a combination of the indicated MAPKi and Gamitrinib for 72 hours (PLX4720, 10 μ M; PD901, 1 μ M; Gamitrinib, 2.5 M). (A and B) Cells treated with DMSO were used as a control. The average of 2 biological replicates was plotted, and data are representative of 2 independent experiments. (C) Long-term cell growth assay of WM9 cells treated with 10 μ M DMSO or PLX4720 in combination with Gamitrinib for 15 days. Cells were fixed and stained with crystal violet on day 15. Data are representative of 2 independent experiments. (D) Two heatmaps of RPPA data on WM9 cells treated with DMSO or the indicated MAPKi in combination with 1 μ M Gamitrinib for 72 hours. Upper panel: PLX4720, 10 μ M; lower panel: PLX4720, 10 μ M and PD0325901, 1 μ M. $n = 3$ biological replicates. (E) Immunoblot analysis of proteins in WM9 cells treated with 10 μ M DMSO or PLX4720, with or without 1 μ M Gamitrinib, for 72 hours.

Table 7. Relative expression of 18 MitoBiogenesis genes in WM9 cells that were treated with a combination of MAPKi and Gamitrinib

Drug	<i>PPARGC1A</i>	<i>PPARGC1B</i>	<i>PPRC1</i>	<i>ESRRA</i>	<i>NRF1</i>	<i>NFE2L2</i>	<i>TFAM</i>	<i>TFB1M</i>	<i>TFB2M</i>	<i>POLGA</i>	<i>POLGB</i>	<i>Twinkle</i>	<i>PHB1</i>	<i>PHB2</i>	<i>DRP1</i>	<i>FIS1</i>	<i>MFN1</i>	<i>MFN2</i>
DMSO	1.0	1.0	1.0	1.0	1.0	1.0	1.0	1.0	1.0	1.0	1.0	1.0	1.0	1.0	1.0	1.0	1.0	1.0
Gami	1.4	0.8	0.9	1.0	0.8	0.5	0.7	1.1	0.7	0.6	1.2	0.5	0.6	0.6	0.7	0.9	0.9	0.8
PLX4720/ PD901	102.6	6.2	4.6	13.0	3.3	2.1	2.6	0.5	1.7	0.7	2.6	2.1	2.7	2.6	2.8	3.4	4.6	3.2
PLX4720/ PD901/Gami	21.6	2.7	2.0	9.9	2.0	0.5	0.9	0.2	0.5	0.1	0.5	0.7	1.1	1.1	0.9	1.4	2.0	1.6

Red: ≥ 2 -fold increase compared with cells treated with DMSO alone; blue: ≤ 2 -fold decrease compared with cells treated with a combination of 10 μ M PLX4720 and 1 μ M PD0325901.

anoma cells that activate mitochondrial biogenesis and OxPhos to meet their bioenergetic needs and to survive MAPKi. Our study establishes the molecular basis for how mitochondrial biogenesis underlies and couples both intrinsic and acquired drug resistance. Furthermore, our data pave the way for combining Gamitrinib with MAPKi to trigger synthetic lethality.

We found that the MitoBiogenesis gene signature is primarily expressed in a subset of melanoma cell lines or tumors. MAPKi downregulate MitoBiogenesis in sensitive melanoma cell lines with high basal levels of MitoBiogenesis and upregulate MitoBiogenesis in resistant melanoma cell lines with low basal levels of MitoBiogenesis. Intrinsically resistant cells that highly express mitochondrial biogenesis have high mtDNA copy numbers, mitochondrial mass, and OCRs and produce more ROS. Clinically, the expression of MitoBiogenesis and mtDNA content is highly upregulated in early-on treatment tumor biopsies from a subset of patients.

We uncovered a dynamic expression profile change in intrinsically resistant cells responding to MAPKi and identified 3 major pathways, OxPhos, autophagy/lysosomes, and ABC transporters, that may confer the intrinsic resistance phenotype. Interestingly, *KRAS*-mutant pancreatic cancer cells also depend on OxPhos for survival when the mutant *KRAS* is blunted (30).

To pinpoint the causal and passive roles of MitoBiogenesis, tumor bioenergetics, and autophagy in underlying intrinsic resistance, we performed selected siRNA- and drug-based screens. The autophagy inhibitor and siRNAs against representative mitochondrial respiratory chain subunits did not enhance the apoptosis and cell death that were induced by MAPKi. We reason that it is possible that redundant or alternative pathways are activated to compensate for the genetic and pharmacologic inhibition. Importantly, we demonstrate that the depletion of *TFAM* or *TRAP1*, but not *PGC1A*, synergizes with MAPK. Our data underscore the idea that a core signaling network involving *PPRC1*, *ESRRA*, and *TFAM* confers resistance to MAPKi. *TRAP1* is exclusively located in mitochondria and controls proper mitochondrial protein folding and integrity. The potent effect of the combination of si*TRAP1* and MAPKi encouraged us to test the efficacy of Gamitrinib, which is designed to target TRAP1 (mitochondrial HSP90) in inhibiting MitoBiogenesis.

The combination of Gamitrinib and MAPKi results in an unparalleled synthetic lethality, outperforming many other metabolic inhibitors, except Phenformin. We further demonstrate that the combination of Gamitrinib and MAPKi downregulates

TFAM, *PGC1A*, and *M-MITF* and impairs many key parameters of mitochondrial biogenesis as well as glucose uptake and ATP production. The combination of Gamitrinib and MAPKi leads to an increase in mitochondrial oxidative stress that is beyond the tolerable threshold for cell detoxification and survival. Our data support the use of Gamitrinib as an effective therapeutic option to inhibit aberrant tumor metabolism. A recent study showed the efficacy of BCL2 inhibition by targeting OxPhos to eradicate leukemia stem cells with low ROS and warrants the investigation of its efficacy in targeting resistant melanoma cells (38).

We show that Gamitrinib not only circumvents the acquisition of resistance to MAPKi but also impairs the viability of cells with acquired resistance. Furthermore, our data show that, in progressive tumor biopsies from a subset of patients, the expression of MitoBiogenesis and tumor bioenergetics is upregulated.

The clinical relevance of mitochondrial biogenesis, glycolysis, and OxPhos in patients with melanoma is very intriguing. TCGA melanoma patients with high expression of MitoBiogenesis or coexpression of glycolysis and OxPhos have worse overall survival rates. Thus, mitochondrial metabolism might be a tractable therapeutic target for that subset of patients. Further investigation of the expression of mitochondrial biogenesis, glycolysis, and OxPhos genes and the association with clinical status in other types of cancers is clearly warranted.

Methods

Cell lines established from human melanomas and patient-derived xenografts. See the Supplemental Methods for details.

Illumina gene expression microarray data on WM9 cells. Time-course Illumina gene expression microarray data on WM9 cells were deposited in the NCBI's GEO database (GEO GSE58721).

Melanoma xenotransplantation and in vivo studies. Ten thousand 1205Lu or WM9 cells were harvested from cell culture and resuspended in culture medium and Matrigel at a 1:1 ratio. Cells were s.c. injected into mice, which were treated with the indicated inhibitors when the tumor volume reached 100 mm³. Mice were sacrificed at the end time point and solid tumors collected.

Statistics. Unless otherwise indicated, data in the figures are presented as the mean \pm SEM for 3 biological or technical replicates. Significant differences between experimental conditions were determined using a 2-tailed, unpaired *t* test. For survival data, Kaplan-Meier survival curves were generated, and their differences were examined using a log-rank test. For tumor growth data, mixed-effects models

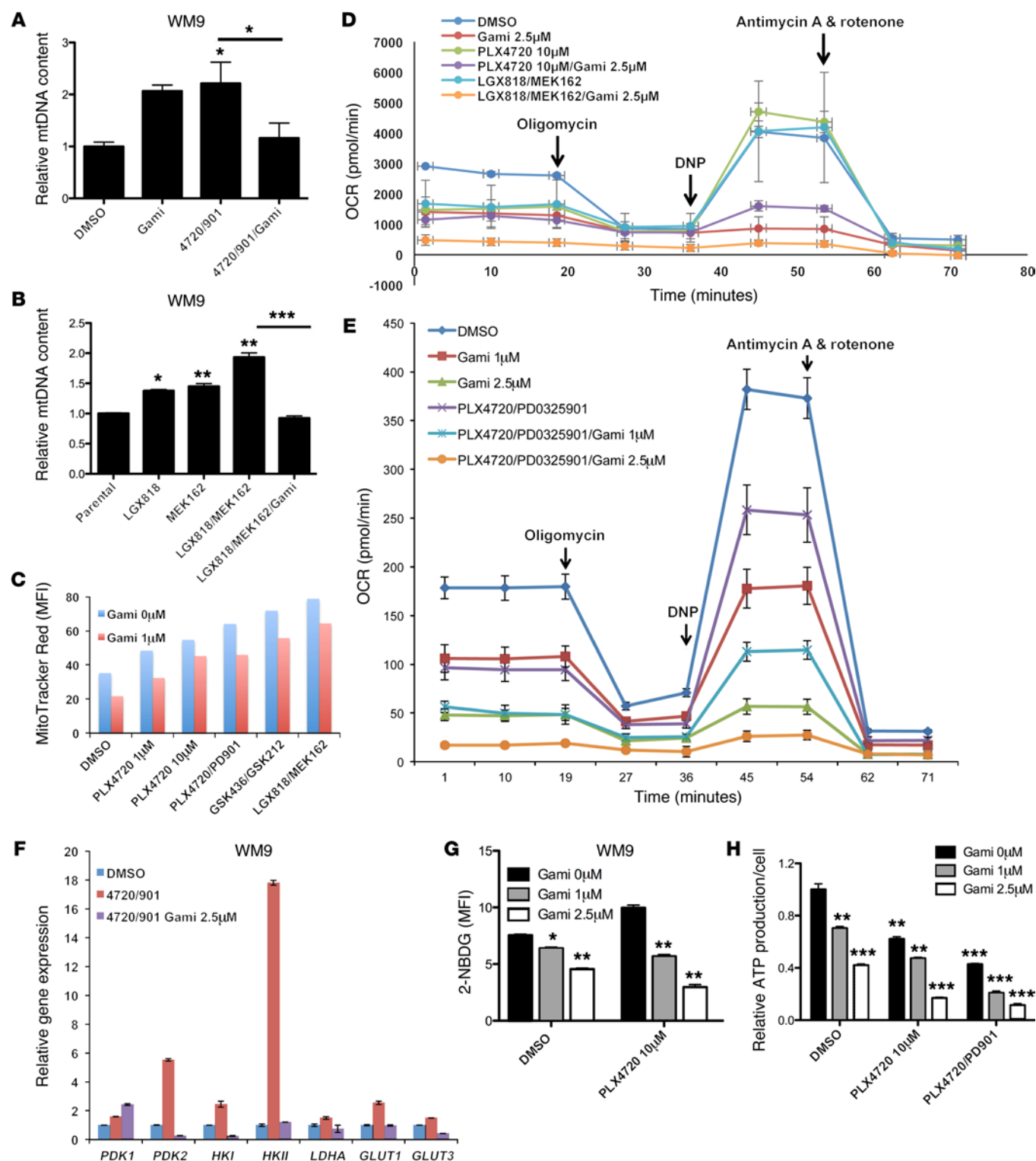
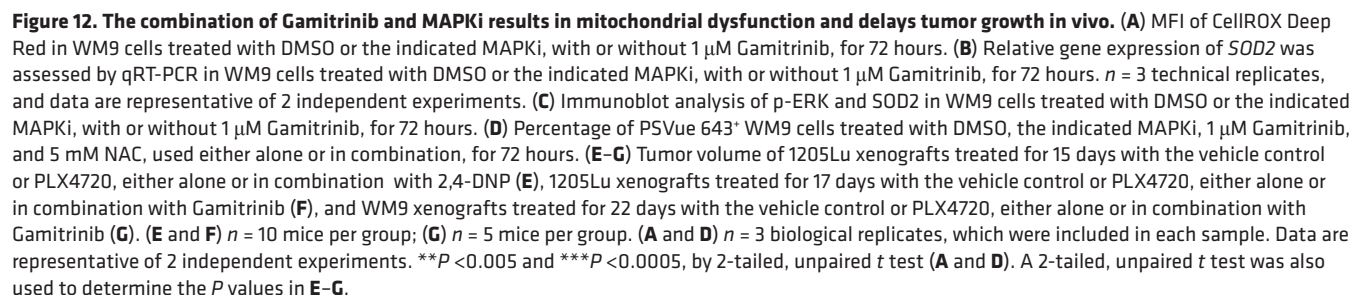
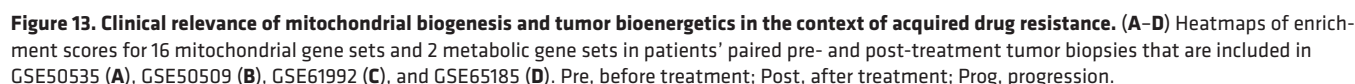


Figure 11. Gamitrinib leads to decreased mtDNA copy numbers, mass, and respiration and inhibits glycolysis and ATP production. (A and B) Relative mtDNA copy numbers in WM9 cells treated with DMSO or the indicated MAPKi, with or without 1 μM Gamitrinib, for 72 hours. (C) MFI of MitoTracker Red for WM9 cells treated for 72 hours with DMSO or the indicated MAPKi, with or without 1 or 2.5 μM Gamitrinib. *n* = 2 biological replicates, and the average was plotted. Data are representative of 2 independent experiments. (D and E) Real-time oxygen consumption of WM9 cells subjected to a metabolic stress test with a Seahorse XF 24 Analyzer. Cells were treated for 72 hours with DMSO or the indicated MAPK inhibitor, with or without 1 or 2.5 μM Gamitrinib. *n* = 4 biological replicates. (F) Relative gene expression was assessed by qRT-PCR in WM9 cells treated for 48 hours with DMSO or the indicated MAPKi, with or without 2.5 μM Gamitrinib. (G and H) MFI of 2-NBDG (G) and relative ATP production (H) in WM9 cells treated for 72 hours with DMSO or the indicated MAPKi, with or without 1 or 2.5 μM Gamitrinib. (A, B, and F) *n* = 3 technical replicates, and data are representative of 2 independent experiments. (G and H) *n* = 3 biological replicates, which were included in each sample, and the data are representative of 2 independent experiments. **P* < 0.05, ***P* < 0.005, and ****P* < 0.0005, by 2-tailed, unpaired *t* test.





Study approval. All clinical data and patients' samples were collected following IRB approval of the Massachusetts General Hospital and the Hospital of the University of Pennsylvania, and informed consent was obtained from all study participants. All animal studies were

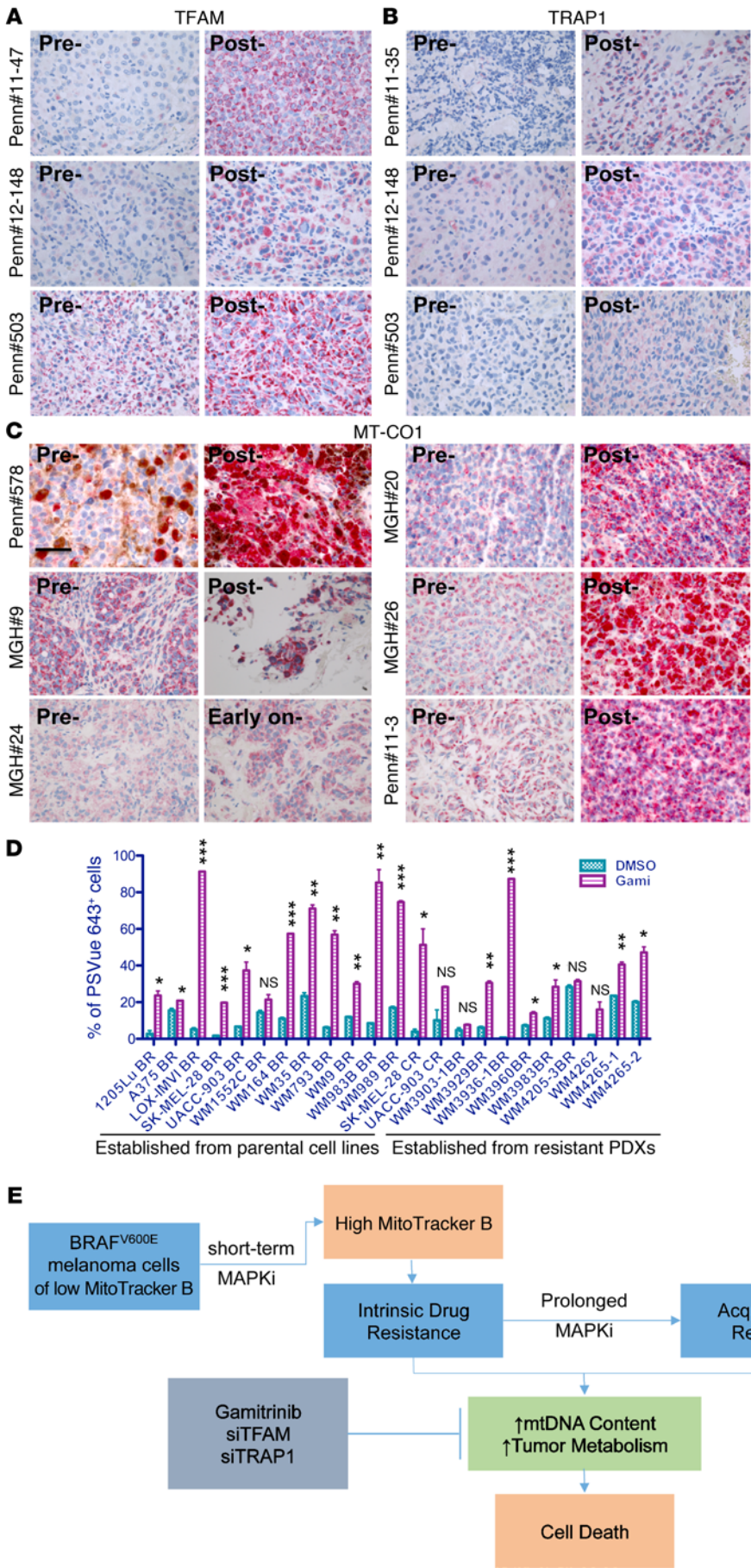


Figure 14. Increases of mitochondrial biogenesis proteins exhibited in patients' progressive tumor biopsies and targeting acquired drug resistant cells with Gamitrinib. (A–C) Immunohistochemical staining of TFAM (A), TRAP1 (B), and MT-CO1 (C) in patients' paired pre-, early-on, and post-treatment tumor biopsies. Scale bars represent 40 μ m. **(D)** Percentage of PSVue 643+ cells in 23 *BRAF*-mutated resistant melanoma cell lines that were treated with 2.5 μ M Gamitrinib for 72 hours. $n = 2$ biological replicates, which were included for each sample. Data are representative of 2 independent experiments. * $P < 0.05$, ** $P < 0.005$, and *** $P < 0.0005$, by 2-tailed, unpaired t test was used. PDXs, patient-derived xenografts. **(E)** Schematic model showing cotargeting the MAPK pathway and mitochondrial biogenesis in *BRAF*-mutated melanoma cells as a viable therapeutic strategy.

conducted in accordance with NIH animal care and use guidelines, and mice were maintained according to the guidelines of the IACUC of The Wistar Institute. All animal experiments were performed in accordance with IACUC protocol 112330 of The Wistar Institute, and the study designs were approved by the IACUC of The Wistar Institute.

Author contributions

GZ and MH designed the study. DTF, LW, CK, SS, YCC, XX, HC, ED, OO, BS, DZ, MG, MX, SR, KS, CX, AG, PB, and YL conducted experiments. ZW, SS, MG, Weiting Xu, TT, JZ, SZ, and QL analyzed data. DTF, Wei Xu, JL, GCK, LMS, TCG, and KTF provided patients' samples and clinical information. GZ and MH wrote the manuscript, with input and scientific advice from LW, BS, DB, RKA, AW, MAD, JAW, NGA, GBM, DCA, and KTF.

Acknowledgments

We thank all former and current laboratory members for their comments and helpful discussions; J. Hayden (Wistar Micro-

copy Facility), C. Chang, S. Billouin, and T. Nguyen (Wistar Genomics Facility), J.S. Faust, and D. Ambrose (Wistar Flow Cytometry Facility) for their technical support; M.B. Powell for providing human melanoma cells (Stanford University); and M.S. Soengas and E. Riveiro-Falkenbach for providing plasmids (Centro Nacional de Investigaciones Oncológicas [CNIO]). We apologize to those whose work was not cited or mentioned here due to space constraints. The research was funded by NIH grants P01 CA114046, P01 CA025874, P30 CA010815, and R01 CA047159 and by the Dr. Miriam and Sheldon G. Adelson Medical Research Foundation and the Melanoma Research Foundation. The support for Shared Resources used in this study was provided by Cancer Center Support Grant (CCSG) CA010815 (to the Wistar Institute).

Address correspondence to: Meenhard Herlyn, The Wistar Institute, 3601 Spruce Street, Philadelphia, Pennsylvania 19104, USA. Phone: 215.898.3950; E-mail: herlynm@wistar.org.

- Bhatia S, Tykodi SS, Thompson JA. Treatment of metastatic melanoma: an overview. *Oncology (Williston Park)*. 2009;23(6):488–496.
- Davies H, et al. Mutations of the BRAF gene in human cancer. *Nature*. 2002;417(6892):949–954.
- McArthur GA, et al. Safety and efficacy of vemurafenib in BRAF(V600E) and BRAF(V600K) mutation-positive melanoma (BRIM-3): extended follow-up of a phase 3, randomised, open-label study. *Lancet Oncol*. 2014;15(3):323–332.
- Flaherty KT, et al. Inhibition of mutated, activated BRAF in metastatic melanoma. *N Engl J Med*. 2010;363(9):809–819.
- Bollag G, et al. Clinical efficacy of a RAF inhibitor needs broad target blockade in BRAF-mutant melanoma. *Nature*. 2010;467(7315):596–599.
- Chapman PB, et al. Improved survival with vemurafenib in melanoma with BRAF V600E mutation. *N Engl J Med*. 2011;364(26):2507–2516.
- Flaherty KT, et al. Improved survival with MEK inhibition in BRAF-mutated melanoma. *N Engl J Med*. 2012;367(2):107–114.
- Flaherty KT, et al. Combined BRAF and MEK inhibition in melanoma with BRAF V600 mutations. *N Engl J Med*. 2012;367(18):1694–1703.
- Shi H, et al. Acquired resistance and clonal evolution in melanoma during BRAF inhibitor therapy. *Cancer Discov*. 2014;4(1):80–93.
- Whittaker SR, et al. A genome-scale RNA interference screen implicates NF1 loss in resistance to RAF inhibition. *Cancer Discov*. 2013;3(3):350–362.
- Kaplon J, et al. A key role for mitochondrial gatekeeper pyruvate dehydrogenase in oncogene-induced senescence. *Nature*. 2013;498(7452):109–112.
- Haq R, et al. BCL2A1 is a lineage-specific antiapoptotic melanoma oncogene that confers resistance to BRAF inhibition. *Proc Natl Acad Sci U S A*. 2013;110(11):4321–4326.
- Haq R, et al. Oncogenic BRAF regulates oxidative metabolism via PGC1 α and MITF. *Cancer Cell*. 2013;23(3):302–315.
- Abel EV, et al. Melanoma adapts to RAF/MEK inhibitors through FOXD3-mediated upregulation of ERBB3. *J Clin Invest*. 2013;123(5):2155–2168.
- Hanahan D, Weinberg RA. Hallmarks of cancer: the next generation. *Cell*. 2011;144(5):646–674.
- Roesch A, et al. A temporarily distinct subpopulation of slow-cycling melanoma cells is required for continuous tumor growth. *Cell*. 2010;141(4):583–594.
- Roesch A, et al. Overcoming intrinsic multidrug resistance in melanoma by blocking the mitochondrial respiratory chain of slow-cycling JARID-1B(high) cells. *Cancer Cell*. 2013;23(6):811–825.
- Vazquez F, et al. PGC1 α expression defines a subset of human melanoma tumors with increased mitochondrial capacity and resistance to oxidative stress. *Cancer Cell*. 2013;23(3):287–301.
- Alvarez-Calderon F, et al. Tyrosine kinase inhibition in leukemia induces an altered metabolic state sensitive to mitochondrial perturbations. *Clin Cancer Res*. 2015;21(6):1360–1372.
- Kelly DP, Scarpulla RC. Transcriptional regulatory circuits controlling mitochondrial biogenesis and function. *Genes Dev*. 2004;18(4):357–368.
- Gleyzer N, Vercauteren K, Scarpulla RC. Control of mitochondrial transcription specificity factors (TFB1M and TFB2M) by nuclear respiratory factors (NRF-1 and NRF-2) and PGC-1 family coactivators. *Mol Cell Biol*. 2005;25(4):1354–1366.
- Di Re M, et al. The accessory subunit of mitochondrial DNA polymerase gamma determines the DNA content of mitochondrial nucleoids in human cultured cells. *Nucleic Acids Res*. 2009;37(17):5701–5713.
- Supale S, et al. Loss of prohibitin induces mitochondrial damages altering β -cell function and survival and is responsible for gradual diabetes development. *Diabetes*. 2013;62(10):3488–3499.
- Shirendeb U, et al. Abnormal mitochondrial dynamics, mitochondrial loss and mutant huntingtin oligomers in Huntington's disease: implications for selective neuronal damage. *Hum Mol Genet*. 2011;20(7):1438–1455.
- Barretina J, et al. The Cancer Cell Line Encyclopedia enables predictive modelling of anticancer drug sensitivity. *Nature*. 2012;483(7391):603–607.
- Kabbarah O, et al. Integrative genome comparison of primary and metastatic melanomas. *PLoS One*. 2010;5(5):e10770.
- Cancer Genome Atlas Network. Genomic classification of cutaneous melanoma. *Cell*. 2015;161(7):1681–1696.
- Litvin O, et al. Interferon α/β enhances the cytotoxic response of MEK inhibition in melanoma. *Mol Cell*. 2015;57(5):784–796.
- Kokoszka JE, Coskun P, Esposito LA, Wallace DC. Increased mitochondrial oxidative stress in the Sod2 (+/-) mouse results in the age-related decline of mitochondrial function culminating in increased apoptosis. *Proc Natl Acad Sci U S A*. 2001;98(5):2278–2283.
- Viale A, et al. Oncogene ablation-resistant pancreatic cancer cells depend on mitochondrial function. *Nature*. 2014;514(7524):628–632.
- Cheng MY, Hartl FU, Horwich AL. The mitochondrial chaperonin hsp60 is required for its own assembly. *Nature*. 1990;348(6300):455–458.
- Skrtec M, et al. Inhibition of mitochondrial translation as a therapeutic strategy for human acute myeloid leukemia. *Cancer Cell*. 2011;20(5):674–688.
- Ekstrand MI, et al. Mitochondrial transcription factor A regulates mtDNA copy number in mammals. *Hum Mol Genet*. 2004;13(9):935–944.
- Kang BH, et al. Combinatorial drug design targeting multiple cancer signaling networks controlled by mitochondrial Hsp90. *J Clin Invest*. 2009;119(3):454–464.
- Chae YC, et al. Landscape of the mitochondrial Hsp90 metabolome in tumours. *Nat Commun*. 2013;4:2139.
- Chae YC, et al. Control of tumor bioenergetics and survival stress signaling by mitochondrial HSP90s. *Cancer Cell*. 2012;22(3):331–344.
- Gopal YN, et al. Inhibition of mTORC1/2 overcomes resistance to MAPK pathway inhibitors mediated by PGC1 α and oxidative phosphorylation in melanoma. *Cancer Res*. 2014;74(23):7037–7047.
- Lagadinou ED, et al. BCL-2 inhibition targets oxidative phosphorylation and selectively eradicates quiescent human leukemia stem cells. *Cell Stem Cell*. 2013;12(3):329–341.

RESEARCH ARTICLE

The Mitochondrial Unfoldase-Peptidase Complex ClpXP Controls Bioenergetics Stress and Metastasis

Jae Ho Seo^{1,2}, Dayana B. Rivadeneira^{1,2}, M. Cecilia Caino^{1,2}, Young Chan Chae^{1,2}, David W. Speicher^{1,3,4}, Hsin-Yao Tang⁴, Valentina Vaira^{5,6}, Silvano Bosari^{5,6}, Alessandro Palleschi⁷, Paolo Rampini⁸, Andrew V. Kossenkov⁴, Lucia R. Languino^{1,9}, Dario C. Altieri^{1,2*}



OPEN ACCESS

Citation: Seo JH, Rivadeneira DB, Caino MC, Chae YC, Speicher DW, Tang H-Y, et al. (2016) The Mitochondrial Unfoldase-Peptidase Complex ClpXP Controls Bioenergetics Stress and Metastasis. *PLoS Biol* 14(7): e1002507. doi:10.1371/journal.pbio.1002507

Academic Editor: Heather Christofk, University of California Los Angeles, UNITED STATES

Received: January 15, 2016

Accepted: June 10, 2016

Published: July 7, 2016

Copyright: © 2016 Seo et al. This is an open access article distributed under the terms of the [Creative Commons Attribution License](http://creativecommons.org/licenses/by/4.0/), which permits unrestricted use, distribution, and reproduction in any medium, provided the original author and source are credited.

Data Availability Statement: All relevant data are within the paper and its supporting information files.

Funding: This work was supported by the National Institutes of Health (NIH) grants (<http://grants.nih.gov>) P01 CA140043 (DCA, LRL, and DWS), R01 CA78810 and CA190027 (DCA), R01 CA089720 (LRL), F32CA177018 (MCC), the Italian Minister of Health grant (<http://www.salute.gov.it>) GR2011-02351626 (VV), the Office of the Assistant Secretary of Defense for Health Affairs through the Prostate Cancer Research Program (<http://cdmrp.army.mil/default.shtml>) under Award No. W81XWH-13-1-0193

1 Prostate Cancer Discovery and Development Program, The Wistar Institute, Philadelphia, Pennsylvania, United States of America, **2** Tumor Microenvironment and Metastasis Program, The Wistar Institute, Philadelphia, Pennsylvania, United States of America, **3** Molecular and Cellular Oncogenesis Program, The Wistar Institute, Philadelphia, Pennsylvania, United States of America, **4** Center for Systems and Computational Biology, The Wistar Institute, Philadelphia, Pennsylvania, United States of America, **5** Division of Pathology, Fondazione IRCCS Ca' Granda Ospedale Maggiore Policlinico, Milan, Italy, **6** Department of Pathophysiology and Transplantation, University of Milan, Milan, Italy, **7** Division of Thoracic Surgery, Fondazione IRCCS Ca' Granda Ospedale Maggiore Policlinico, Milan, Italy, **8** Division of Neurosurgery, Fondazione IRCCS Ca' Granda Ospedale Maggiore Policlinico, Milan, Italy, **9** Department of Cancer Biology and Kimmel Cancer Center, Thomas Jefferson University, Philadelphia, Pennsylvania, United States of America

* daltieri@wistar.org

Abstract

Mitochondria must buffer the risk of proteotoxic stress to preserve bioenergetics, but the role of these mechanisms in disease is poorly understood. Using a proteomics screen, we now show that the mitochondrial unfoldase-peptidase complex ClpXP associates with the oncoprotein survivin and the respiratory chain Complex II subunit succinate dehydrogenase B (SDHB) in mitochondria of tumor cells. Knockdown of ClpXP subunits ClpP or ClpX induces the accumulation of misfolded SDHB, impairing oxidative phosphorylation and ATP production while activating “stress” signals of 5' adenosine monophosphate-activated protein kinase (AMPK) phosphorylation and autophagy. Deregulated mitochondrial respiration induced by ClpXP targeting causes oxidative stress, which in turn reduces tumor cell proliferation, suppresses cell motility, and abolishes metastatic dissemination in vivo. ClpP is universally overexpressed in primary and metastatic human cancer, correlating with shortened patient survival. Therefore, tumors exploit ClpXP-directed proteostasis to maintain mitochondrial bioenergetics, buffer oxidative stress, and enable metastatic competence. This pathway may provide a “drugable” therapeutic target in cancer.

Author Summary

As the powerhouse of the cell and a pivotal hub for oxidative stress, mitochondria must tightly control the state of the proteins that they contain, quickly eliminating misfolded,

(DCA), and a Challenge Award from the Prostate Cancer Foundation (PCF) (<http://www.pcf.org>) to MCC, LRL, and DCA. Support for Core Facilities utilized in this study was provided by Cancer Center Support Grant (CCSG) (<http://cancercenters.cancer.gov>) CA010815 to The Wistar Institute. The funders had no role in study design, data collection and analysis, decision to publish, or preparation of the manuscript.

Competing Interests: The authors have declared that no competing interests exist.

Abbreviations: AMPK, 5' adenosine monophosphate-activated protein kinase; CS, citrate synthase; ER, endoplasmic reticulum; Hsp90, heat shock protein-90; IAP, inhibitor-of-apoptosis protein; mTOR, mechanistic target of rapamycin; NAC, N-acetylcysteine; NSCLC, non-small cell lung cancer; OCR, oxygen consumption rate; ROS, reactive oxygen species; SDHB, succinate dehydrogenase B; siRNA, small interfering RNA; TRAP-1, TNFR-associated molecule-1; UPR, unfolded protein response; VDAC, voltage-dependent anion channel.

aggregated, or otherwise damaged proteins. Here, we show that tumor mitochondria manage their set of proteins by assembling an integrated network of protein homeostasis, or proteostasis, that controls both the folding and degradation of proteins. This protein complex is formed by the unfoldase-peptidase ClpXP, survivin, and the Hsp90-like chaperone TRAP-1, and regulates the function of the oxidative phosphorylation Complex II subunit succinate dehydrogenase B (SDHB). We find that interference with this process impairs energy production, promotes oxidative stress, and shuts down critical downstream signals important for tumor cell proliferation, invasion, and metastatic dissemination *in vivo*. Our results suggest that the mitochondrial proteostasis network may offer therapeutic opportunities in advanced disease.

Introduction

The control of protein homeostasis, or proteostasis, occupies a central, evolutionary-conserved role in organismal integrity and flexible adaptation to environmental “stress” [1]. This pathway involves mechanisms of chaperone-directed protein (re)folding [2] as well as removal of aggregated or misfolded proteins via proteolytic degradation [3]. Defects in either process impair organelle function, in particular the endoplasmic reticulum (ER) [4] and mitochondria [5], activating an unfolded protein response (UPR) that may culminate in cell death and tissue damage [6].

There is also evidence that a heightened proteostatic threshold can contribute to disease, in particular cancer, by buffering the risk of proteotoxic stress associated with the biosynthetic needs of transformed cells. Accordingly, molecular chaperones of the heat shock protein-90 (Hsp90) family, including Hsp90 [7] and its homolog, TNFR-associated molecule-1 (TRAP-1) [8], become overexpressed in mitochondria of tumor cells compared to normal tissues [9] and preserve the folding and activity of key effectors of organelle homeostasis [10]. In turn, the heightened proteostatic environment prevents the emergence of a mitochondrial UPR [11], antagonizes cyclophilin D-dependent apoptosis [9], and maintains bioenergetics [10], including oxidative phosphorylation [12], correlating with unfavorable disease outcome in cancer patients [13].

What has remained unclear, however, is whether chaperone-directed protein folding is the sole mechanism of mitochondrial proteostasis in cancer [10]. In this context, mitochondria contain an evolutionary-conserved, ATP-dependent unfoldase-peptidase protein complex, ClpXP [14], which mediates proteolytic removal of misfolded proteins [15]. There is evidence that this pathway may regulate a mitochondrial UPR [16,17] and contribute to human disease pathogenesis [18].

In this study, we investigated mechanisms of mitochondrial proteostasis as a potential driver of tumor progression.

Results

Identification of ClpXP as a Novel Survivin-Associated Molecule

Previous studies have shown that a pool of the inhibitor-of-apoptosis (IAP) protein survivin [19] localizes to mitochondria and contributes to the stability of oxidative phosphorylation Complex II subunit succinate dehydrogenase B (SDHB) [20]. To further characterize this pathway, we carried out a proteomics screen for additional survivin-associated molecules in mitochondria, using prostate adenocarcinoma PC3 cells as a tumor model (S1 Methods). In this

screen, molecules associated with mitochondrial survivin comprised regulators of organelle trafficking (Rab11), assembly of respiratory chain complexes (PTCD1), oxidative stress (GPX4), mitoribosomal transferase activity (NSUN4), ubiquinone biosynthesis (COQ7), and the AAA+ peptidase subunit of the ClpXP complex, ClpP ([Fig 1A](#)).

Consistent with these results, survivin immune complexes precipitated from mitochondria of PC3 cells contained ClpP as well as TRAP-1 ([Fig 1B](#)) [[20](#)]. Reciprocally, ClpP co-immunoprecipitated with survivin and TRAP-1 in tumor mitochondria ([Fig 1C](#)). In addition, ClpX and ClpP mutually associated with each other as well as with SDHB in co-immunoprecipitation experiments ([Fig 1D](#)), consistent with the assembly of a survivin-ClpXP [[14](#)]-SDHB complex in tumor mitochondria. When analyzed for submitochondrial distribution, survivin, ClpP, and TRAP-1 co-localized within the organelle matrix in PC3 cells ([Fig 1E](#)). In addition, a fraction of TRAP-1 and survivin localized to the inner mitochondrial membrane ([Fig 1E](#)), in agreement with recent observations [[20](#)].

To begin investigating the role of a survivin-ClpXP complex in mitochondria, we next exposed PC3 cells to YM155, a small molecule survivin suppressant currently examined in the clinic as an anticancer drug. In these experiments, YM155 treatment was associated with reduced expression of ClpP ([Fig 1F](#)). As an independent approach, we next silenced survivin using our validated small interfering RNA (siRNA) sequences [[20](#)]. Survivin knockdown significantly reduced the levels of ClpP in mitochondria of PC3 cells, especially under conditions of hypoxic stress ([Fig 1G](#)). In contrast, YM155 treatment ([Fig 1F](#)) or siRNA silencing of survivin ([Fig 1G](#)) did not affect the expression of mitochondrial chaperones Hsp70 or Hsp60, or the voltage-dependent anion channel (VDAC). Next, we used cycloheximide block experiments to quantify changes in ClpXP stability after survivin targeting. In these experiments, YM155 treatment ([S1A and S1B Fig](#)) or siRNA silencing of survivin ([S1C and S1D Fig](#)) resulted in accelerated turnover of ClpP, compared to control siRNA transfectants. This regulation occurred at the protein level because survivin knockdown did not affect ClpP mRNA expression ([S1E Fig](#)). In reciprocal experiments, transfection of PC3 cells with a survivin variant engineered to selectively accumulate in mitochondria [[20](#)] increased ClpP levels in mitochondria ([Fig 1H](#)). In contrast, targeting survivin with YM155 ([Fig 1F](#)) or siRNA knockdown ([S1C and S1D Fig](#)) or, conversely, over-expression of mitochondrial survivin ([Fig 1H](#)) did not appreciably affect ClpX levels. This suggests that ClpP is the primary binding partner of survivin in the ClpXP complex, consistent with the results of the proteomics screen ([Fig 1A](#)).

ClpXP Regulation of Mitochondrial Complex II Folding and Activity

In mitochondria, survivin associates with the oxidative phosphorylation Complex II subunit, SDHB, and regulates its stability [[20](#)]. Therefore, a role of ClpXP in this process [[15](#)] was next investigated. First, siRNA silencing of ClpP resulted in increased accumulation of SDHB in mitochondria, whereas COX-IV levels were not affected ([S2A Fig](#)). We next looked at the folding status of SDHB in these conditions. We found that siRNA silencing of ClpP caused the accumulation of detergent-insoluble, i.e., misfolded, mitochondrial Complex II, whereas subunits of oxidative phosphorylation Complex I, III, IV, or V were not affected ([Fig 2A](#)). When individual Complex II subunits were examined, ClpP knockdown selectively induced misfolding and aggregation of SDHB at different detergent concentrations ([Figs 2B, 2C and S2B](#)). In contrast, ClpP depletion did not affect the solubility of SDHA or other mitochondrial proteins, including COX-IV ([Fig 2A and 2B](#)), VDAC, or citrate synthase (CS; [S2B Fig](#)), compared to control transfectants. Aggregation and misfolding of SDHB, but not SDHA, after ClpP knockdown was observed under different detergent conditions (NP-40; [S2C and S2D Fig](#)). In

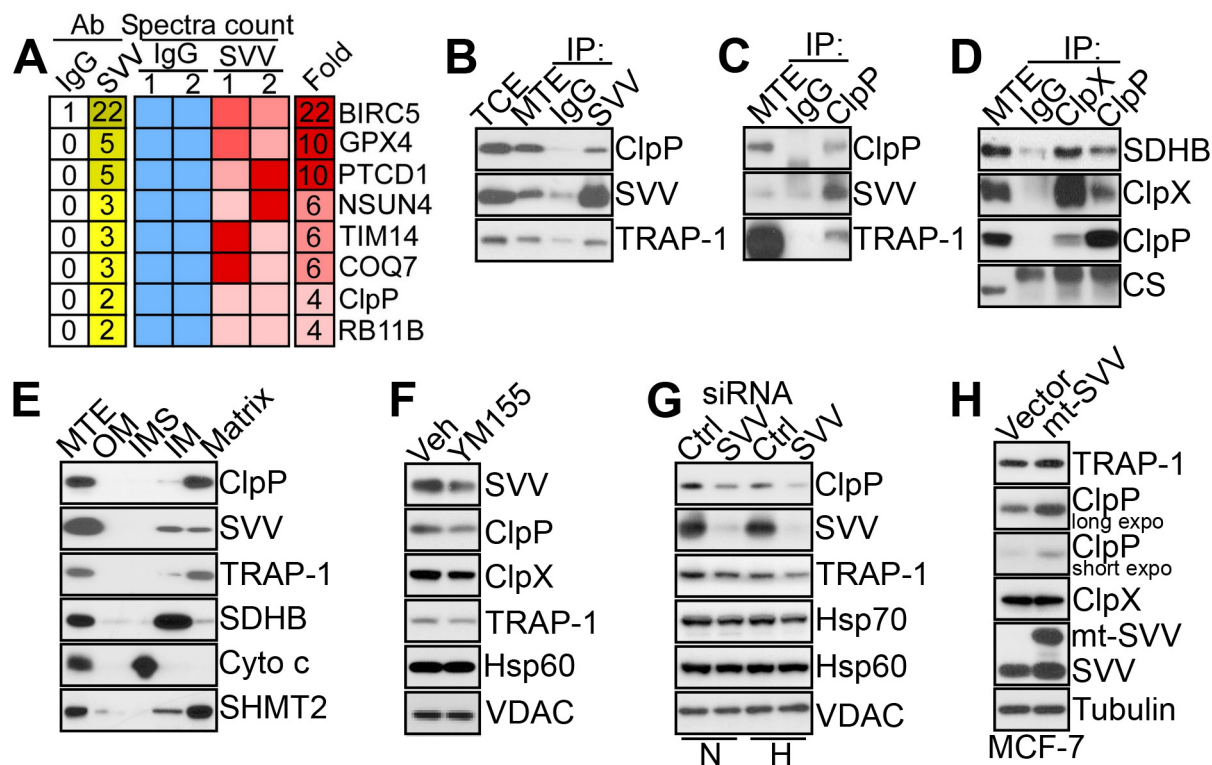


Fig 1. Survivin-ClpXP interaction. (A) Heatmap of proteomics identification of mitochondrial proteins co-precipitated with an antibody to survivin (SVV) or control IgG from PC3 mitochondrial extracts. Two independent replicates per condition are shown. A fold enrichment in spectra counts (SVV/IgG) is shown. (B–D) Mitochondrial extracts from PC3 cells were immunoprecipitated (IP) with antibodies to survivin (SVV) (B), ClpP (C), ClpP or ClpX (D), or non-binding IgG and analyzed by western blotting. TCE, total cell extracts. MTE, mitochondrial extracts. CS, citrate synthase. (E) Submitochondrial fractions representative of outer membrane (OM), inter-membrane space (IMS), inner membrane (IM), or matrix were isolated from PC3 cells and analyzed by western blotting. (F) PC3 cells were treated with vehicle (Veh) or small molecule survivin (SVV) suppressant YM155 and analyzed by western blotting. (G) PC3 cells in normoxia (N) or hypoxia (H) were transfected with control non-targeting siRNA (Ctrl) or survivin (SVV)-directed siRNA and analyzed by western blotting. (H) MCF-7 cells were transfected with vector or mitochondrial-targeted (mt) survivin (SVV) cDNA and analyzed by western blotting. Expo, exposure.

doi:10.1371/journal.pbio.1002507.g001

addition, siRNA silencing of ClpX similarly induced accumulation of aggregated or misfolded SDHB (Figs 2D and S2E).

ClpXP Is Required for Mitochondrial Respiration

Next, we asked whether SDHB misfolding induced by ClpXP targeting affected mitochondrial respiration. siRNA silencing of ClpX or ClpP did not affect mitochondrial Complex I activity in PC3 cells, compared to control siRNA transfectants (Fig 3A). In contrast, knockdown of ClpX or ClpP significantly reduced Complex II activity in PC3 cells (Fig 3B) as well as other prostate cancer cell types, including C4-2 (S3A Fig) and DU145 (S3B Fig). This response was specific because ClpX or ClpP targeting had no effect on mitochondrial Complex III (S3C Fig) or Complex IV (S3D Fig) activity, whereas Complex V function was increased in ClpP- but not ClpX-silenced PC3 cells (S3E Fig). Functionally, impaired Complex II activity after ClpXP targeting reduced oxygen consumption (Fig 3C), increased the NAD/NADH ratio (Figs 3D and S3F), and lowered overall ATP production (Fig 3E) in prostate cancer cells. Markers suggestive of compensatory glycolysis, including glucose consumption (S3G Fig) or lactate production (S3H Fig), were increased after ClpP- but not ClpX-silencing (S3G and S3H Fig). Consistent

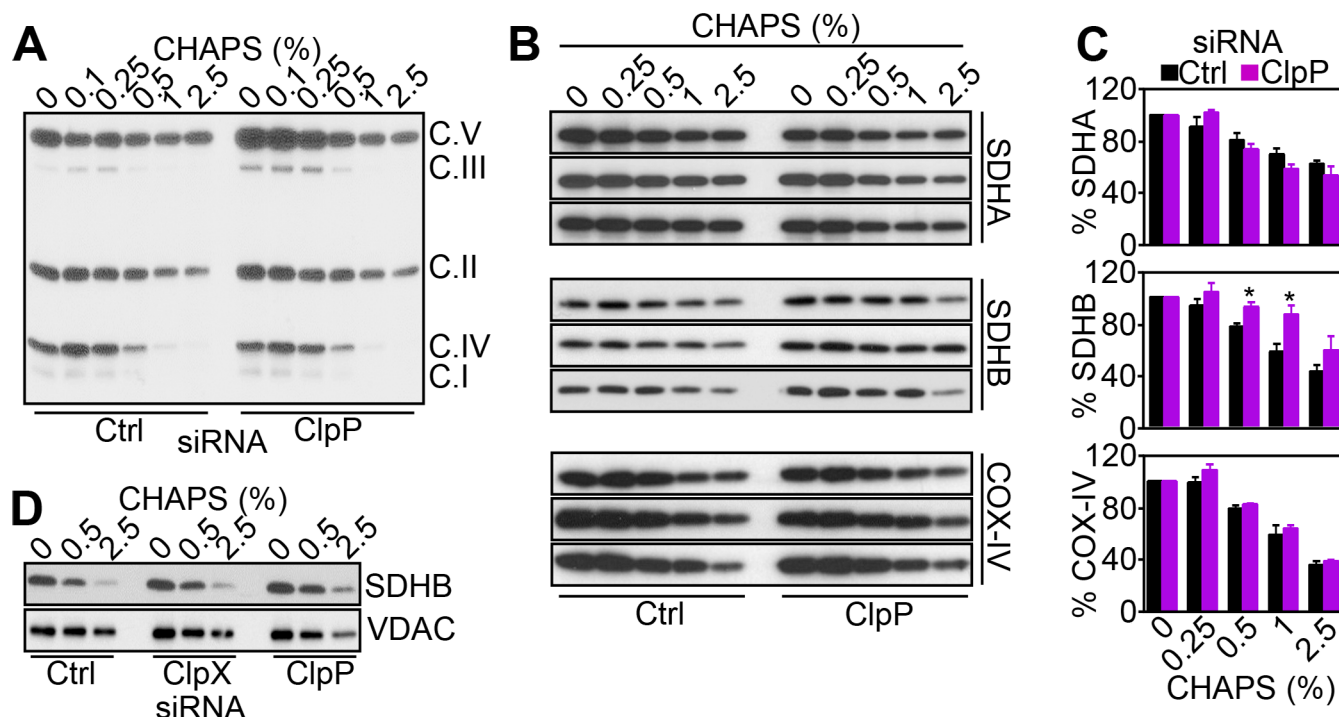


Fig 2. ClpXP regulates mitochondrial SDHB folding. (A) PC3 cells were transfected with control siRNA (Ctrl) or ClpP-directed siRNA and solubilized in the indicated concentrations of detergent (CHAPS), and insoluble fractions were analyzed by western blotting. The position of oxidative phosphorylation complex (C) subunits are indicated. (B) PC3 cells were transfected with control siRNA (Ctrl) or ClpP-directed siRNA and mixed with increasing concentrations of detergent (CHAPS), and insoluble fractions were analyzed by western blotting. Three independent experiments per condition are shown. (C) Densitometric quantification of protein bands in control or ClpP siRNA transfectants, as in (B). Data are the mean \pm SEM of four (SDHB) or three (SDHA, COX-IV) independent experiments. (D) PC3 cells transfected with control siRNA (Ctrl) or ClpP- or ClpX-directed siRNA were mixed with the indicated increasing concentrations of CHAPS, and insoluble material was analyzed by western blotting. Raw data for this figure can be found in [S1 Data](#).

doi:10.1371/journal.pbio.1002507.g002

with defective bioenergetics, PC3 cells silenced for ClpP or ClpX exhibited increased phosphorylation of the energy sensor 5' adenosine monophosphate-activated protein kinase (AMPK), whereas total AMPK levels were not affected (Fig 3F). In turn, AMPK phosphorylation coupled to downstream activation of autophagy, as determined by increased LC3-II conversion (Fig 3G), appearance of punctate LC3 staining by fluorescence microscopy (Fig 3H and 3I), accumulation of autophagy markers p62 and Beclin-1, and increased phosphorylation of ULK1 on its AMPK target site, Ser555 (Fig 3J).

Targeting Mitochondrial Proteases Induces Oxidative Stress

Based on these data, we next looked at the downstream consequences of defective mitochondrial respiration in ClpXP-targeted cells. siRNA silencing of ClpP or ClpX resulted in increased total cellular superoxide production in prostate cancer cells (Fig 4A–4C). This response was also associated with heightened production of mitochondria-specific reactive oxygen species (ROS), compared to control transfectants (Fig 4D). To rule out potential off-target effects, we next generated clones of PC3 and DU145 cells with stable shRNA knockdown of ClpP or ClpX (S4A Fig). Stable depletion of ClpXP did not affect total mitochondrial content (S4B Fig) or mitochondrial membrane potential (S4C Fig). In contrast, stable knockdown of ClpP increased mitochondrial ROS production (Fig 4E and 4F), with hyperoxidation of mitochondrial peroxiredoxin III (Prx III), a marker of oxidative damage (Fig 4G). Total Prx III levels were not

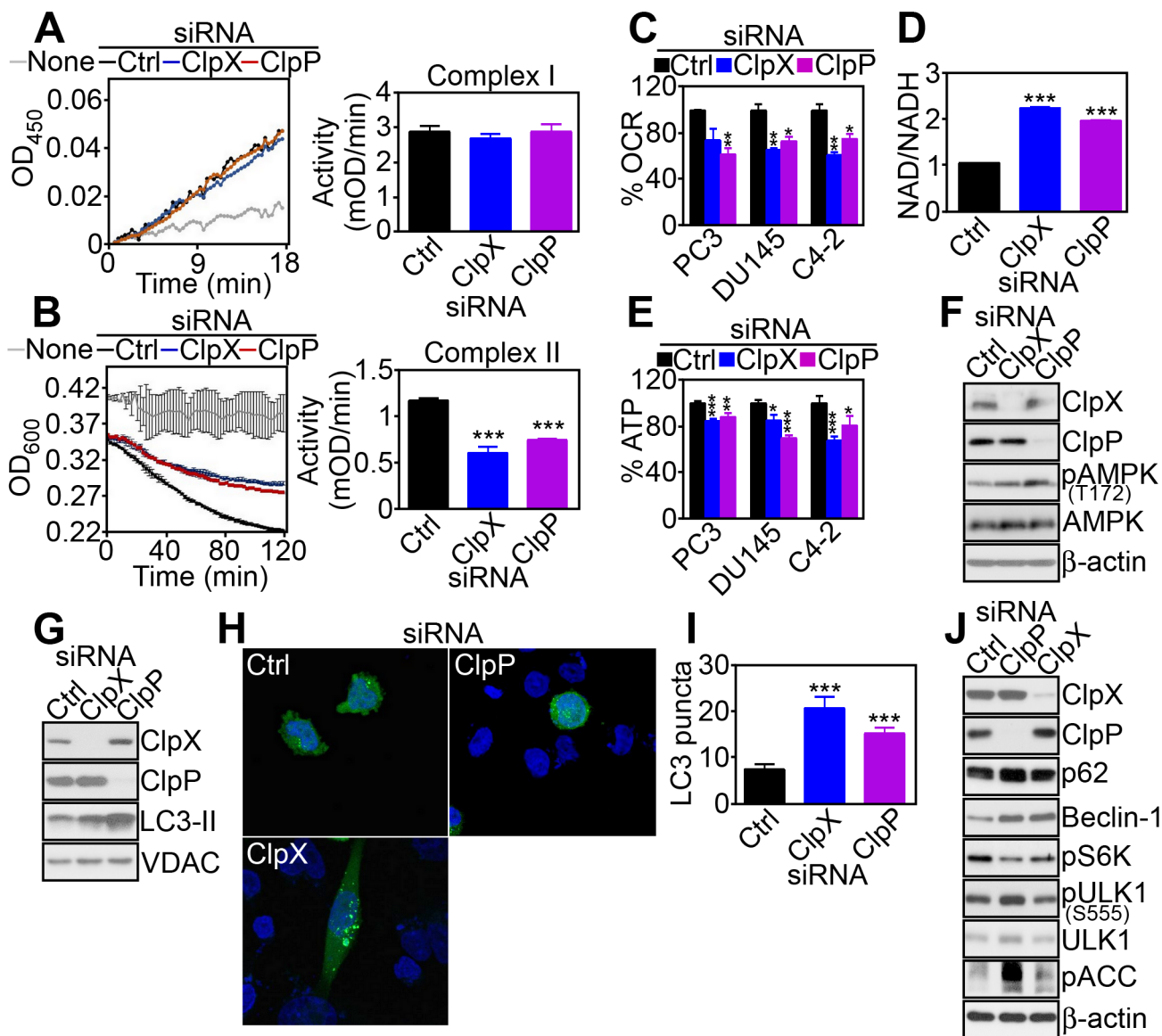


Fig 3. ClpXP regulation of mitochondrial bioenergetics. (A and B) PC3 cells were transfected with control siRNA (Ctrl), ClpX- or ClpP-directed siRNA, and mitochondrial extracts were analyzed for Complex I (A) or Complex II (B) activity. *Right*, Quantification of citrate synthase-normalized mitochondrial complex activity. ***, $p < 0.0001$. (C–E) The indicated prostate cancer cell types were transfected with control siRNA (Ctrl), ClpX- or ClpP-directed siRNA, and analyzed for changes in oxygen consumption rate (OCR, C), NAD/NADH ratio (PC3 cells, D), or ATP production (E). **, $p < 0.006$; ***, $p < 0.0001$. (F and G) PC3 cells transfected with the indicated siRNAs were analyzed by western blotting. (H and I) siRNA-silenced PC3 cells and transfected with GFP-LC3 were analyzed by fluorescence microscopy (H) and the number of LC3 puncta per cell were quantified (I). ***, $p < 0.0001$. (J) PC3 cells were transfected with control siRNA (Ctrl), ClpX- or ClpP-directed siRNA, and analyzed by western blotting. Raw data for this figure can be found in [S2 Data](#).

doi:10.1371/journal.pbio.1002507.g003

affected (Fig 4G). In contrast, stable shRNA silencing of ClpX did not significantly modulate mitochondrial ROS production (Fig 4E and 4F) or Prx III hyperoxidation (Fig 4G), suggesting that other mechanisms compensated for ClpX loss in the stable cell line. Treatment with the antioxidant N-acetylcysteine (NAC) or mitochondrial ROS scavenger MitoTempo alone did not rescue Prx III hyperoxidation after ClpXP knockdown (S4D Fig). Conversely, the combination of NAC plus MitoTempo reversed the hyperoxidation of Prx III in these cells (S4D Fig). Functionally, we next asked if oxidative stress induced by ClpXP targeting was important for

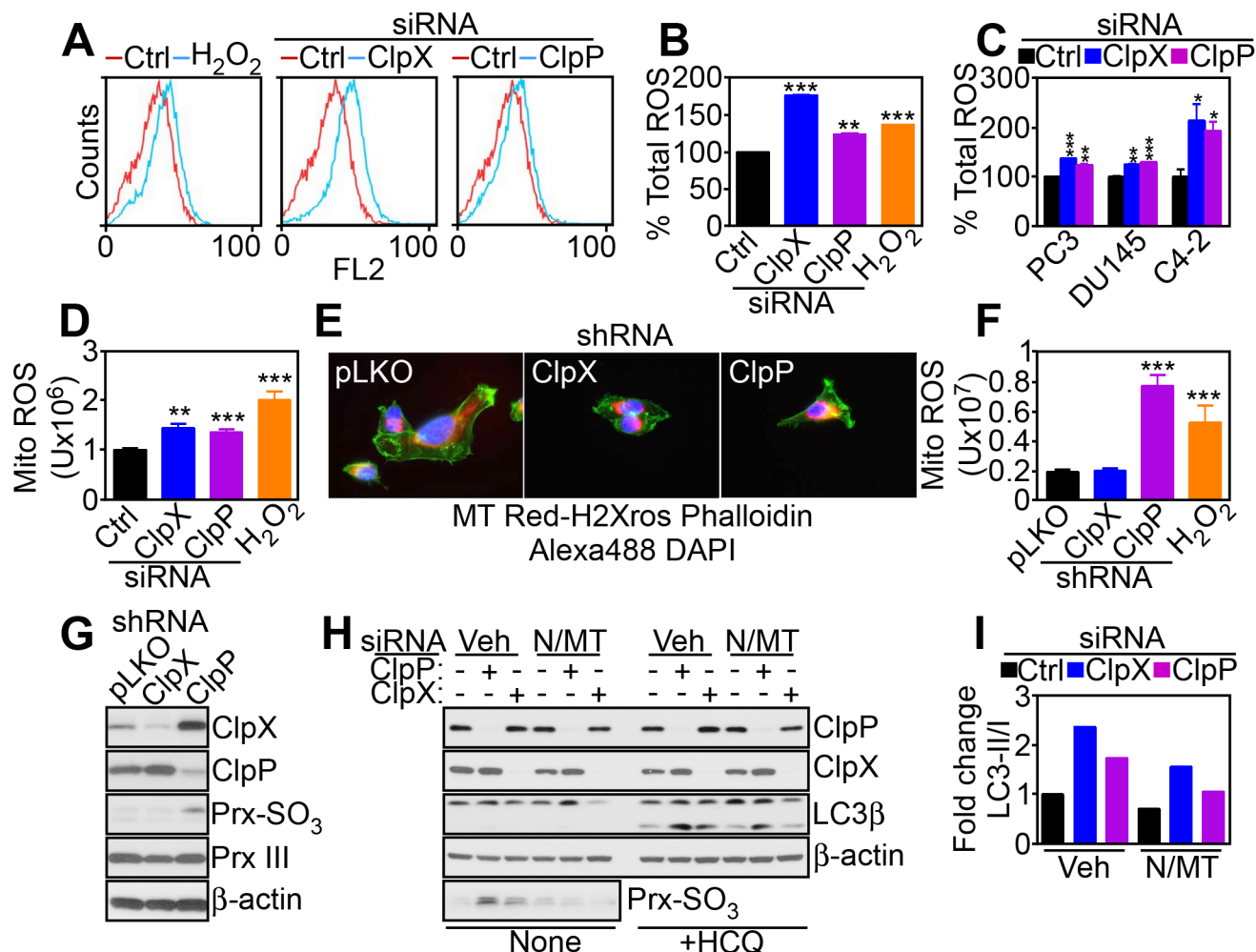


Fig 4. Mitochondrial ROS modulation by ClpXP. (A and B) PC3 cells transfected with control siRNA (Ctrl) or ClpX- or ClpP-directed siRNA were labeled with CellROX Green Reagent by flow cytometry (A), and staining intensity was quantified (B). H₂O₂ was a control oxidative stimulus. **, $p = 0.004$; ***, $p < 0.0001$. (C) The indicated prostate cancer cell types were analyzed for total ROS production as in (A). *, $p = 0.03–0.04$; **, $p = 0.001$; ***, $p = 0.0008–<0.0001$. (D) PC3 cells transfected with the indicated siRNAs as in (A) were analyzed for MitoSOX red mitochondrial superoxide reactivity by fluorescence microscopy and quantified. H₂O₂ was a control oxidative stimulus. **, $p = 0.001$; ***, $p = 0.0004–0.0001$. (E and F) PC3 cells stably transduced with control pLKO or shRNA to ClpX or ClpP were analyzed for mitochondrial superoxide production by fluorescence microscopy (E), and staining intensity was quantified (F). ***, $p = 0.0004–0.0001$. (G) PC3 cells stably transduced with pLKO or ClpX- or ClpP-directed shRNA were analyzed by western blotting. (H) PC3 cells transfected with control siRNA or ClpX- or ClpP-directed siRNA were incubated with vehicle (Veh) or the combination of antioxidants NAC (N) plus mitochondrial-directed MitoTempo (MT) and analyzed by western blotting in the absence or presence of the autophagic flux inhibitor hydroxychloroquine (HCQ). (I) Densitometric quantification of LC3-II/I ratio in vehicle (Veh) or antioxidant-treated PC3 cells in (H). Raw data for this figure can be found in [S3 Data](#).

doi:10.1371/journal.pbio.1002507.g004

autophagy induction in these settings. Consistent with this possibility, the combination of NAC plus MitoTempo significantly attenuated LC3-II conversion in ClpP- or ClpX-silenced cells (Fig 4H and 4I), and this response was amplified by the autophagic flux inhibitor hydroxychloroquine (Fig 4H).

ClpXP Overexpression in Human Cancer

To complement the results obtained with tumor cell lines, we next looked at a potential differential expression of ClpXP in human cancer. First, ClpP was prominently upregulated in breast

adenocarcinoma MCF-7 cells, compared to non-tumorigenic breast epithelial MCF-10A cells (Fig 5A). Similarly, ClpP was highly expressed in primary tissue samples of human prostatic adenocarcinoma, but not normal prostate epithelium (Fig 5B). For comparison, another protease involved in mitochondrial protein quality control, LonP1, was expressed in normal prostate but not prostate cancer (Fig 5B). When applied to tissue extracts of patient-derived tumor samples, an antibody to ClpP reacted with a predominant single band by western blotting (S5A Fig), reinforcing its specificity. Immunohistochemical staining of a universal cancer tissue microarray demonstrated that ClpP was overexpressed in virtually every human malignancy examined (Fig 5C), with intense cytoplasmic staining in the tumor cell population (Figs 5D and 5B). ClpP expression in cancer patients was independent of grade (colon adenocarcinoma and CNS tumors), Gleason score (prostate adenocarcinoma), histotype (lung cancer), or aggressive versus indolent lymphomas (S5C Fig). Conversely, ClpP levels were increased in histotypes of breast adenocarcinoma compared to normal epithelium (S5C Fig). In addition, ClpP became more prominently expressed in metastatic non-small cell lung cancer (NSCLC), compared to non-metastatic lesions, with the highest levels in brain-metastatic NSCLC (Figs 5E, 5F and 5D). In contrast, no difference in the percentage of ClpP-positive cells was observed in primary or metastatic NSCLC (Fig 5G). Consistent with these results, bioinformatics meta-analysis of public databases (Prognoscan) revealed that ClpP expression correlated with poorer outcome in 9 out of 14 analyzed datasets (64%; S2 Table and Fig 5H–5J), whereas ClpP levels were associated with better prognosis (S2 Table) in only one dataset (Melbourne). Importantly, high levels of ClpP expression were associated with shortened distant metastasis-free survival (S2 Table) in patients with breast adenocarcinoma (Fig 5H) and uveal melanoma (Fig 5I) and in abbreviated relapse-free survival in lung adenocarcinoma (Fig 5J).

Regulation of Tumor Cell Proliferation by ClpXP

Based on these results, we next asked how ClpXP influenced tumor progression. In a first series of experiments, knockdown of ClpP or ClpX partially reduced tumor cell proliferation (Figs 6A and 6A) and inhibited colony formation (Figs 6B, 6C and 6B), a marker of tumorigenicity. The effect of ClpXP silencing on tumor cell proliferation was cell-type-specific and more pronounced after knockdown of ClpP compared to ClpX (S6A Fig). In addition, silencing of ClpP or ClpX minimally reduced proliferation of non-metastatic breast adenocarcinoma MCF-7 cells, and non-tumorigenic breast epithelial MCF-10A cells were not affected (S6A Fig). When characterized in sensitive PC3 cells, knockdown of ClpXP resulted in lower levels of cyclins A, B1, and D1 (Fig 6D), reduced number of BrdU-positive cells (S6C Fig), and accumulation of cells with G1 DNA content (S6D Fig), consistent with cell cycle arrest.

Next, we looked at the mechanism(s) of ClpXP regulation of tumor cell proliferation. First, silencing of ClpP or ClpX in MCF-7 cells had little to no effect on mitochondrial Complex II activity (S6E Fig) and oxygen consumption rate (OCR, S6F Fig), thus mirroring the marginal sensitivity of these cells to ClpXP targeting (S6A Fig). In addition, ClpP or ClpXP knockdown did not reduce Complex II activity (S6G Fig) or OCR (S6H Fig) in non-tumorigenic MCF-10A cells, further linking impaired mitochondrial respiration induced by ClpXP targeting to reduced tumor cell proliferation. Based on these results, we next asked if aberrant ROS production associated with ClpXP targeting interfered with tumor cell proliferation. Consistent with this possibility, the combination of antioxidants NAC plus MitoTempo (MT) restored tumor cell proliferation (Fig 6E) and colony formation (Fig 6F) in ClpP-silenced PC3 cells. Similarly, transfection of the ROS scavenger MnSOD rescued the defect of cell proliferation induced by ClpP knockdown (Fig 6G). Finally, ClpXP depletion further sensitized tumor cells to “stress stimuli,” with more sustained inhibition of tumor cell proliferation mediated by oxidative stress

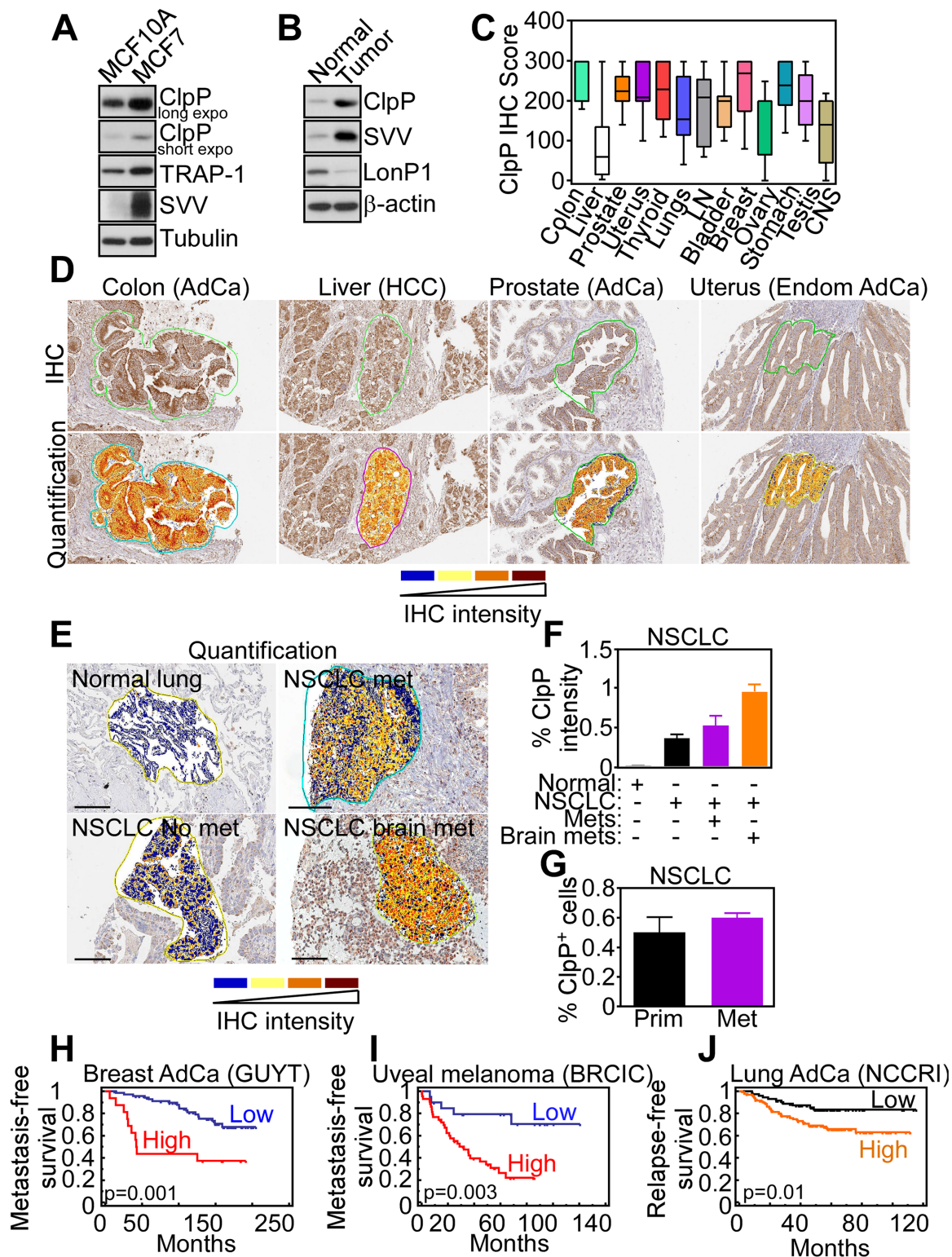


Fig 5. ClpP expression in human cancer. (A and B) Breast adenocarcinoma MCF-7 cells, non-tumorigenic breast epithelial MCF-10A cells (A), or primary human tissue samples representative of normal prostate or prostatic adenocarcinoma (B) were analyzed by western blotting. (C) Immunohistochemistry (IHC) score of ClpP expression in the indicated primary human tumors arrayed in a universal cancer tissue microarray. LN, lymph nodes; CNS, central nervous system. (D) IHC staining and Apero quantification of ClpP expression in the indicated human tumor types. AdCa, adenocarcinoma; HCC, hepatocellular

carcinoma; Endom, endometrial AdCa. (E) Aperio quantification of ClpP IHC expression in primary tissue samples of non-small cell lung cancer (NSCLC) that developed (met) or did not develop (no met) distant metastases or brain metastases (brain met) during a 5-y follow-up. (F) Quantification of ClpP staining intensity in the NSCLC cases in (E). (G) Quantification of ClpP-positive cells in primary and brain metastatic NSCLC. (H–J) Kaplan-Meier curves of metastasis-free survival (H and I) or relapse-free survival (J) in the indicated patient series with high or low expression of ClpP. AdCa, adenocarcinoma. Raw data for this figure can be found in [S4 Data](#).

doi:10.1371/journal.pbio.1002507.g005

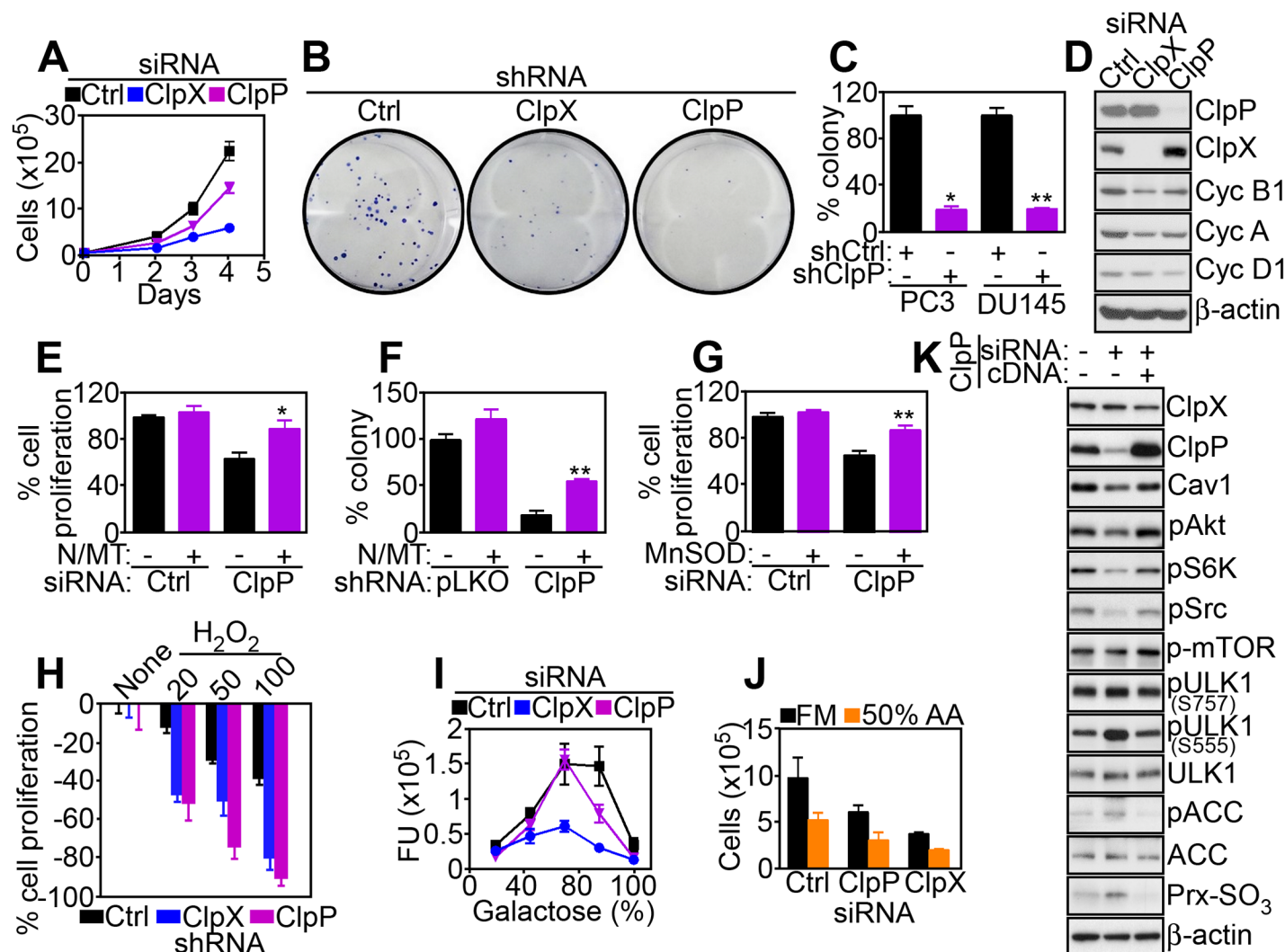


Fig 6. ClpXP regulation of tumor cell proliferation. (A) PC3 cells were transfected with control siRNA (Ctrl) or ClpX- or ClpP-directed siRNA and analyzed for cell proliferation at the indicated time intervals by direct cell counting. (B and C) PC3 or DU145 cells stably transduced with pLKO or ClpX- or ClpP-directed shRNA were analyzed for colony formation by crystal violet staining after 7 d (B, PC3) and quantified (C). *, $p = 0.01$; **, $p = 0.006$. (D) PC3 cells transfected with the indicated siRNAs as in (A) were analyzed by western blotting. (E and F) PC3 cells transfected with the indicated siRNAs (E) or shRNAs (F) were incubated with the combination of antioxidants NAC (N) plus mitochondrial-directed MitoTempo (MT) and analyzed for cell proliferation by direct cell counting (E) or colony formation (F). *, $p = 0.028$; **, $p = 0.0026$. (G) PC3 cells treated with control siRNA (Ctrl) or ClpP-directed siRNA were transfected with vector or MnSOD cDNA, and analyzed for cell proliferation by direct cell counting. **, $p = 0.001$. (H) PC3 cells stably transduced with pLKO or ClpX- or ClpP-directed shRNA were incubated with the indicated increasing concentrations of H₂O₂ (mM) and analyzed for inhibition of cell proliferation by direct cell counting. (I and J) PC3 cells transfected with the indicated siRNAs were incubated with increasing galactose:glucose ratios (I) or amino acid-deprived medium (50% amino acids, J) and analyzed for cell proliferation by direct cell counting. FU, fluorescence units. (K) PC3 cells transfected with ClpP-directed siRNA were reconstituted with ClpP cDNA and analyzed by western blotting. Raw data for this figure can be found in [S5 Data](#).

doi:10.1371/journal.pbio.1002507.g006

(H₂O₂, [Fig 6H](#)), high galactose:glucose ratios ([Fig 6I](#)), or amino acid deprivation (50% amino acids, [Fig 6J](#)). We next reconstituted ClpP-silenced PC3 cells with siRNA-insensitive ClpP cDNA to test the specificity of these findings. Re-expression of ClpP under these conditions rescued the phosphorylation of Akt, Src, and p70S6K in ClpP-silenced cells ([Fig 6K](#)). In addition, re-expression of ClpP reversed the induction of autophagy (S555 phosphorylation of ULK1), AMPK signaling (ACC phosphorylation), and oxidative stress (Prx III hyperoxidation) induced by ClpP silencing ([Fig 6K](#)).

ClpXP Regulation of Tumor Cell Invasion and Metastasis

A potential participation of ClpXP in other tumor traits was investigated next, and we focused on cell motility, which requires mitochondrial bioenergetics [20]. siRNA knockdown of ClpP or ClpX inhibited directional PC3 cell migration in a wound closure assay ([Fig 7A and 7B](#)), and suppressed tumor cell invasion across Matrigel-coated Transwell inserts ([Figs 7C and 7A](#)). This response was specific because reconstitution of ClpP-silenced cells with a ClpP cDNA restored tumor cell motility in a wound closure assay ([Fig 7D](#)). Mechanistically, the combination of antioxidants NAC plus MitoTempo rescued the defect of tumor cell invasion mediated by ClpP knockdown ([Fig 7E](#)), demonstrating that increased ROS production in these settings was responsible for the inhibition of cell motility.

Next, we mapped the signaling requirements of ClpXP regulation of tumor cell motility. In these experiments, siRNA silencing of ClpP attenuated Akt (S473) phosphorylation ([S7B Fig](#)) and lowered the expression of cell motility effectors Caveolin-1 (Cav1) and Axl ([S7B Fig](#)). ClpXP knockdown was marginally effective ([S7B Fig](#)), and no changes in Cav1 mRNA levels were observed in control or ClpP siRNA transfectants ([Fig 7F](#)). Exposure of tumor cells to the oxidative stressor H₂O₂ mimicked this response, causing hyperoxidation of Prx III and loss of Cav1 expression ([S7C Fig](#)). Accordingly, siRNA silencing of Cav1 in PC3 cells was sufficient to reduce the levels of phosphorylated Akt (S473) ([S7D Fig](#)) and suppressed tumor cell migration and invasion, compared to control transfectants ([S7E Fig](#)). To validate a role of Cav1 in this cell motility pathway, we next reconstituted ClpP- or ClpX-depleted cells with a Cav1 cDNA. Re-expression of Cav1 in these settings restored Akt phosphorylation ([Fig 7G](#)) and rescued the defect of tumor cell invasion ([Fig 7H](#)) after ClpP, but not ClpX knockdown. In contrast, reconstitution of ClpXP-targeted cells with an Akt cDNA had no effect ([S7F Fig](#)).

Finally, we asked if ClpXP regulation of tumor cell motility was important for metastasis in vivo. Intra-splenic injection of PC3 cells transfected with control shRNA gave rise to extensive metastatic dissemination to the liver of immunocompromised mice within 11 d of injection ([Fig 7I and 7J](#)). In contrast, stable silencing of ClpX or ClpP in these cells suppressed the size, number, and extent of liver metastases at the same time interval ([Fig 7I and 7J](#)).

Discussion

In this study, we have shown that the unfoldase-peptidase ClpXP forms a complex with survivin and the Hsp90-like chaperone TRAP-1 in mitochondria of tumor cells. This interaction maintains protein quality control and function of the oxidative phosphorylation Complex II subunit SDHB. Accordingly, genetic targeting of ClpXP causes the accumulation of misfolded SDHB, resulting in impaired bioenergetics, oxidative damage, and activation of stress signals, including autophagy. ClpXP is dramatically upregulated in primary and disseminated human tumors, correlates with shortened patient survival, and mechanistically supports tumor cell proliferation, cell motility, and heightened metastatic competence in vivo.

Extensively studied in bacteria [21] and proposed as a regulator of cell persistence [22], the ClpXP multimolecular complex [23] comprises a ClpX subunit that functions as an ATPase-

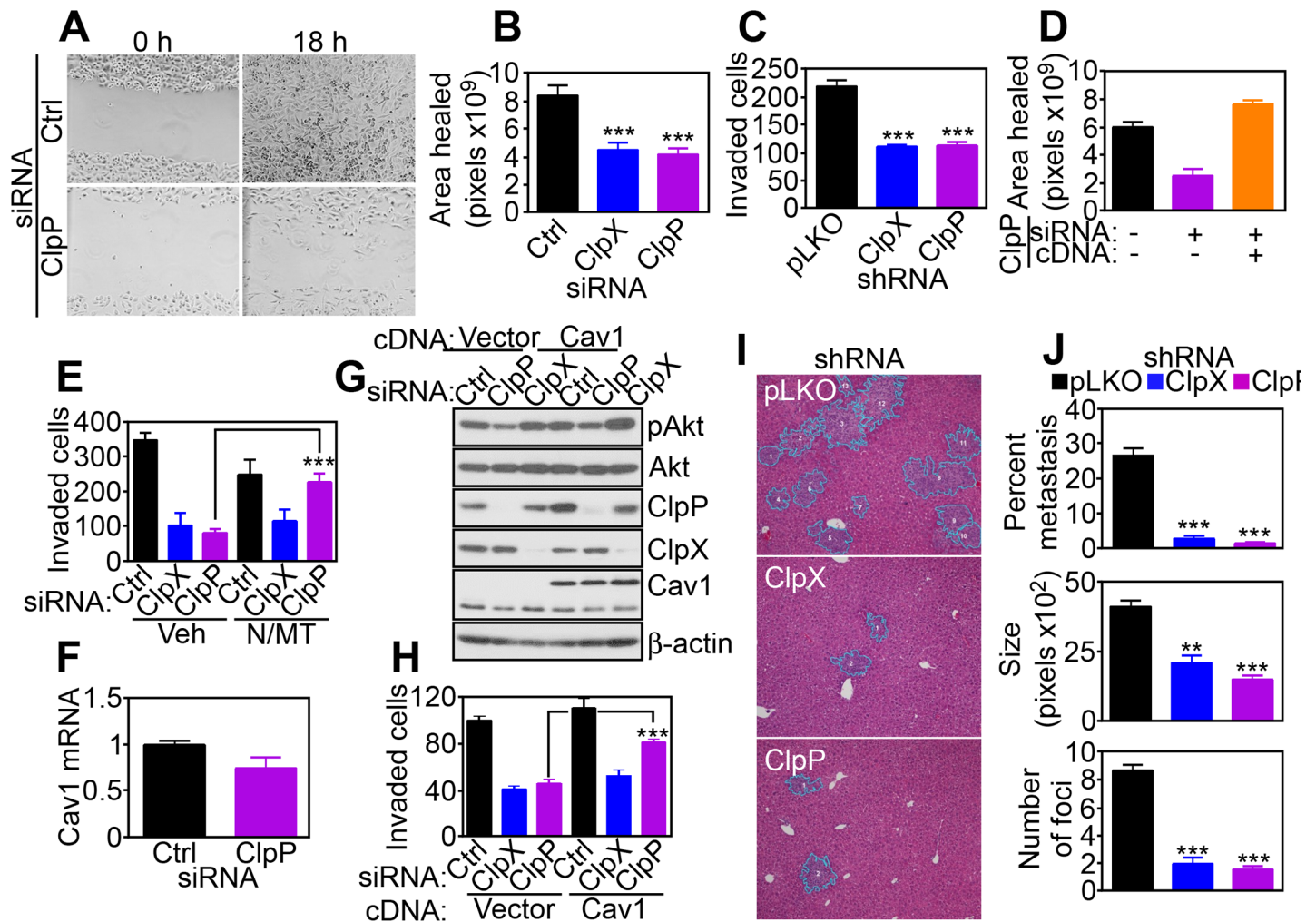


Fig 7. Requirement of ClpXP for tumor cell invasion and metastasis. (A and B) PC3 cells transfected with control siRNA (Ctrl) or ClpX- or ClpP-directed siRNA were analyzed for directional cell migration in a wound closure assay by light microscopy (ClpP, A), and wound surface area was quantified after 18 h (B). ***, $p < 0.0001$. (C) PC3 cells stably transduced with pLKO or ClpX- or ClpP-directed shRNA were analyzed for cell invasion across Matrigel-coated inserts. ***, $p < 0.0001$. (D) PC3 cells transfected with ClpP-directed siRNA were reconstituted with ClpP cDNA and analyzed for cell migration in a wound closure assay as in (A and B). (E) PC3 cells transfected with control siRNA (Ctrl) or ClpX- or ClpP-directed siRNA were analyzed for Matrigel invasion in the presence of vehicle (Veh) or the combination of antioxidants NAC (N) plus MitoTempo (MT). ***, $p < 0.0001$. (F) PC3 cells transfected with control siRNA (Ctrl) or ClpP-directed siRNA were analyzed for Caveolin-1 (Cav1) mRNA levels by quantitative PCR. (G and H) PC3 cells were transfected with the indicated siRNAs, reconstituted with vector or Cav1 cDNA, and analyzed by western blotting (G) or Matrigel invasion (H). ***, $p < 0.0001$. (I) PC3 cells stably transduced with pLKO or ClpX- or ClpP-directed shRNA were injected in the spleen of immunocompromised mice and livers collected after 11 d, which were analyzed by hematoxylin-eosin staining and light microscopy. (J) Quantification of metastatic burden (% metastasis, top), number of metastatic foci (middle), and size of metastatic foci (bottom) in mice intrasplenically injected with shRNA-transduced PC3 cells as in (I). **, $p = 0.002$; ***, $p < 0.0001$. Raw data for this figure can be found in [S6 Data](#).

doi:10.1371/journal.pbio.1002507.g007

directed unfoldase for unstructured protein substrates and an internal caseinolytic peptidase, ClpP, which degrades the translocated, unfolded peptides [14]. Although this proteasome-like arrangement is conserved in mammalian cells [15], the data presented here suggest that the ClpP and ClpX subunits may not have completely overlapping function(s) in tumor mitochondria, especially with respect to Akt activation and Cav1-dependent tumor cell motility. It is possible that these different responses reflect individual mitochondrial proteins independently regulated by ClpP or ClpX, or, alternatively, the coupling of individual ClpXP subunits to separate regulators of downstream signaling.

The interaction between TRAP-1 [10] and ClpXP [14] described here brings together the two main mechanisms of proteostasis: chaperone-regulated protein folding (TRAP-1) and proteolytic removal of misfolded molecules (ClpXP) in a single, functional continuum. A mitochondrial pool of survivin contributes to this proteostasis network, potentially as a scaffolding protein that binds both ClpP (this study) and TRAP-1 [20], and contributes to the stability of the complex. Consistent with the earlier elucidation of a TRAP-1 proteome in tumor mitochondria [10], a key substrate of the proteostasis network identified here was the iron-sulfur SDHB subunit of oxidative phosphorylation Complex II. The biochemical requirements of mitochondrial respiration and electron transport chain are well understood [24], but the possibility that these activities may depend on a carefully orchestrated balance of protein folding/protein clearance, especially in the proteotoxic-prone environment of tumor mitochondria [5], has not been widely considered. Consistent with this possibility, perturbation of the mitochondrial proteostasis network by TRAP-1 targeting [10] or ClpXP knockdown (this study) caused SDHB degradation or, conversely, accumulation of misfolded or aggregated SDHB. The exquisite specificity of this response, in which none of the other oxidative phosphorylation complexes are affected, highlights a potential unique propensity of SDHB to protein misfolding, especially in tumor mitochondria, or, alternatively, a more stringent requirement of protein quality control to enable efficient Complex II activity.

Irrespective, the loss of SDHB due to defective proteostasis profoundly affected mitochondrial bioenergetics, with decreased oxygen consumption, loss of ATP production, and a phenotype of cellular “stress,” characterized by activation of a mitochondrial and ER UPR [11], AMPK phosphorylation [25], stimulation of autophagy [12], and loss of mechanistic target of rapamycin (mTOR) signaling [20]. As shown here, an important mediator of these responses was the increased production of mitochondrial ROS and the ensuing oxidative damage likely associated with a defective electron transport chain [24]. This model is consistent with other data in the literature that homozygous deletion of TRAP-1 caused increased ROS production, DNA damage, and reduced cell proliferation [26], whereas TRAP-1 overexpression is protective against oxidative stress [27,28]. Here, antioxidants that include a mitochondrial ROS scavenger, MitoTempo, prevented the activation of autophagy and rescued the defects of cell proliferation and tumor cell invasion associated with ClpXP targeting, establishing a causal role of mitochondrial oxidative stress in these tumor traits.

Although a role of TRAP-1 in tumor progression is recognized [29], the possibility that ClpXP-directed proteostasis [14] may be also exploited in cancer has been proposed only recently [30]. In that study, the ClpXP subunit ClpP was found overexpressed in a subset of human acute myeloid leukemias, and pharmacologic or genetic targeting of ClpP impaired mitochondrial oxidative phosphorylation, resulting in leukemia cell killing [30]. The data presented here extend these observations and demonstrate that ClpXP-directed proteostasis is exploited in most human cancers, correlating with shortened patient survival. Where the two studies diverge, however, is in the mechanistic underpinning of the proposed pathway. Here, ClpXP was recognized as a pivotal component of a proteostasis network that, together with TRAP-1 [10] and survivin [20], ensures mitochondrial homeostasis in tumors. In our hands, and at variance with recent findings [30], targeting ClpXP only partially reduced tumor cell proliferation and in a cell-type-specific manner, with no measurable effect on tumor cell viability. Instead, we found that ClpXP was required to support directional tumor cell migration, invasion, and heightened metastatic dissemination *in vivo*. Mechanistically, this pathway involved increased phosphorylation of key cell motility kinases Akt and Src, and reconstitution experiments in ClpP-silenced cells identified the membrane microdomain adapter caveolin-1 [31] as a novel, oxidative, stress-regulated mediator of tumor cell motility.

As most epithelial tumors rewire their metabolism toward glycolysis [32], a role of mitochondrial bioenergetics in cancer has been controversial, and SDHB itself has been at times dubbed as a “tumor suppressor.” On the other hand, oxidative phosphorylation remains an important energy source in most cancers [33], fueling critical disease traits such as tumor repopulation after oncogene ablation [34] and drug resistance [35]. The data presented here reinforce this model and establish a key requirement of mitochondrial integrity for tumor cell motility and metastatic competence in vivo. This conclusion fits well with other evidence that oxidative phosphorylation is required for membrane lamellipodia dynamics, turnover of focal adhesion complexes, and phosphorylation of cell motility kinases [20,36], supporting tumor cell invasion and metastatic dissemination, in vivo [25,37]. In the context of a proteostasis network, ClpXP may contribute to this response by efficiently removing misfolded or aggregated SDHB molecules to preserve Complex II bioenergetics as well as buffering organelle oxidative stress.

In summary, we have shown that the unfoldase-peptidase complex ClpXP [14] is universally exploited in human cancer and contributes to a mitochondrial proteostasis network that controls metabolic reprogramming and downstream signals of tumor cell proliferation, motility, and metastatic competence in vivo. There is now considerable interest in targeting unique features of tumor metabolism, including mitochondrial functions [38], as a novel approach to cancer therapy. In this context, proof-of-concept studies have demonstrated that small molecule targeting of mitochondrial Hsp90s [25] or ClpXP [30] is feasible and produces potent anti-cancer activity in preclinical models. Together, this suggests that therapeutic inhibition of the mitochondrial proteostasis network described here may provide a viable strategy to disrupt key requirements of tumor progression.

Materials and Methods

Patient Samples

All patient-related studies were reviewed and approved by an institutional review board at Fondazione IRCCS Ca' Granda Ospedale Maggiore Policlinico Milan, Italy. A cohort of 53 patients with single brain metastases who underwent surgical resection for curative purposes between 2010 and 2015 was retrieved from the archives of Fondazione IRCCS Ca' Granda Ospedale Maggiore Policlinico (Milan, Italy) and arranged in a tissue microarray (TMA), as described [39]. The predominant primary cancer histotype of metastatic cases was non-small cell lung cancer (NSCLC, $n = 44$). Nineteen NSCLC patients for which complete 5-y follow-up records were available were included in the study. During follow-up, 9 NSCLC patients developed metastatic disease to the brain, whereas 10 patients had no evidence of metastasis (S1 Table). A Cancer Universal TMA (CaU-TMA) representative of 13 different cancer types (10 cases for each tumor type) was described previously [40].

Mitochondrial Protein Folding

Mitochondrial protein folding assays were performed as previously described [10]. Briefly, mitochondrial fractions were isolated from PC3 cells transfected with control non-targeting siRNA or ClpP- or ClpX-directed siRNA after 72 h and suspended in equal volume of mitochondrial fractionation buffer containing increasing concentrations of NP-40 (0%, 0.05%, 0.1%, 0.2%, 0.5%, or 2%) or CHAPS (0%, 0.1%, 0.25%, 0.5%, 1%, or 2.5%). Samples were incubated for 25 min on ice with vortexing every 5 min, and detergent-insoluble protein aggregates were isolated by centrifugation at 20,000 g for 20 min, separated on SDS polyacrylamide gels, and analyzed by western blotting.

Analysis of Bioenergetics

The various prostate cancer cell types were transfected with control non-targeting siRNA or ClpP- or ClpX-directed siRNA for 48 h or 72 h and analyzed for ATP generation (BioChain cat No. Z5030041) or oxygen consumption (ENZO Lifesciences cat. No. ENZ-51045-1), as described previously [10]. In other experiments, fresh culture medium containing dialyzed FBS was harvested after 2 h and examined for lactate production (Abcam cat No. ab65331). The quantification of NAD⁺ or NADH was measured by enzymatic NADH recycling assay according to the manufacturer's instruction (BioVision Cat No. K337-100). Briefly, PC3 cells (6 x 10⁵) transfected with control non-targeting siRNA or ClpP- or ClpX-directed siRNA were harvested after 72 h, and cell pellets were disrupted by two cycles of freezing and thawing in NADH/NAD⁺ extraction buffer. Soluble fractions were collected by centrifugation at 20,000 g for 5 min and processed for removal of NADH-consuming enzymes using YM-10 (Millipore). For assessment of NADH content, the cycling assay was performed after decomposition of NAD⁺ by heating at 60°C for 25 min, whereas the decomposition step was omitted for determination of total NAD⁺/H content.

Mitochondrial Oxidative Phosphorylation Complex Activity

Various prostate cancer cell types were analyzed for changes in oxidative phosphorylation complex activity using Abcam reagents (Cat. no. ab109721—Complex I, ab109908—Complex II, ab109905—Complex II/III, ab109909—Complex IV) and Cayman reagent (701000—Complex V) using isolated lysed mitochondria, as described [10]. Briefly, tumor cells were transfected with control non-targeting siRNA or ClpP- or ClpX-directed siRNA and validated for protein knockdown by western blotting, and 2 µg of mitochondrial extracts from each condition were assayed for citrate synthase (CS) activity (ScienCell). Aliquots of mitochondrial lysates with comparable CS activity were applied for determination of the individual mitochondrial complex function. Relative complex activities were calculated by determining the change in absorbance over time in the linear range of the individual measurements.

ROS Analysis

To detect total ROS, ClpP- or ClpX-silenced prostate cancer cell types were incubated with 2.5 µM of CellROX Green Reagent (Invitrogen) for 30 min at 37°C, according to the manufacturer's instructions. After three washes in PBS, pH 7.4, cells were harvested and analyzed on a FACS Calibur flow cytometer, with the CellROX Green Reagent signal in FL1. Intact cells were gated in the FSC/SSC plot to exclude small debris. The resulting FL1 data were plotted on a histogram. Superoxide production by mitochondria was visualized by fluorescence microscopy, as described previously [36]. Briefly, 1.5 x 10⁴ cells were grown on high optical quality 8-well µ-slides (Ibidi) and stained with MitoSOX Red mitochondrial superoxide indicator (5 µM, 10 min) in complete medium, followed by extensive washing in warm complete medium. Stained cells were imaged with a 40X objective on a Nikon TE300 inverted time-lapse microscope equipped with a video system containing an Evolution QEi camera and a time-lapse video cassette recorder. The atmosphere was equilibrated to 37°C and 5% CO₂ in an incubation chamber. Phase and red fluorescence (TRITC filter cube, excitation wavelength: 532–554 nm, emission wavelength: 570–613 nm) images were captured. To quantitate superoxide levels, files were imported into Image J and masks were manually created around the periphery of the cell based on the phase image and subsequently applied to the TRITC channel to measure intensity. A minimum of 100 cells were analyzed in each independent experiment to obtain mean values.

Cell Migration and Invasion

The various tumor cell types suspended in 0.1% BSA/RPMI and seeded (1×10^5 cells) in the upper compartment of 8 μ M pore diameter BD Transwell membranes (BD) were quantified for cell migration, as described [20]. For cell invasion, the Transwell membranes were coated with Matrigel. In all experiments, NIH3T3 conditioned medium was placed in the lower compartment as a chemoattractant [25]. After 18 h incubation at 37°C, the Transwell membranes from each insert were recovered and cells on the upper side (non-migratory) were scraped off the surface. Cells on the lower side of the membrane were fixed in methanol, rinsed in water, and mounted on glass slides with Vectashield medium containing DAPI (Vector Laboratories). Migrated cells on each membrane were counted in five different fields at 20x magnification by fluorescence microscopy.

Liver Metastasis Model

All experiments involving animals were carried out in accordance with the Guide for the Care and Use of Laboratory Animals of the National Institutes of Health. Protocols were approved by the Institutional Animal Care and Use Committee (IACUC) at The Wistar Institute. A liver metastasis models was performed essentially as described previously [25]. Briefly, PC3 cells stably transfected with control pLKO or ClpP- or ClpX-directed shRNA at 80% confluency were suspended in PBS, pH 7.4, and 50 μ l containing 1×10^6 cells were injected in the spleen of 6–8 wk-old male NOD SCID gamma (NSG, NOD.Cg-Prkdcscid Il2rgtm1 Wjl/SzJ) mice (Jackson Laboratory). Spleens were removed the first day after injection to minimize potentially confounding effects on metastasis due to variable growth of primary tumors. Animals were sacrificed 11 d after injection of the tumor cells, and their livers were resected, fixed in formalin, and paraffin-embedded. Serial liver sections 500 μ m apart ($n = 15$ per each condition) were stained with hematoxylin and eosin and analyzed histologically. Metastatic foci were quantified by morphometry and expressed as number and surface areas of metastatic tumor growth compared to total surface area, as described [25].

Statistical Analysis

Data were analyzed using the two-sided unpaired *t* or chi-square tests using a GraphPad software package (Prism 6.0) for Windows. Data are expressed as mean \pm SD or mean \pm SEM of replicates from a representative experiment out of at least two or three independent determinations. A *p* value of <0.05 was considered statistically significant.

Supporting Information

S1 Data. Excel file containing the raw data for [Fig 2](#).
(XLSX)

S2 Data. Excel file containing the raw data for [Fig 3](#).
(XLSX)

S3 Data. Excel file containing the raw data for [Fig 4](#).
(XLSX)

S4 Data. Excel file containing the raw data for [Fig 5](#).
(XLSX)

S5 Data. Excel file containing the raw data for [Fig 6](#).
(XLSX)

S6 Data. Excel file containing the raw data for [Fig 7](#).
(XLSX)

S7 Data. Excel file containing the raw data for [S1 Fig](#).
(XLSX)

S8 Data. Excel file containing the raw data for [S2 Fig](#).
(XLSX)

S9 Data. Excel file containing the raw data for [S3 Fig](#).
(XLSX)

S10 Data. Excel file containing the raw data for [S4 Fig](#).
(XLSX)

S11 Data. Excel file containing the raw data for [S5 Fig](#).
(XLSX)

S12 Data. Excel file containing the raw data for [S6 Fig](#).
(XLSX)

S13 Data. Excel file containing the raw data for [S7 Fig](#).
(XLSX)

S1 Fig. Mitochondrial survivin regulation of ClpP. (A and B) PC3 cells were treated with vehicle (Veh) or small molecule survivin (SVV) suppressant YM155, incubated with cycloheximide (CHX), and ClpP or SVV protein bands detected by western blotting after CHX release (A) was quantified by densitometry (B). (C and D) The experimental conditions are as in (A and B) except that PC3 cells were transfected with control siRNA (Ctrl) or SVV-directed siRNA and protein bands detected by western blotting after CHX release (C) was quantified by densitometry (D). (E) PC3 cells were transfected with control non-targeting siRNA (Ctrl) or SVV-directed siRNA and analyzed for ClpP mRNA levels by quantitative PCR. Raw data for this figure can be found in [S7 Data](#).
(TIF)

S2 Fig. Analysis of protein folding. (A) PC3 cells were transfected with control siRNA (Ctrl) or ClpP-directed siRNA and analyzed by western blotting. (B) PC3 cells transfected with control siRNA (Ctrl) or ClpP-directed siRNAs, as in (A), were solubilized in the indicated increasing concentrations of detergent (CHAPS), and insoluble (*top*) or soluble (*bottom*) fractions were analyzed by western blotting. CS, citrate synthase. (C and D) PC3 cells transfected with control siRNA (Ctrl) or ClpP-directed siRNA were solubilized in the indicated increasing concentrations of detergent (NP-40) and detergent-insoluble bands were visualized by western blotting (C) with quantification by densitometry (D). (E) PC3 cells were transfected with control non-targeting siRNA (Ctrl) or ClpP- or ClpX-directed siRNA and detergent-insoluble SDHB bands visualized by western blotting were quantified by densitometry at the indicated detergent (CHAPS) concentrations. Raw data for this figure can be found in [S8 Data](#).
(TIF)

S3 Fig. ClpXP regulation of mitochondrial respiration. (A and B) Prostate cancer C4-2 (A) or DU145 (B) cells were transfected with control non-targeting siRNA (Ctrl) or ClpP- or ClpX-directed siRNA and analyzed for Complex II activity. *Right*, quantification of citrate synthase-normalized Complex II activity. *, $p = 0.01$; **, $p = 0.008$. (C–E) PC3 cells transfected with control siRNA (Ctrl) or ClpP- or ClpX-directed siRNA were analyzed for mitochondrial Complex III (C), Complex IV (D), or Complex V (E) activity. *Right*, Quantification of citrate

synthase-normalized mitochondrial complex activities. *, $p = 0.04$. (F) siRNA-transfected PC3 cells, as in (C–E), were analyzed for NAD/NADH ratio. (G and H) PC3 cells transfected with the indicated siRNAs were analyzed for glucose consumption (G) or lactate production (H). ***, $p < 0.0001$. Raw data for this figure can be found in [S9 Data](#).
(TIF)

S4 Fig. Characterization of stable cell lines. (A) PC3 cells were infected with control pLKO or shRNA directed to ClpX or ClpP and selected in puromycin-containing medium, and the indicated clones were analyzed by western blotting. (B and C) Control pLKO-transfectants or ClpX (clone #59) or ClpP (clone #59) shRNA transfectants were analyzed for total mitochondrial content (B) or changes in mitochondrial membrane potential (C) by TMRM labeling and flow cytometry. (D) PC3 cells were transfected with control siRNA (Ctrl) or ClpX- or ClpP-directed siRNA, mixed with the ROS scavengers NAC (N) or MitoTempo (MT), alone or in combination, and analyzed by western blotting. Raw data for this figure can be found in [S10 Data](#).
(TIF)

S5 Fig. ClpP expression in human tumors. (A) Tissue extracts from brain metastasis of non-small cell lung cancer (NSCLC) were separated by SDS gel electrophoresis and analyzed with an antibody to ClpP by western blotting. Undiff, undifferentiated; SCC, squamous cell carcinoma; AdCa, adenocarcinoma. (B) Primary tissue samples representative of the indicated tumor diagnoses were stained with an antibody to ClpP and analyzed by immunohistochemistry (IHC). Quantification of cytosolic ClpP staining in the marked tissue areas was carried out using the Aperio software (Quantification). Ca, carcinoma, AdCa, adenocarcinoma; HL, Hodgkin's Lymphoma; HG, high-grade; IDC, infiltrating ductal carcinoma; ILC, infiltrating lobular carcinoma; GBM, glioblastoma. (C) Correlation between ClpP immunohistochemical (IHC) staining in primary human tumors and tumor grade (Colon AdCa, CNS tumors), Gleason score (prostate AdCa), lymphoma subtype (DLBCL, diffuse large B cell lymphoma; Follicular, follicular lymphoma; Mantle, mantle cell lymphoma; HL, Hodgkin's lymphoma); histotype (lung cancer or breast AdCa; CIS, carcinoma in situ; IDC, infiltrating ductal carcinoma; ILB, infiltrating lobular carcinoma). Mening, meningioma. Data are expressed as mean \pm SEM of a ClpP IHC score per each tumor type examined. (D) Primary tissue samples representative of normal lung, non-small cell lung cancer (NSCLC) that developed (met) or not (no met) distant metastases during a 5-years follow-up, or metastatic NSCLC to the brain were analyzed for ClpP expression by immunohistochemistry (IHC), with quantification of marked areas by Aperio. Raw data for this figure can be found in [S11 Data](#).
(TIF)

S6 Fig. ClpXP regulation of tumor cell proliferation. (A) The indicated tumor cell types were transfected with control siRNA (Ctrl) or ClpX- or ClpP-directed siRNA and analyzed for changes in cell proliferation by direct cell counting. *, $p = 0.013$ – 0.015 ; **, $p = 0.001$ – 0.007 ; ***, $p < 0.0001$. (B) PC3 cells stably transfected with control pLKO or shRNA to ClpX or ClpP were analyzed for colony formation after 7 d by crystal violet staining. **, $p = 0.001$ – 0.004 . (C) PC3 cells transfected with the indicated siRNAs were analyzed for BrdU incorporation by flow cytometry, and the percentage of BrdU⁺ cells was quantified. **, $p = 0.004$; ***, $p < 0.0001$. (D) PC3 cells transfected as in (A) were analyzed for DNA content by propidium iodide staining and flow cytometry, and the percentage of cells in each cell cycle phase was quantified. (E) Breast adenocarcinoma MCF-7 cells were transfected with control siRNA (Ctrl) or ClpP- or ClpX-directed siRNA and analyzed for Complex II activity. *Right*, Quantification of citrate synthase-normalized Complex II activity. **, $p = 0.002$. (F) MCF-7 cells transfected with the

indicated siRNAs were analyzed for oxygen consumption rates (OCR). (G) Breast epithelial MCF-10A cells were transfected with control siRNA (Ctrl) or ClpP- or ClpX-directed siRNA and analyzed for Complex II activity. *Right*, Quantification of citrate synthase-normalized Complex II activity. (H) siRNA-transfected MCF-10A cells as in (G) were analyzed for oxygen consumption rates (OCR). Raw data for this figure can be found in [S12 Data](#). (TIF)

S7 Fig. ClpXP requirement for tumor cell invasion. (A) DU145 or LN229 cells were transfected with control siRNAs or ClpX- or ClpP-directed siRNA and analyzed for Matrigel invasion. $***, p < 0.0001$. (B) LN229 cells were transfected with the indicated siRNAs as in (A) and analyzed by western blotting. (C) PC3 cells were treated with the indicated increasing concentrations of H_2O_2 and analyzed by western blotting. (D and E) PC3 cells were transfected with control siRNA (Ctrl) or Caveolin-1 (Cav1)-directed siRNA and analyzed by western blotting (D) or changes in cell migration (Migr) or cell invasion (Inv) across Transwell membranes (E). $***, p < 0.0001$. (F) PC3 cells transfected with control siRNA (Ctrl) or ClpX- or ClpP-directed siRNA were reconstituted with vector or Akt cDNA and analyzed for cell invasion in a Transwell assay. Raw data for this figure can be found in [S13 Data](#). (TIF)

S1 Methods. Supporting materials and methods.

(DOCX)

S1 Table. Patients' characteristics. NSCLC, non-small cell lung cancer; PNET, pulmonary neuroendocrine tumor; other cancers: breast adenocarcinoma (1), melanoma (1), colorectal adenocarcinoma (1), ovarian carcinoma (1).

(DOCX)

S2 Table. Meta-analysis of ClpP prognostic implications.

(DOCX)

Author Contributions

Conceived and designed the experiments: JHS DCA. Performed the experiments: JHS DBR MCC YCC HYT DWS VV. Analyzed the data: AVK DWS SB LRL DCA. Wrote the paper: JHS DCA. Collection of primary patient samples: PR AP.

References

1. van Oosten-Hawle P, Morimoto RI. Organismal proteostasis: role of cell-nonautonomous regulation and transcellular chaperone signaling. *Genes Dev.* 2014; 28(14):1533–43. doi: [10.1101/gad.241125.114](#) PMID: [25030693](#); PubMed Central PMCID: PMC4102760.
2. Hartl FU, Bracher A, Hayer-Hartl M. Molecular chaperones in protein folding and proteostasis. *Nature.* 2011; 475(7356):324–32. doi: [10.1038/nature10317](#) PMID: [21776078](#).
3. Ciechanover A, Kwon YT. Degradation of misfolded proteins in neurodegenerative diseases: therapeutic targets and strategies. *Exp Mol Med.* 2015; 47:e147. doi: [10.1038/emm.2014.117](#) PMID: [25766616](#); PubMed Central PMCID: PMC4351408.
4. Chevet E, Hetz C, Samali A. Endoplasmic reticulum stress-activated cell reprogramming in oncogenesis. *Cancer Discov.* 2015; 5(6):586–97. doi: [10.1158/2159-8290.CD-14-1490](#) PMID: [25977222](#).
5. Haynes CM, Ron D. The mitochondrial UPR—protecting organelle protein homeostasis. *J Cell Sci.* 2010; 123(Pt 22):3849–55. Epub 2010/11/05. 123/22/3849 [pii] doi: [10.1242/jcs.075119](#) PMID: [21048161](#).
6. Hetz C, Chevet E, Oakes SA. Proteostasis control by the unfolded protein response. *Nat Cell Biol.* 2015; 17(7):829–38. doi: [10.1038/ncb3184](#) PMID: [26123108](#).
7. Taipale M, Jarosz DF, Lindquist S. HSP90 at the hub of protein homeostasis: emerging mechanistic insights. *Nat Rev Mol Cell Biol.* 2010; 11(7):515–28. doi: [10.1038/nrm2918](#) PMID: [20531426](#)

8. Lavery LA, Partridge JR, Ramelot TA, Elnatan D, Kennedy MA, Agard DA. Structural asymmetry in the closed state of mitochondrial Hsp90 (TRAP1) supports a two-step ATP hydrolysis mechanism. *Mol Cell*. 2014; 53(2):330–43. doi: [10.1016/j.molcel.2013.12.023](https://doi.org/10.1016/j.molcel.2013.12.023) PMID: [24462206](https://pubmed.ncbi.nlm.nih.gov/24462206/); PubMed Central PMCID: PMC3947485.
9. Kang BH, Plescia J, Dohi T, Rosa J, Doxsey SJ, Altieri DC. Regulation of tumor cell mitochondrial homeostasis by an organelle-specific Hsp90 chaperone network. *Cell*. 2007; 131(2):257–70. Epub 2007/10/25. doi: [10.1016/j.cell.2007.08.028](https://doi.org/10.1016/j.cell.2007.08.028) PMID: [17956728](https://pubmed.ncbi.nlm.nih.gov/17956728/).
10. Chae YC, Angelin A, Lisanti S, Kossenkova AV, Speicher KD, Wang H, et al. Landscape of the mitochondrial Hsp90 metabolome in tumours. *Nat Commun*. 2013; 4:2139. Epub 2013/07/12. doi: [10.1038/ncomms3139](https://doi.org/10.1038/ncomms3139) PMID: [23842546](https://pubmed.ncbi.nlm.nih.gov/23842546/); PubMed Central PMCID: PMC3732457.
11. Siegelin MD, Dohi T, Raskett CM, Orlowski GM, Powers CM, Gilbert CA, et al. Exploiting the mitochondrial unfolded protein response for cancer therapy in mice and human cells. *J Clin Invest*. 2011; 121(4):1349–60. Epub 2011/03/03. doi: [10.1172/JCI44855](https://doi.org/10.1172/JCI44855) PMID: [21364280](https://pubmed.ncbi.nlm.nih.gov/21364280/); PubMed Central PMCID: PMC3069780.
12. Chae YC, Caino MC, Lisanti S, Ghosh JC, Dohi T, Danial NN, et al. Control of tumor bioenergetics and survival stress signaling by mitochondrial HSP90s. *Cancer Cell*. 2012; 22(3):331–44. Epub 2012/09/15. doi: [10.1016/j.ccr.2012.07.015](https://doi.org/10.1016/j.ccr.2012.07.015) PMID: [22975376](https://pubmed.ncbi.nlm.nih.gov/22975376/).
13. Agorreta J, Hu J, Liu D, Delia D, Turley H, Ferguson DJ, et al. TRAP1 regulates proliferation, mitochondrial function, and has prognostic significance in NSCLC. *Mol Cancer Res*. 2014; 12(5):660–9. doi: [10.1158/1541-7786.MCR-13-0481](https://doi.org/10.1158/1541-7786.MCR-13-0481) PMID: [24567527](https://pubmed.ncbi.nlm.nih.gov/24567527/).
14. Baker TA, Sauer RT. ClpXP, an ATP-powered unfolding and protein-degradation machine. *Biochim Biophys Acta*. 2012; 1823(1):15–28. doi: [10.1016/j.bbamcr.2011.06.007](https://doi.org/10.1016/j.bbamcr.2011.06.007) PMID: [21736903](https://pubmed.ncbi.nlm.nih.gov/21736903/); PubMed Central PMCID: PMC3209554.
15. Kang SG, Ortega J, Singh SK, Wang N, Huang NN, Steven AC, et al. Functional proteolytic complexes of the human mitochondrial ATP-dependent protease, hClpXP. *J Biol Chem*. 2002; 277(23):21095–102. doi: [10.1074/jbc.M201642200](https://doi.org/10.1074/jbc.M201642200) PMID: [11923310](https://pubmed.ncbi.nlm.nih.gov/11923310/).
16. Haynes CM, Petrova K, Benedetti C, Yang Y, Ron D. ClpP mediates activation of a mitochondrial unfolded protein response in *C. elegans*. *Dev Cell*. 2007; 13(4):467–80. doi: [10.1016/j.devcel.2007.07.016](https://doi.org/10.1016/j.devcel.2007.07.016) PMID: [17925224](https://pubmed.ncbi.nlm.nih.gov/17925224/).
17. Al-Furoukh N, Ianni A, Nolte H, Holper S, Kruger M, Wanrooij S, et al. ClpX stimulates the mitochondrial unfolded protein response (UPRmt) in mammalian cells. *Biochim Biophys Acta*. 2015; 1853(10 Pt A):2580–91. doi: [10.1016/j.bbamcr.2015.06.016](https://doi.org/10.1016/j.bbamcr.2015.06.016) PMID: [26142927](https://pubmed.ncbi.nlm.nih.gov/26142927/).
18. Gispert S, Parganlija D, Klittenberg M, Drose S, Wittig I, Mittelbronn M, et al. Loss of mitochondrial peptidase ClpP leads to infertility, hearing loss plus growth retardation via accumulation of CLPX, mtDNA and inflammatory factors. *Hum Mol Genet*. 2013; 22(24):4871–87. doi: [10.1093/hmg/ddt338](https://doi.org/10.1093/hmg/ddt338) PMID: [23851121](https://pubmed.ncbi.nlm.nih.gov/23851121/).
19. Altieri DC. Survivin and IAP proteins in cell-death mechanisms. *Biochem J*. 2010; 430(2):199–205. Epub 2010/08/14. doi: [10.1042/BJ20100814](https://doi.org/10.1042/BJ20100814) PMID: [20704571](https://pubmed.ncbi.nlm.nih.gov/20704571/); PubMed Central PMCID: PMC3198835.
20. Rivadeneira DB, Caino MC, Seo JH, Angelin A, Wallace DC, Languino LR, et al. Survivin promotes oxidative phosphorylation, subcellular mitochondrial repositioning, and tumor cell invasion. *Sci Signal*. 2015; 8(389):ra80. doi: [10.1126/scisignal.aab1624](https://doi.org/10.1126/scisignal.aab1624) PMID: [26268608](https://pubmed.ncbi.nlm.nih.gov/26268608/); PubMed Central PMCID: PMC394539531.
21. Joshi KK, Berge M, Radhakrishnan SK, Viollier PH, Chien P. An Adaptor Hierarchy Regulates Proteolysis during a Bacterial Cell Cycle. *Cell*. 2015; 163(2):419–31. doi: [10.1016/j.cell.2015.09.030](https://doi.org/10.1016/j.cell.2015.09.030) PMID: [26451486](https://pubmed.ncbi.nlm.nih.gov/26451486/); PubMed Central PMCID: PMC394600535.
22. Conlon BP, Nakayasu ES, Fleck LE, LaFleur MD, Isabella VM, Coleman K, et al. Activated ClpP kills persisters and eradicates a chronic biofilm infection. *Nature*. 2013; 503(7476):365–70. doi: [10.1038/nature12790](https://doi.org/10.1038/nature12790) PMID: [24226776](https://pubmed.ncbi.nlm.nih.gov/24226776/); PubMed Central PMCID: PMC394031760.
23. Liu K, Ologbenla A, Houry WA. Dynamics of the ClpP serine protease: a model for self-compartmentalized proteases. *Crit Rev Biochem Mol Biol*. 2014; 49(5):400–12. doi: [10.3109/10409238.2014.925421](https://doi.org/10.3109/10409238.2014.925421) PMID: [24915503](https://pubmed.ncbi.nlm.nih.gov/24915503/).
24. Wallace DC. Mitochondria and cancer. *Nat Rev Cancer*. 2012; 12(10):685–98. Epub 2012/09/25. doi: [10.1038/nrc3365](https://doi.org/10.1038/nrc3365) PMID: [23001348](https://pubmed.ncbi.nlm.nih.gov/23001348/).
25. Caino MC, Chae YC, Vaira V, Ferrero S, Nosotti M, Martin NM, et al. Metabolic stress regulates cytoskeletal dynamics and metastasis of cancer cells. *J Clin Invest*. 2013; 123(7):2907–20. Epub 2013/08/08. doi: [10.1172/JCI67841](https://doi.org/10.1172/JCI67841) PMID: [23921130](https://pubmed.ncbi.nlm.nih.gov/23921130/).
26. Lisanti S, Tavecchio M, Chae YC, Liu Q, Brice AK, Thakur ML, et al. Deletion of the mitochondrial chaperone TRAP-1 uncovers global reprogramming of metabolic networks. *Cell Rep*. 2014; 8(3):671–7.

Epub 2014/08/05. doi: [10.1016/j.celrep.2014.06.061](https://doi.org/10.1016/j.celrep.2014.06.061) PMID: [25088416](https://pubmed.ncbi.nlm.nih.gov/25088416/); PubMed Central PMCID: PMC4127146.

27. Costa AC, Loh SH, Martins LM. Drosophila Trap1 protects against mitochondrial dysfunction in a PINK1/parkin model of Parkinson's disease. *Cell Death Dis.* 2013; 4:e467. doi: [10.1038/cddis.2012.205](https://doi.org/10.1038/cddis.2012.205) PMID: [23328674](https://pubmed.ncbi.nlm.nih.gov/23328674/); PubMed Central PMCID: PMCPMC3563993.
28. Hua G, Zhang Q, Fan Z. Heat shock protein 75 (TRAP1) antagonizes reactive oxygen species generation and protects cells from granzyme M-mediated apoptosis. *J Biol Chem.* 2007; 282(28):20553–60. doi: [10.1074/jbc.M703196200](https://doi.org/10.1074/jbc.M703196200) PMID: [17513296](https://pubmed.ncbi.nlm.nih.gov/17513296/).
29. Altieri DC, Stein GS, Lian JB, Languino LR. TRAP-1, the mitochondrial Hsp90. *Biochim Biophys Acta.* 2012; 1823(3):767–73. doi: [10.1016/j.bbamcr.2011.08.007](https://doi.org/10.1016/j.bbamcr.2011.08.007) PMID: [21878357](https://pubmed.ncbi.nlm.nih.gov/21878357/); PubMed Central PMCID: PMCPMC3263322.
30. Cole A, Wang Z, Coyaud E, Voisin V, Gronda M, Jitkova Y, et al. Inhibition of the Mitochondrial Protease ClpP as a Therapeutic Strategy for Human Acute Myeloid Leukemia. *Cancer Cell.* 2015; 27(6):864–76. doi: [10.1016/j.ccell.2015.05.004](https://doi.org/10.1016/j.ccell.2015.05.004) PMID: [26058080](https://pubmed.ncbi.nlm.nih.gov/26058080/); PubMed Central PMCID: PMCPMC4461837.
31. Diaz J, Mendoza P, Ortiz R, Diaz N, Leyton L, Stupack D, et al. Rab5 is required in metastatic cancer cells for Caveolin-1-enhanced Rac1 activation, migration and invasion. *J Cell Sci.* 2014; 127(Pt 11):2401–6. doi: [10.1242/jcs.141689](https://doi.org/10.1242/jcs.141689) PMID: [24659799](https://pubmed.ncbi.nlm.nih.gov/24659799/); PubMed Central PMCID: PMCPMC4074264.
32. Vander Heiden MG, Cantley LC, Thompson CB. Understanding the Warburg effect: the metabolic requirements of cell proliferation. *Science.* 2009; 324(5930):1029–33. Epub 2009/05/23. doi: [10.1126/science.1160809](https://doi.org/10.1126/science.1160809) PMID: [19460998](https://pubmed.ncbi.nlm.nih.gov/19460998/); PubMed Central PMCID: PMC2849637.
33. Moreno-Sanchez R, Marin-Hernandez A, Saavedra E, Pardo JP, Ralph SJ, Rodriguez-Enriquez S. Who controls the ATP supply in cancer cells? Biochemistry lessons to understand cancer energy metabolism. *Int J Biochem Cell Biol.* 2014; 50:10–23. Epub 2014/02/12. doi: [10.1016/j.biocel.2014.01.025](https://doi.org/10.1016/j.biocel.2014.01.025) PMID: [24513530](https://pubmed.ncbi.nlm.nih.gov/24513530/).
34. Viale A, Pettazzoni P, Lyssiotis CA, Ying H, Sanchez N, Marchesini M, et al. Oncogene ablation-resistant pancreatic cancer cells depend on mitochondrial function. *Nature.* 2014; 514(7524):628–32. Epub 2014/08/15. doi: [10.1038/nature13611](https://doi.org/10.1038/nature13611) PMID: [25119024](https://pubmed.ncbi.nlm.nih.gov/25119024/).
35. Roesch A, Vultur A, Bogeski I, Wang H, Zimmermann KM, Speicher D, et al. Overcoming intrinsic multi-drug resistance in melanoma by blocking the mitochondrial respiratory chain of slow-cycling JARID1B (high) cells. *Cancer Cell.* 2013; 23(6):811–25. Epub 2013/06/15. doi: [10.1016/j.ccr.2013.05.003](https://doi.org/10.1016/j.ccr.2013.05.003) PMID: [23764003](https://pubmed.ncbi.nlm.nih.gov/23764003/); PubMed Central PMCID: PMC3810180.
36. Caino MC, Ghosh JC, Chae YC, Vaira V, Rivadeneira DB, Favarsani A, et al. PI3K therapy reprograms mitochondrial trafficking to fuel tumor cell invasion. *Proc Natl Acad Sci U S A.* 2015; 112(28):8638–43. doi: [10.1073/pnas.1500722112](https://doi.org/10.1073/pnas.1500722112) PMID: [26124089](https://pubmed.ncbi.nlm.nih.gov/26124089/); PubMed Central PMCID: PMCPMC4507184.
37. LeBleu VS, O'Connell JT, Gonzalez Herrera KN, Wikman H, Pantel K, Haigis MC, et al. PGC-1alpha mediates mitochondrial biogenesis and oxidative phosphorylation in cancer cells to promote metastasis. *Nat Cell Biol.* 2014; 16(10):992–1003. Epub 2014/09/23. doi: [10.1038/ncb3039](https://doi.org/10.1038/ncb3039) PMID: [25241037](https://pubmed.ncbi.nlm.nih.gov/25241037/).
38. Fulda S, Galluzzi L, Kroemer G. Targeting mitochondria for cancer therapy. *Nature reviews Drug discovery.* 2010; 9(6):447–64. doi: [10.1038/nrd3137](https://doi.org/10.1038/nrd3137) PMID: [20467424](https://pubmed.ncbi.nlm.nih.gov/20467424/).
39. Di Cristofori A, Ferrero S, Bertolini I, Gaudioso G, Russo MV, Berno V, et al. The vacuolar H⁺ ATPase is a novel therapeutic target for glioblastoma. *Oncotarget.* 2015. PMID: [26020805](https://pubmed.ncbi.nlm.nih.gov/26020805/).
40. Vaira V, Favarsani A, Dohi T, Maggioni M, Nosotti M, Tosi D, et al. Aberrant overexpression of the cell polarity module scribble in human cancer. *Am J Pathol.* 2011; 178(6):2478–83. doi: [10.1016/j.ajpath.2011.02.028](https://doi.org/10.1016/j.ajpath.2011.02.028) PMID: [21549346](https://pubmed.ncbi.nlm.nih.gov/21549346/); PubMed Central PMCID: PMCPMC3124121.

Mitochondrial Akt Regulation of Hypoxic Tumor Reprogramming

Highlights

- A pool of active Akt is recruited to tumor mitochondria during hypoxia
- Mitochondrial Akt phosphorylates PDK-1 in hypoxia on a T346 site
- Akt-PDK1 activation maintains tumor cell proliferation in hypoxia
- PDK1 phosphorylation by Akt is a negative prognostic factor in gliomas

Authors

Young Chan Chae, Valentina Vaira, M. Cecilia Caino, ..., Lucia R. Languino, David W. Speicher, Dario C. Altieri

Correspondence

daltieri@wistar.org

In Brief

Chae et al. identify a pool of phosphorylated Akt that translocates to the mitochondria during hypoxia. Mitochondrial Akt phosphorylates PDK1, which supports cell survival and proliferation during hypoxia, and elevated Akt-dependent phosphorylation of PDK1 correlates with reduced survival of glioma patients.

Accession Numbers

PXD004024



Mitochondrial Akt Regulation of Hypoxic Tumor Reprogramming

Young Chan Chae,¹ Valentina Vaira,^{2,3,4} M. Cecilia Caino,¹ Hsin-Yao Tang,⁴ Jae Ho Seo,¹ Andrew V. Kossenkov,⁵ Luisa Ottobri,^{4,6} Cristina Martelli,⁴ Giovanni Lucignani,^{7,8} Irene Bertolini,^{3,4} Marco Locatelli,⁹ Kelly G. Bryant,¹ Jagadish C. Ghosh,¹ Sofia Lisanti,¹ Bonsu Ku,¹⁰ Silvano Bosari,^{3,4} Lucia R. Languino,¹¹ David W. Speicher,^{5,12} and Dario C. Altieri^{1,*}

¹Prostate Cancer Discovery and Development Program, Tumor Microenvironment and Metastasis Program, The Wistar Institute, 3601 Spruce Street, Philadelphia, PA 19104, USA

²Istituto Nazionale Genetica Molecolare “Romeo and Enrica Invernizzi”, Milan 20122, Italy

³Division of Pathology, Fondazione IRCCS Ca’ Granda Ospedale Maggiore Policlinico, Milan 20122, Italy

⁴Department of Pathophysiology and Transplantation, University of Milan, Milan 20122, Italy

⁵Center for Systems and Computational Biology, The Wistar Institute, Philadelphia, PA 19104, USA

⁶Institute for Molecular Bioimaging and Physiology (IBFM), National Research Council (CNR), Milan 20090, Italy

⁷Department of Health Sciences, University of Milan, Milan 20142, Italy

⁸Department of Diagnostic Services, Unit of Nuclear Medicine, San Paolo Hospital, Milan 20142, Italy

⁹Division of Neurosurgery, Fondazione IRCCS Ca’ Granda Ospedale Maggiore Policlinico, Milan 20122, Italy

¹⁰Functional Genomics Research Center, Korea Research Institute of Bioscience and Biotechnology, 125 Gwahak-ro, Yuseong-gu, Daejeon 305-806, Republic of Korea

¹¹Department of Cancer Biology, Kimmel Cancer Center, Thomas Jefferson University, Philadelphia, PA 19107, USA

¹²Molecular and Cellular Oncogenesis Program, The Wistar Institute, Philadelphia, PA 19104, USA

*Correspondence: daltieri@wistar.org

<http://dx.doi.org/10.1016/j.ccell.2016.07.004>

SUMMARY

Hypoxia is a universal driver of aggressive tumor behavior, but the underlying mechanisms are not completely understood. Using a phosphoproteomics screen, we now show that active Akt accumulates in the mitochondria during hypoxia and phosphorylates pyruvate dehydrogenase kinase 1 (PDK1) on Thr346 to inactivate the pyruvate dehydrogenase complex. In turn, this pathway switches tumor metabolism toward glycolysis, antagonizes apoptosis and autophagy, dampens oxidative stress, and maintains tumor cell proliferation in the face of severe hypoxia. Mitochondrial Akt-PDK1 signaling correlates with unfavorable prognostic markers and shorter survival in glioma patients and may provide an “actionable” therapeutic target in cancer.

INTRODUCTION

Hypoxia is a nearly universal feature of tumor growth (Hockel and Vaupel, 2001), conferring worse disease outcome via protection from apoptosis (Graeber et al., 1996), resistance to therapy (Tredan et al., 2007), and enhanced metastatic competence (Cox et al., 2015). This pathway requires the transcriptional activity of hypoxia-inducible factor 1 (HIF1), a master regulator of oxygen homeostasis (Keith et al., 2012) that becomes stabilized upon

drops in oxygen pressure by escaping prolyl hydroxylation and proteasome-dependent destruction by the von Hippel-Lindau tumor suppressor (Semenza, 2013). In turn, nuclear localized HIF1 contributes to oncogene signaling (Mazumdar et al., 2010), angiogenesis (Ravi et al., 2000), cell invasion (Gilkes et al., 2014), and tumor metabolic reprogramming.

In this context, mitochondria are the primary sites of hypoxia-induced metabolic reprogramming in tumors (Denko, 2008). This response involves HIF1-dependent transcription of mitochondrial

Significance

The ability to flexibly adapt to an unfavorable microenvironment is a distinctive feature of tumor cells, engendering treatment resistance and unfavorable disease outcome. Low oxygen pressure, or hypoxia, is a powerful driver of tumor adaptation, but “druggable” therapeutic target(s) in this response have remained elusive. Here, we show that hypoxic tumors recruit a pool of active Akt to mitochondria, culminating with Akt phosphorylation of the metabolic gatekeeper, pyruvate dehydrogenase kinase 1. This phosphorylation step improves tumor fitness, preserves tumor cell proliferation in the face of severe hypoxia, and is a negative prognostic factor in glioma patients. Repurposing small-molecule Akt inhibitors currently in the clinic may provide an approach to prevent hypoxic reprogramming and improve anticancer therapy.

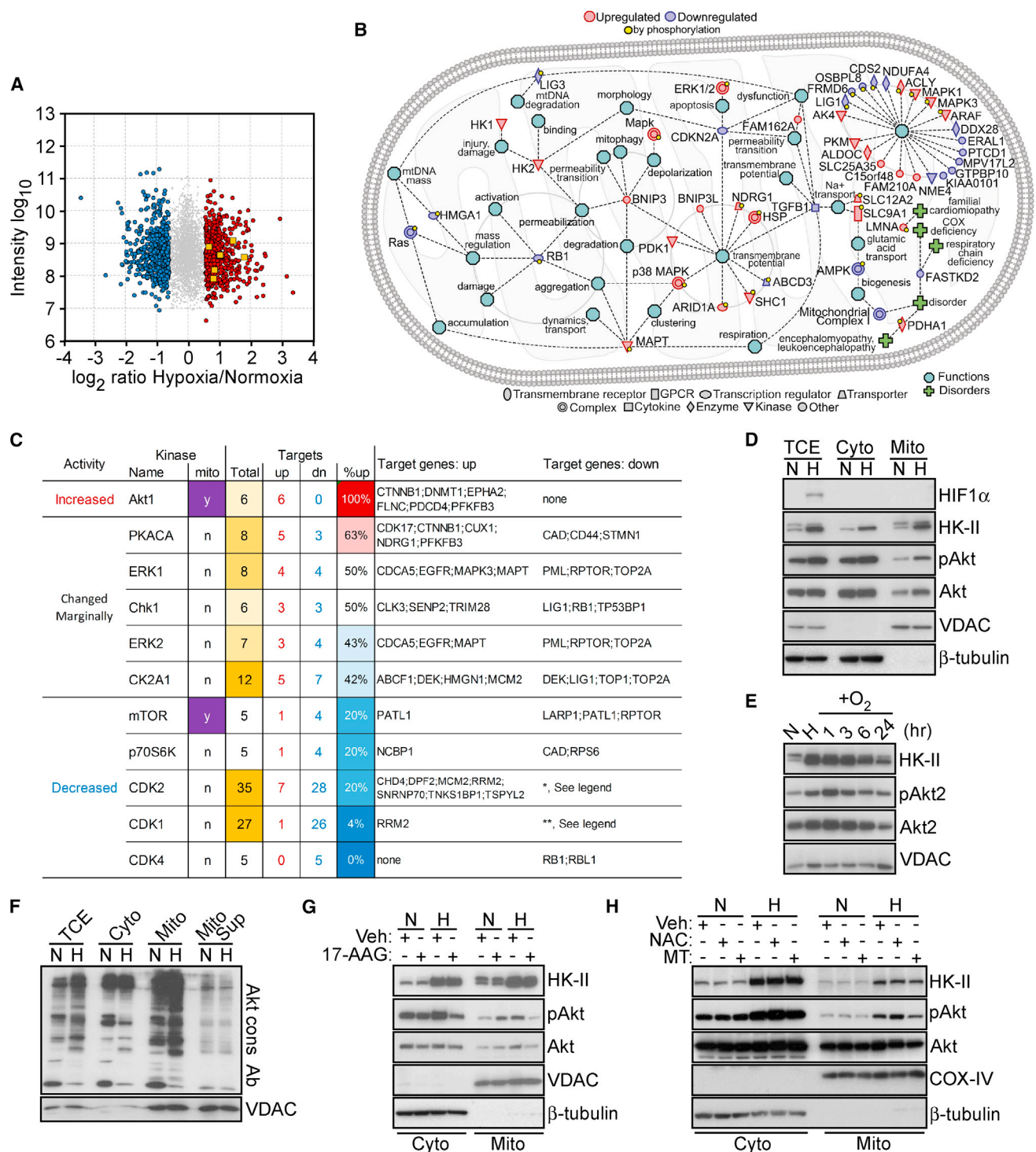


Figure 1. Mitochondrial Phosphoproteome in Hypoxia

(A) Phosphoproteome of prostate adenocarcinoma PC3 cells in hypoxia versus normoxia. Identified phosphosites met a minimum MaxQuant localization probability of 0.75 and a score difference of 5. Fold changes were calculated from the normalized heavy/light SILAC (stable isotope labeling by amino acids in cell culture) ratio. Six Akt target proteins showing increased phosphorylation in hypoxia are indicated. Gray, not significant; red, upregulated; blue, downregulated; yellow squares, Akt targets.

(B) Ingenuity pathway analysis of mitochondrial phosphoproteome and global proteome in hypoxia.

(C) Kinases for which at least five known targets showed significant changes in phosphorylation in hypoxic versus normoxic conditions as in (A). Up, upregulation; Dn, downregulation. *The modulated genes are: *ARID1A*; *HIST1H1E*; *HMGA1*; *LARP1*; *LIG1*; *LIG3*; *LMNB2*; *LRCH3*; *LRWD1*; *MARCKS*; *MED1*; *MKI67*; *NCL*;

(legend continued on next page)

pyruvate dehydrogenase kinase (PDK) (Kim et al., 2006; Papan-dreou et al., 2006), which in turn phosphorylates the pyruvate dehydrogenase complex (PDC) on three separate sites (Patel et al., 2014). By suppressing the oxidative decarboxylation of pyruvate into acetyl-CoA (Patel et al., 2014), an active PDK shuts off oxidative phosphorylation, lowers the production of toxic reactive oxygen species (ROS), and switches tumor bioenergetics toward glycolysis (Denko, 2008), a driver of more aggressive disease traits (Gatenby and Gillies, 2004). What has remained unclear, however, is whether HIF1-dependent transcription is the sole mechanism for PDK activation in hypoxia (Kim et al., 2006; Papan-dreou et al., 2006), and the existence of other potential regulators of this response has not been widely investigated. In this study, we examined mechanisms of the tumor response to hypoxia.

RESULTS

A Mitochondrial Akt Phosphoproteome in Hypoxia

We began this study by profiling the mitochondrial phosphoproteome of prostate adenocarcinoma PC3 cells exposed to severe hypoxia (<0.5% oxygen for 48 hr) versus normoxia. A total of 4,236 phosphosites were identified in the phosphopeptide-enriched samples, with a large number of changes in phosphorylation level in hypoxia/normoxia samples (Figures 1A and S1A). In total, 1,329 phosphosites showed a significant change (minimum fold change of 1.6) in at least one sample analyzed (Figure 1A). By bioinformatics analysis, the mitochondrial phosphoproteome in hypoxia contained regulators of organelle integrity, bioenergetics, gene regulation, and proteostasis (Figure 1B), which are functionally implicated in tumor cell proliferation, motility, invasion, and apoptosis (Figure S1B). To complement these data, we also examined changes in the global mitochondrial proteome in hypoxia versus normoxia. A total of 5,583 proteins were identified in this analysis, and 267 of these proteins showed a significant change in hypoxia/normoxia samples (Figure S1C). Many of the phosphosites were not modulated at the protein level, suggesting that these phosphorylation events were independent of protein expression. In addition, the hypoxia-regulated mitochondrial phosphoproteome contained a discrete “Akt signature” (Figure 1A), characterized by increased phosphorylation of six Akt target proteins in hypoxia versus normoxia (Figure 1C).

Based on these results, we next looked at a role of Akt in the tumor response to hypoxia. Exposure of PC3 cells to hypoxia resulted in increased recruitment of Akt to mitochondria, whereas the cytosolic levels of Akt were unchanged between hypoxia and normoxia (Figures 1D and S1D). The hypoxia-regulated pool of

mitochondrial Akt was “active” as it was phosphorylated on Ser473 (Figure 1D) and persisted for up to 24 hr after re-oxygenation (Figures 1E and S1E). Consistent with these results, hypoxia was accompanied by increased phosphorylation of a set of mitochondrial proteins recognized by an antibody to the Akt consensus phosphorylation sequence, RxRxxS/T (Akt cons Ab) (Figure 1F). Preincubation of mitochondrial extracts with Akt cons Ab (Figure 1F), or silencing Akt2 by small interfering RNA (siRNA) (Figure S1F), removed the mitochondrial proteins recognized by Akt cons Ab in hypoxia, confirming the specificity of this response and Akt-directed phosphorylation activity in mitochondria in hypoxia. Silencing Akt1 had minimal effect (Figure S1F). siRNA silencing of HIF1 α did not affect Akt recruitment to mitochondria in hypoxia (Figure S1G), suggesting that this pathway did not require HIF1-dependent transcription. In addition, depletion of HIF1 α did not affect Akt levels in the cytosol or mitochondria under normoxic conditions, whereas phosphorylated Akt2 levels were increased in the cytosol in response to hypoxia (Figure S1G). As detected by Akt cons Ab, the expression levels of downstream Akt-phosphorylated target molecules were unchanged in normoxic or hypoxic conditions (Figure 1F). In response to hypoxia, active Akt was found predominantly in the mitochondrial inner membrane, and, to a lesser extent, the matrix (Figure S1H).

The mechanism(s) of how Akt is recruited to mitochondria in hypoxia was further investigated. We found that blocking the chaperone activity of heat shock protein-90 (Hsp90) with 17-allylaminogeldanamycin (17-AAG) prevented the accumulation of mitochondrial Akt in hypoxia (Figure 1G). Also, scavenging mitochondrial ROS with Mito-Tempo inhibited Akt recruitment to mitochondria (Figure 1H). The antioxidant N-acetylcysteine (NAC) had no effect (Figure 1H), identifying mitochondria-derived ROS as a critical stimulus for mitochondrial accumulation of Akt in hypoxia.

PDK1 Is a Phosphorylation Target of Mitochondrial Akt in Hypoxia

We next set up a 1D proteomics screen to identify mitochondrial proteins phosphorylated by Akt in hypoxia (Figure 2A). Immune complexes precipitated with Akt cons Ab from normoxic or hypoxic PC3 cells contained bands with molecular weights of ~35 to ~120 kDa that were more abundant in hypoxia (Figure S2A). Preclearing mitochondrial extracts with Akt cons Ab removed most of these proteins, validating the specificity of the immunoprecipitation step. From these experiments, we identified 84 high-confidence Akt substrates differentially expressed in hypoxia using mass spectrometry (Table S1). Sixteen of these

NPM1; NUCKS1; PDS5B; PTPN2; RB1; RBL1; RBL2; SAMHD1; SETDB1; TERF2; VIM. **The modulated genes are: *DUT; EEF1D; HIST1H1E; HMG1A; IRS2; LIG1; LIG3; LMNA; LMNB1; MAP4; NOLC1; NPM1; NUCKS1; PDS5B; PTPN2; RB1; SAMHD1; TCOF1; TOP2A; TPX2; VIM.*

(D) PC3 cells in normoxia (N) or hypoxia (H) were fractionated in cytosol (Cyto) or mitochondrial (Mito) extracts and analyzed by western blotting. pAkt, phosphorylated Akt (Ser473); TCE, total cell extracts.

(E) PC3 cells in hypoxia (H) were exposed to re-oxygenation (O₂) for the indicated time intervals and analyzed by western blotting.

(F) The indicated subcellular fractions isolated from normoxic (N) or hypoxic (H) PC3 cells were analyzed with an antibody to the Akt consensus phosphorylation site RxRxxS/T (Akt cons Ab) by western blotting. Mito Sup, supernatant of mitochondrial extracts after preclearing with Akt cons Ab.

(G) PC3 cells in normoxia (N) or hypoxia (H) were treated with vehicle (Veh) or Hsp90 small-molecule inhibitor 17-AAG (5 μ M for 6 hr), and cytosolic (Cyto) or mitochondrial (Mito) extracts were analyzed by western blotting.

(H) PC3 cells in normoxia (N) or hypoxia (H) were treated with vehicle (Veh), the antioxidant N-acetyl cysteine (NAC, 1 mM) or mitochondria-specific ROS scavenger, Mito-Tempo (MT, 25 μ M), and subcellular fractions were analyzed by western blotting. See also Figure S1.

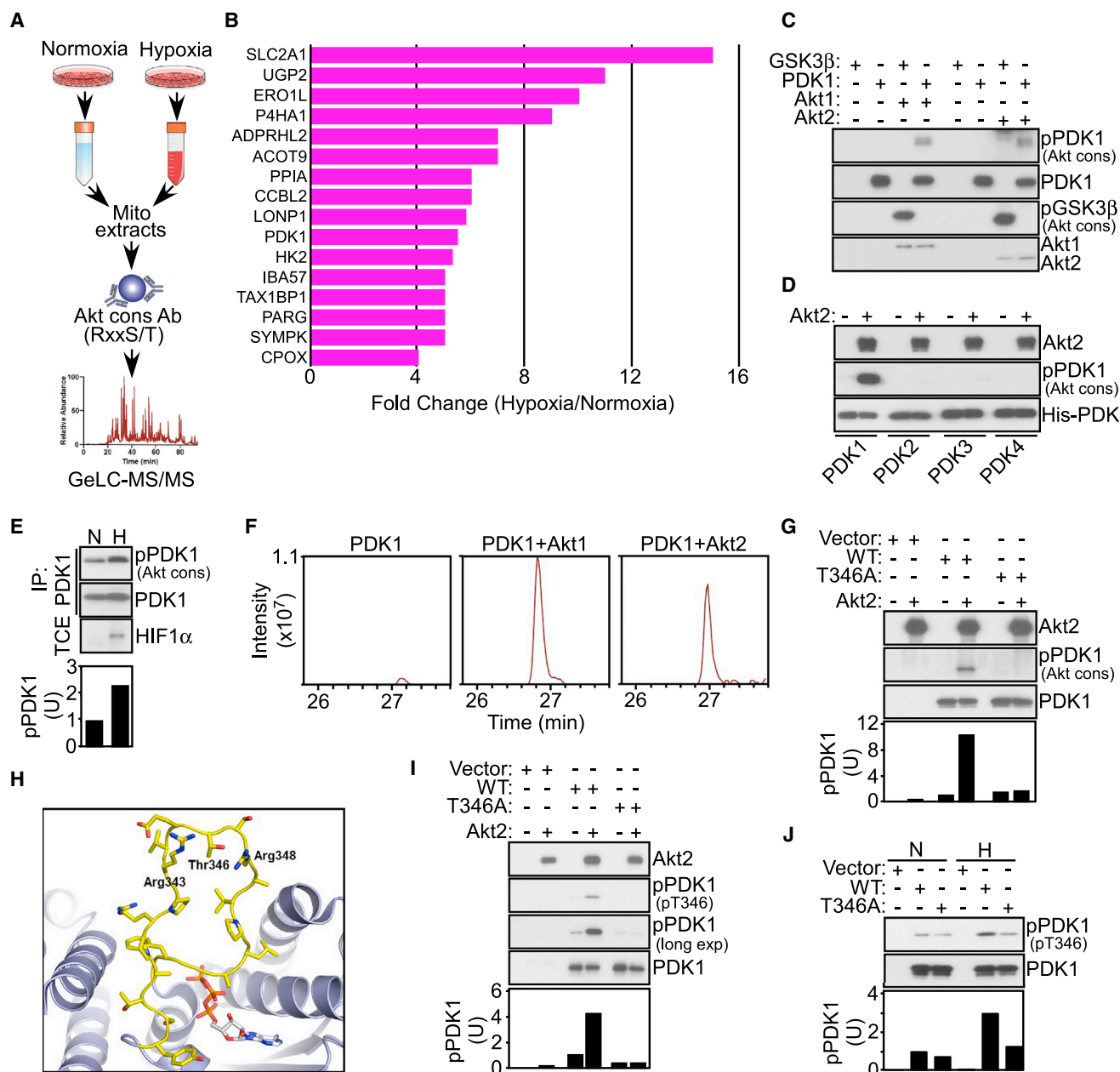


Figure 2. Mitochondrial Akt Phosphorylation of PDK1

(A) Schematic diagram for the identification of a mitochondrial Akt phosphoproteome in hypoxic versus normoxic PC3 cells.

(B) Mitochondrial proteins reacting with Akt cons Ab showing differential expression in hypoxic versus normoxic PC3 cells.

(C) Recombinant PDK1 or GSK3β was mixed in a kinase assay with active Akt1 or Akt2, and phosphorylated bands were detected with Akt cons Ab by western blotting.

(D) The indicated PDK isoforms were mixed in the presence or absence of active Akt2 in a kinase assay, and phosphorylated bands were detected with Akt cons Ab by western blotting.

(E) PC3 cells in normoxia (N) or hypoxia (H) were immunoprecipitated (IP) with an antibody to PDK1 followed by western blotting. HIF1α reactivity (bottom) was used as a marker of hypoxia. Bottom, densitometric quantification of phosphorylated (p) PDK1 bands. U, a.u.

(F) Extracted ion chromatogram of the PDK1-phosphorylated T346 chymotryptic peptide (STAPRPRVEpTSRAVPL, m/z = 908.9751) resulting from incubation with or without active Akt1 or Akt2 in a kinase assay.

(G) PC3 cells were transfected with vector or Flag-tagged wild-type (WT) PDK1 or the T346A PDK1 mutant, IP with an antibody to Flag, and immune complexes were mixed with active Akt2 in a kinase assay followed by western blotting with Akt cons Ab. Bottom, densitometric quantification of phosphorylated (p) PDK1 bands. U, a.u.

(H) Molecular dynamics simulation of the structure of PDK1 (ribbon) with stick representation of residues 336–356 comprising the “ATP lid.” The ATP molecule is derived from the structure of PDK3-L2-ATP (PDB: 1Y8P) superimposed onto the structure of PDK1. The protein is presented as ribbon drawings. The loop is

(legend continued on next page)

molecules were known mitochondrial proteins (Figure 2B), including hypoxia- and HIF1-regulated effectors of bioenergetics (UGP2, SLC2A1, PDK1, HK2), extracellular matrix remodeling (P4HA1), Ca^{2+} homeostasis at the ER-mitochondria interface (Ero1L), oxidative phosphorylation (LonP1, IBA57), and metabolism (Acot9). Due to previously published work suggesting the importance of PDK1 in the tumor hypoxic response, we next focused on PDK1 as a potential substrate of mitochondrial Akt in hypoxia. In kinase assays, active Akt1 or Akt2 readily phosphorylated PDK1, as well as control GSK3 β , as determined by western blotting with Akt cons Ab (Figure 2C). This phosphorylation event was selective for PDK1, as related PDK2, PDK3, or PDK4 isoforms were unreactive (Figure 2D). In addition, PDK1 immune complexes reacted with Akt cons Ab preferentially in hypoxia (Figure 2E) and, reciprocally, immune complexes precipitated with Akt cons Ab in hypoxia contained PDK1 (Figure S2B), consistent with the model of Akt phosphorylation of PDK1 in hypoxia.

We next looked for potential Akt phosphorylation sites in PDK1 by liquid chromatography-tandem mass spectrometry analysis of chymotrypsin digests of Akt-phosphorylated PDK1 in a kinase assay separated by SDS-PAGE (Figure S2C). We identified Thr346 (T346) in a number of PDK1 chymotryptic peptides, including the sequence STAPRRVE_pTSRAVPL (m/z = 908.9751) as the sole phospho-amino acid modified by Akt1 or Akt2, compared with control (Figure 2F). The PDK1 sequence surrounding T346 matched an Akt consensus phosphorylation site, RxRxxS/T (Figure S2D), which was not present in PDK2, PDK3, or PDK4 (Figure S2E). Consistent with these data, active Akt2 phosphorylated wild-type (WT) PDK1 but not a phosphorylation-defective Thr346→Ala (T346A) PDK1 mutant in transfected PC3 cells (Figure 2G). In the PDK1 crystal structure, T346 is predicted to localize to a flexible, “ATP lid” hinge region (Figure 2H), positioned to affect ATP loading and kinase activation.

To independently validate these findings, we next generated a phospho-specific antibody to phosphorylated T346 (pT346 Ab) in PDK1. The pT346 Ab dose-dependently reacted with the phosphorylated PDK1 peptide CAPRRVE(pT)SRAVPLA, but not the non-phosphorylated sequence (Figure S2F). A second antibody raised against the non-phosphorylated sequence recognized the non-phosphorylated PDK1 peptide (Figure S2G). Under these conditions, pT346 Ab reacted with Akt2-phosphorylated WT PDK1, but not the T346A PDK1 mutant (Figure 2I). Consistent with the model that T346 phosphorylation is hypoxia sensitive, WT PDK1, but not T346A PDK1, precipitated from hypoxic PC3 cells reacted with pT346 Ab (Figure 2J). pT346 Ab only weakly reacted with WT or T346A PDK1 precipitated from normoxic cells (Figure 2J).

Finally, we generated clones of PC3 cells stably silenced for endogenous PDK1 by short hairpin RNA (shRNA). pT346 Ab did not react with these cells in normoxia (Figure S2H). In

contrast, pLKO transfectants reacted with pT346 Ab in hypoxia, and this response was abolished by shRNA silencing of PDK1 (Figure S2H).

The Akt-PDK1 Phosphorylation Axis in Hypoxia

Expression of WT PDK1 in hypoxic PC3 cells increased the phosphorylation of the E1 α catalytic subunit (PDHE1) of the PDC (Figure 3A) on site 1 (Ser264 in the mature protein), one of three regulatory phosphorylation sites (Patel et al., 2014). Conversely, expression of the T346A PDK1 mutant reduced PDHE1 phosphorylation in hypoxia (Figure 3A), and no PDHE1 phosphorylation was detected in normoxia (Figure 3A). Immune complexes of the WT or T346A PDK1 mutant contained comparable amounts of the PDC component, PDHE1 α , suggesting that T346 does not contribute to a PDK1-PDC complex (Figure S3A). In a kinase assay, active Akt2 increased PDK1 phosphorylation of PDHE1 (Figure 3B). While WT PDK1 phosphorylated PDHE1 in the presence of Akt2 (Figure 3C), the T346A PDK1 mutant was ineffective (Figure 3C). Consistent with these data, increased PDHE1 phosphorylation was detected only in the presence of Akt2 and PDK1, but not PDK2, PDK3, or PDK4 (Figure S3B). Silencing of Akt2 inhibited PDHE1 phosphorylation in hypoxia, whereas Akt1 knockdown only had a partial effect (Figure 3D). As a complementary approach, we used a pan-Akt small-molecule inhibitor, MK2206, which indistinguishably suppressed Akt phosphorylation in hypoxia and normoxia (Figure S3C). Incubation of PC3 cells with MK2206 suppressed PDHE1 phosphorylation in hypoxia (Figure 3E). This response was specific because PDK1 immunoprecipitated from MK2206-treated cells also failed to phosphorylate PDHE1 in a kinase assay in hypoxia (Figure S3D). In normoxia, MK2206 had no effect on PDHE1 phosphorylation in cell extracts (Figure 3E) or in a kinase assay with immunoprecipitated PDK1 (Figure S3D), validating the specificity of Akt-directed phosphorylation in hypoxic conditions.

As an independent approach, we next generated WT or kinase dead (KD) Akt2 constructs targeted to the mitochondria by the cytochrome c oxidase subunit 8 mitochondrial import sequence. Similar to the endogenous protein, mitochondrial-targeted Akt2 accumulated in various submitochondrial fractions (Figure S3E). Functionally, mitochondrial-targeted Akt2-KD inhibited PDHE1 phosphorylation in hypoxic PC3 cells (Figure 3F), whereas non-mitochondrial-targeted Akt2-KD had no effect. There was no PDHE1 phosphorylation in the cytosol of hypoxic or normoxic tumor cells, and Akt2-KD or mitochondrial-targeted Akt2-KD had no effect in these settings (Figure S3F). Reciprocally, forced expression of mitochondrial-targeted WT Akt2 was sufficient to increase PDHE1 phosphorylation even in the absence of hypoxia (Figure S3G).

Finally, we reconstituted PDK1-depleted cells with various PDK1 cDNAs. Expression of WT PDK1 in these settings restored PDHE1 phosphorylation in hypoxia, whereas T346A PDK1

colored in yellow and the rest of the protein is in navy. The side chains of the loop and the ligand are shown as sticks, colored red for oxygen, blue for nitrogen, and orange for phosphate. The predicted location of Thr346 as well as Arg343 and Arg348 is shown.

(I) The experimental conditions are as in (G) except that Flag-PDK1 immune complexes mixed with active Akt2 in a kinase assay were analyzed with phospho-specific pT346 Ab by western blotting. Exp., exposure. Bottom, densitometric quantification of phosphorylated (p) PDK1 bands. U, a.u.

(J) Flag-PDK1 immune complexes as in (G) were precipitated from PC3 cells in normoxia (N) or hypoxia (H) and analyzed with pT346 Ab by western blotting. Bottom, densitometric quantification of pPDK1 bands. U, a.u. See also Figure S2 and Table S1.

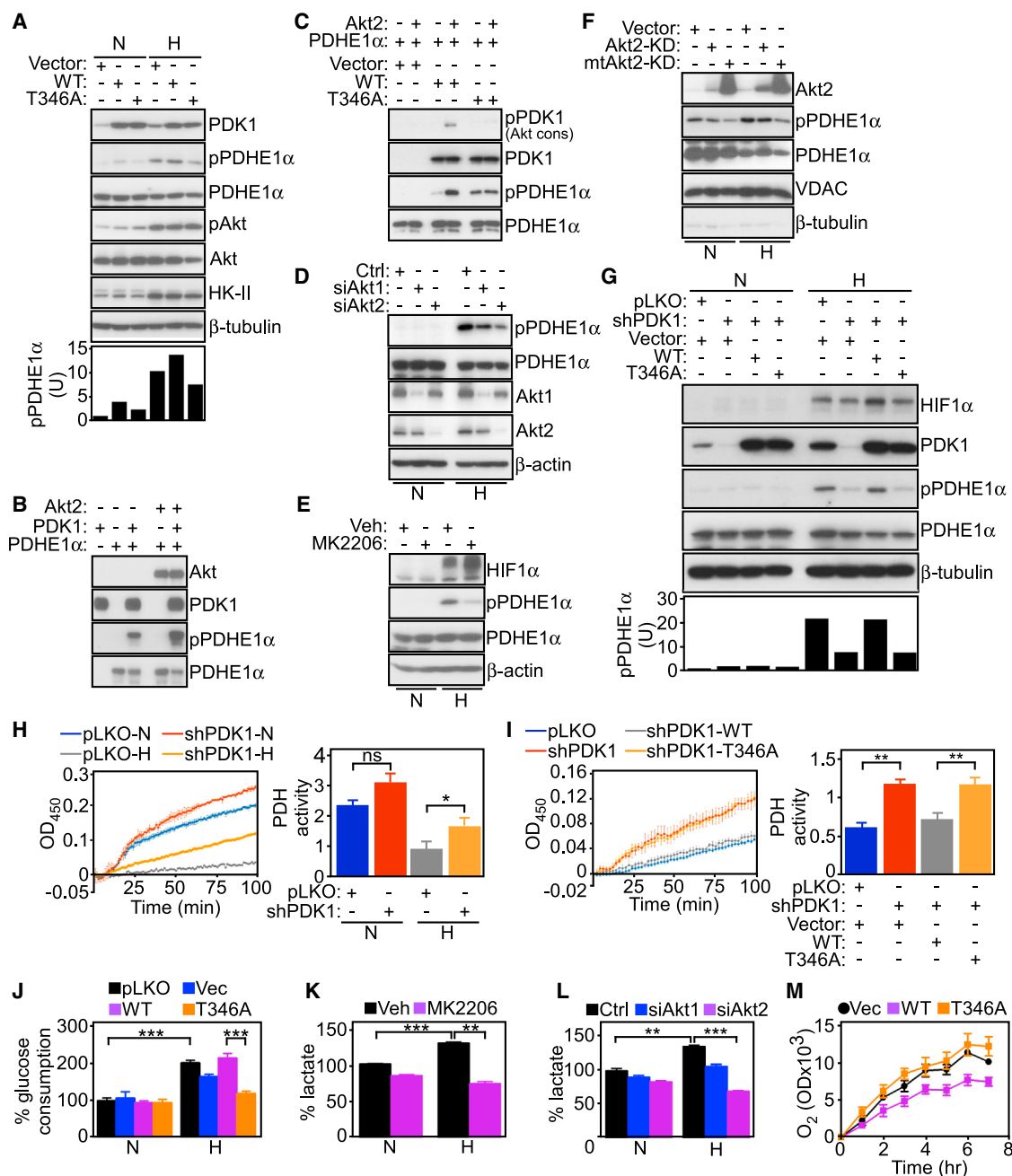


Figure 3. A Mitochondrial Akt-PDK1-PDHE1 Phosphorylation Axis in Hypoxia

(A) PC3 cells in normoxia (N) or hypoxia (H) were transfected with vector, WT PDK1, or the T346A PDK1 mutant and analyzed by western blotting. Bottom, densitometric quantification of phosphorylated (p) PDHE1 bands. U, a.u.

(B) The indicated recombinant proteins were mixed in a kinase assay and analyzed by western blotting.

(C) PC3 cells transfected with vector or the indicated Flag-tagged WT PDK1 or the T346A PDK1 mutant were IP with an antibody to Flag, and immune complexes were mixed in a kinase assay with recombinant Akt2 and PDHE1 followed by western blotting.

(D) PC3 cells in normoxia (N) or hypoxia (H) were transfected with control siRNA (Ctrl) or siRNA to Akt1 or Akt2, and analyzed by western blotting.

(E) PC3 cells in normoxia (N) or hypoxia (H) were treated with vehicle control (Veh) or a small-molecule Akt inhibitor, MK2206 (1 μ M), and analyzed by western blotting.

(F) PC3 cells in normoxia (N) or hypoxia (H) were transfected with vector, Akt-kinase dead (Akt-KD), or the mitochondrial-targeted Akt-KD (mtAkt-KD) mutant, and mitochondrial extracts (Mito) were analyzed by western blotting.

(G) PC3 cells in normoxia (N) or hypoxia (H) were transduced with pLKO or PDK1-directed shRNA, reconstituted with vector, WT PDK1, or the T346A PDK1 mutant and analyzed by western blotting. Bottom, densitometric quantification of phosphorylated (p) PDHE1 bands. U, a.u.

(H) PC3 cells transduced with pLKO or PDK1-directed shRNA were analyzed for PDH activity in normoxia (N) or hypoxia (H). Left, representative tracings (n = 4). Right, quantification of PDH activity. ns, not significant. Mean \pm SEM. *p = 0.03.

(legend continued on next page)

mutant had no effect (Figure 3G). With respect to its enzymatic function, PDK1 knockdown increased PDH activity in normoxic PC3 cells (Figure 3H). Hypoxic cells showed reduced PDH activity, and this response was partially rescued by shRNA silencing of PDK1 (Figure 3H). Reconstitution of these cells with WT PDK1, but not the T346A PDK1 mutant, suppressed PDH activity in hypoxia (Figure 3I). In addition, expression of Akt-KD or mitochondrial-targeted Akt-KD in PC3 cells had no effect on PDH activity in normoxia, but modestly elevated PDH function in hypoxia (Figure S3H), consistent with loss of an Akt-regulated inhibitory function of PDK1 in these settings. Vector or non-mitochondrial-targeted Akt2-KD had no effect (Figure S3H).

Mitochondrial Akt-PDK1 Phosphorylation Controls Tumor Metabolic Reprogramming

To understand how mitochondrial Akt-PDK1 signaling affects tumor behavior, we first looked at potential changes in cancer metabolism. Consistent with previous studies, hypoxia stimulated glycolytic metabolism in tumor cells, characterized by increased glucose consumption (Figure 3J) and lactate production (Figure 3K). Mitochondrial Akt-PDK1 signaling was important for this response, as PDK1 knockdown reduced glucose consumption in hypoxia, whereas reconstitution of targeted cells with WT PDK1, but not the T346A PDK1 mutant, restored glycolysis (Figure 3J). Similarly, Akt inhibition with MK2206 (Figure 3K) or silencing of Akt2 (Figure 3L) impaired metabolic reprogramming, reducing lactate production in hypoxia. Normoxic cultures were not affected (Figures 3K and 3L), and Akt1 knockdown had only partial effect (Figure 3L). Consistent with a metabolic switch toward glycolysis (Kim et al., 2006; Pandreou et al., 2006), PC3 cells reconstituted with WT PDK1 exhibited reduced oxygen consumption, a marker of oxidative phosphorylation, whereas expression of the T346A PDK1 mutant restored oxygen consumption (Figure 3M), further supporting a role of mitochondrial Akt-PDK1 signaling in hypoxic metabolic reprogramming.

Mitochondrial Akt-PDK1 Phosphorylation In Vivo

When analyzed in time course experiments, hypoxia increased phosphorylation of Akt1 and Akt2, as well as PDHE1, starting at 3 and 6 hr, respectively (Figure S4A). The overall hypoxic response under these conditions was cell-type specific. Akt inhibition strongly reduced PDHE1 phosphorylation in prostate adenocarcinoma (DU145), lung adenocarcinoma (A549), and glioblastoma (GBM) (LN229), but had no effect on PDHE1 phosphorylation in breast adenocarcinoma cells MCF-7 (ER⁺) or MDA-231 (ER⁻) (Figure S4B). Knockdown of phosphatase and tensin homolog (PTEN) in MCF-7 cells increased PDHE1 phosphorylation in normoxia and, to a lesser extent, hypoxia, whereas

LN229 cells were unaffected (Figure S4C), suggesting that PTEN status may differentially affect hypoxia-stimulated mitochondrial Akt-PDK1 signaling depending on the tumor cell type.

To examine a more “physiologic” model of tumor hypoxia, we next looked at 3D cultures of patient-derived, stem cell-enriched GBM neurospheres (Di Cristofori et al., 2015). These cultures become hypoxic in their “core,” as determined by expression of a hypoxia probe (Figures 4A, S4D, and S4E). Under these conditions, GBM neurospheres exhibited strong phosphorylation of PDK1, as determined by immunofluorescence with pT346 Ab (Figure 4A). Conversely, differentiated GBM cells depleted of stem cells and growing as monolayers were normoxic, contained cytosolic HIF1 α , and did not react with pT346 Ab (Figure 4A). Pre-absorption of pT346 Ab with the immunizing peptide abolished reactivity with GBM (Figure S4D).

Next, we looked at Akt phosphorylation of PDK1 in primary, patient-derived GBM tissue samples (Table S2). GBMs with a high score (≥ 2) for nuclear HIF1 α showed increased phosphorylation of PDK1 by Akt (pT346 Ab), as well as phosphorylation of PDHE1 and Src, a major determinant of glioma invasiveness (Du et al., 2009), in hypoxic areas (Figures 4B and S4F). In contrast, GBMs with undetectable nuclear HIF1 α (score = 0) showed low to undetectable levels of PDK1-PDHE1 phosphorylation (Figures 4C and S4F). In these patients, phosphorylation of PDK1 (pT346 Ab) (Figure 4D) or PDHE1 phosphorylation (Figure 4E) correlated with expression of nuclear HIF1 α . Reciprocally, PDHE1 phosphorylation correlated with the expression of Akt-phosphorylated PDK1 (pT346 Ab) (Figure 4F), reinforcing a link between hypoxia and mitochondrial Akt-PDK1 phosphorylation in primary patient samples.

Mitochondrial Akt-PDK1 Regulation of Tumor Cell Proliferation in Hypoxia

To test a role of a mitochondrial Akt-PDK1 signaling in tumor growth in vivo, we first utilized human U251 GBM cells expressing a luciferase reporter under the control of a HIF1-responsive element (HRE) and a mCherry reporter under a constitutive phosphoglycerate kinase promoter to quantify cell viability. Stereotactic intracranial injection of these cells in immunocompromised mice gave rise to GBMs characterized by HIF1-directed luciferase activity and reactivity with a hypoxia-sensitive marker (Figures 5A and 5B). Despite low oxygenation, these orthotopic GBMs remained viable, as determined by high mCherry expression (Figures 5A and 5B), and exhibited a time-dependent increase in the number of mitotic tumor cells (Figure S5A). These proliferating cells stained intensely positive for Akt-phosphorylated PDK1 (Figures 5C, S5B, and S5C), correlating with increased HIF1 activity (Figure S5D). PDHE1 was also highly phosphorylated in intracranial GBMs (Figure 5C).

(I) PC3 cells in hypoxia were transduced with PDK1-directed shRNA, reconstituted with vector, WT PDK1, or the T346A PDK1 mutant cDNA and analyzed for PDH activity. Left, representative tracings (n = 3). Right, quantification of PDH activity. Mean \pm SEM. **p = 0.009.

(J) PC3 cells transduced with pLKO or PDK1-directed shRNA were reconstituted with vector, WT PDK1, or the T346A PDK1 cDNA and analyzed for glucose consumption (n = 4). Mean \pm SEM. ***p < 0.0002.

(K) PC3 cells in normoxia (N) or hypoxia (H) were treated with vehicle control (Veh) or Akt inhibitor, MK2206 (1 μ M), and analyzed for lactate production (n = 3). Mean \pm SEM. **p = 0.001–0.004, ***p = 0.0005–0.0009.

(L) PC3 cells in normoxia (N) or hypoxia (H) were transfected with control siRNA (Ctrl) or siRNA to Akt1 or Akt2 and analyzed for lactate production (n = 2). Mean \pm SD. **p = 0.004, ***p = 0.0005.

(M) PC3 cells stably silenced for PDK1 were transfected with vector (Vec), WT PDK1 or T346A PDK1 mutant, and analyzed for oxygen (O₂) consumption (n = 3). Mean \pm SEM. For all panels, data were analyzed using the two-sided unpaired Student's t tests. See also Figure S3.

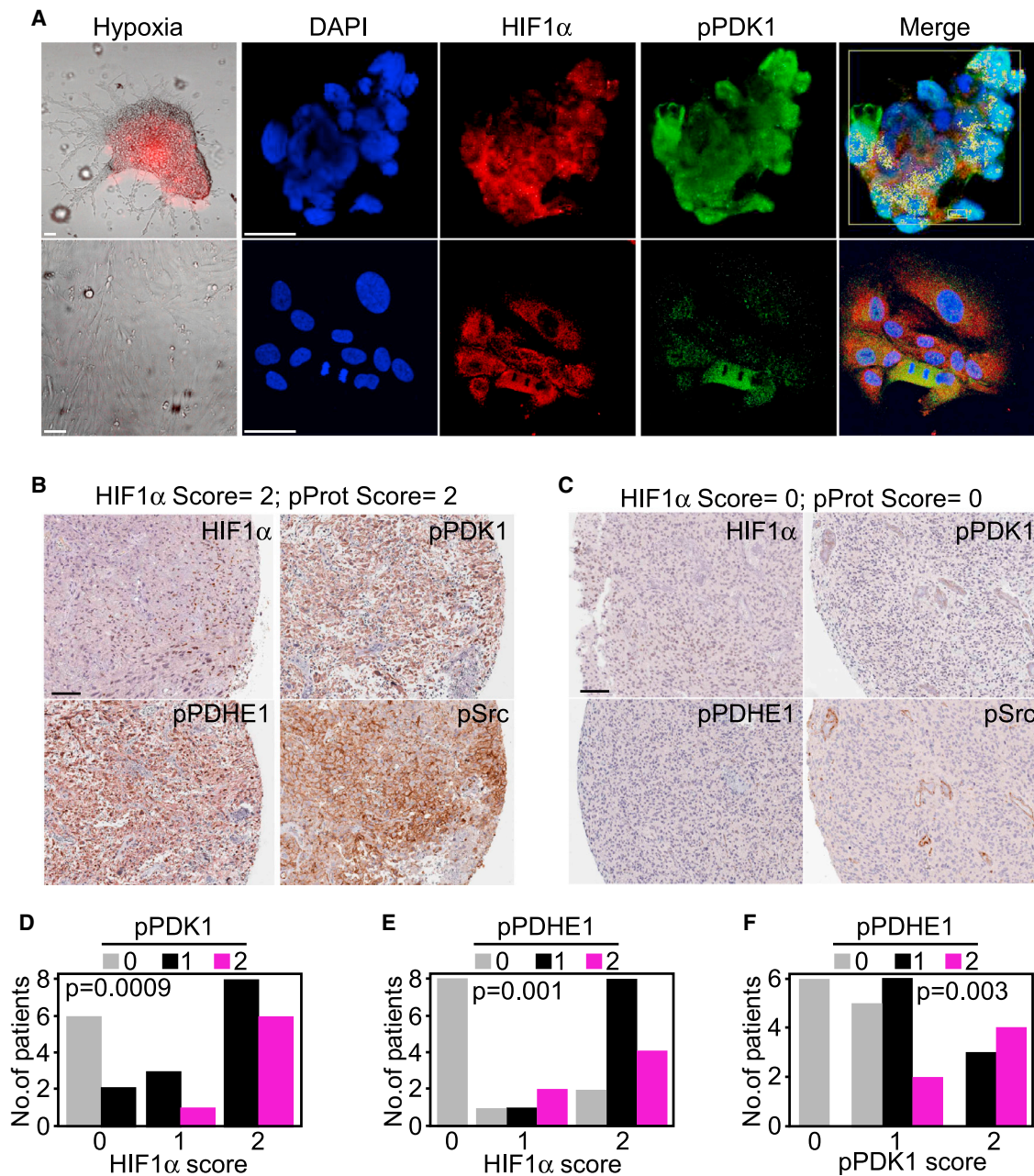


Figure 4. Mitochondrial Akt-PDK1 Phosphorylation In Vivo

(A) GBM neurospheres (top) or differentiated GBM cultures (bottom) were stained for DNA (DAPI), HIF1 α , pT346-phosphorylated PDK1, or hypoxia (hypoxia-sensitive probe). Merged images of nuclear-localized HIF1 α in hypoxic neurospheres (by velocity mask) are indicated (Merge). Yellow box, Velocity analysis to identify cells with nuclear HIF1 α in each single z stack. Scale bar, 20 μ m.

(B and C) Immunohistochemical staining of primary, patient-derived GBM samples with high (≥ 2) (B) or low (0) (C) score for HIF1 α and phosphorylated protein (pProt) expression. Scale bars, 100 μ m.

(D–F) Quantitative immunohistochemical correlation of patient-derived GBM samples (n = 24) or grade II gliomas (n = 2) for HIF1 α expression and pPDK1 (D) or pPDHE1 (E), or between pPDK1 and pPDHE1 (F). Four tissue microarray (TMA) cores/patient. The scoring is as follows: 0, no staining; 1, staining in at least one TMA core; 2, staining in ≥ 2 TMA cores. The individual p values per each analysis are indicated (chi-square test). See also Figure S4 and Table S2.

We next tested the requirement of mitochondrial Akt-PDK1 signaling in regulating proliferation under hypoxic conditions. siRNA knockdown of Akt1 or Akt2 (Figure 5D) or stable shRNA knockdown of PDK1 (Figure 5E) suppressed tumor cell proliferation in hypoxia. Normoxic cultures were partially affected (Fig-

ures 5D and 5E). When cells were analyzed for cell cycle transitions, MK2206 or the PDK1 inhibitor dichloroacetate suppressed S-phase progression in hypoxia and increased the population of tumor cells in G1/subG1 phase (Figure S5E). Finally, stable silencing of PDK1 abolished PC3 colony formation in hypoxia,

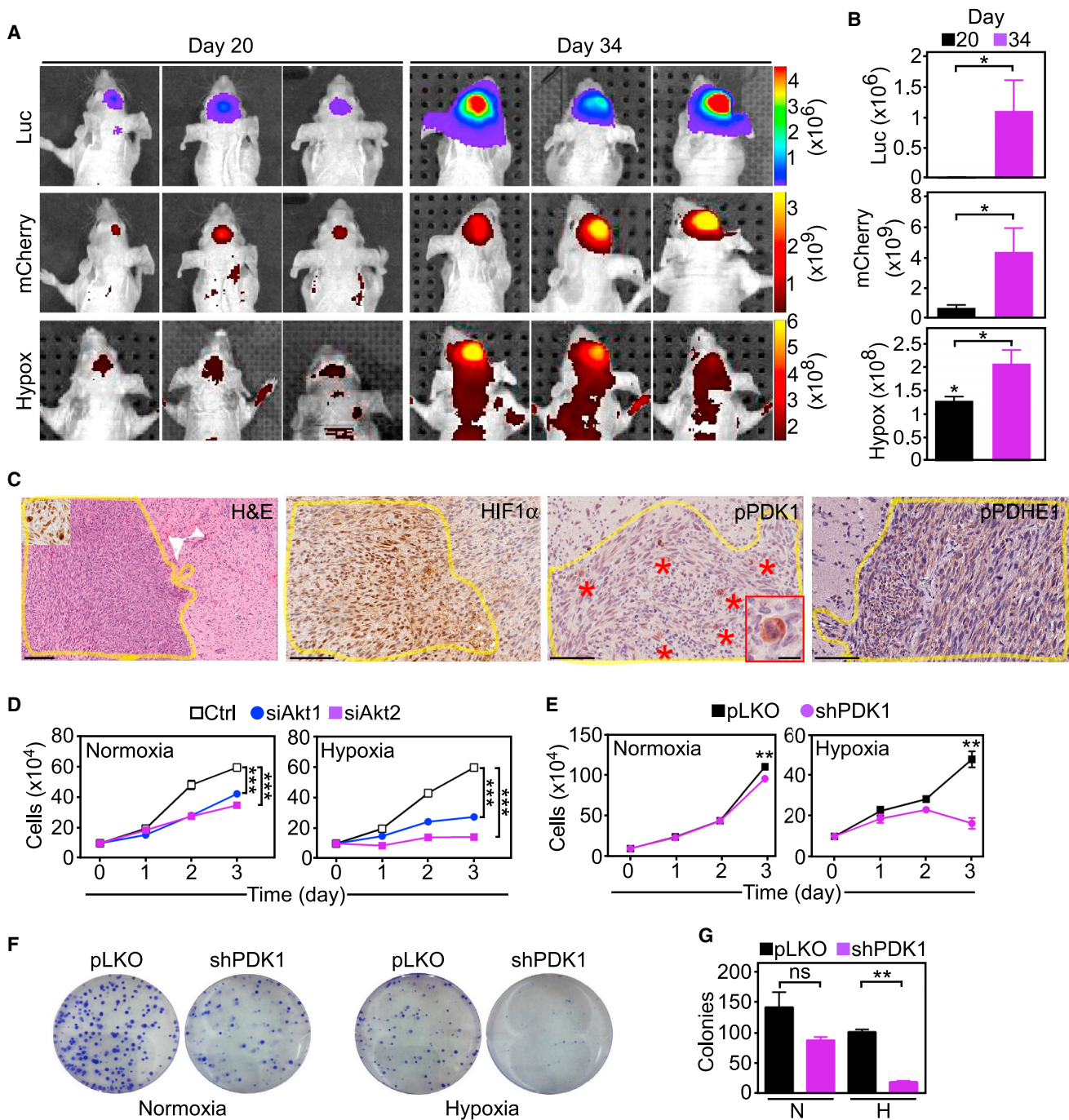


Figure 5. Requirement of Mitochondrial Akt for Tumor Cell Proliferation in Hypoxia

(A and B) Bioluminescence imaging of immunocompromised mice carrying U251 intracranial GBMs (three animals/group) expressing luciferase under the control of HIF1-responsive elements (Luc) and mCherry (cell viability) and exposed to a hypoxia-sensitive probe (Hypox). Scans were obtained at days 20 and 34 (A) and fluorescence signals were quantified (B). * $p = 0.016$ – 0.057 by Mann-Whitney test.

(C) Tissue samples from intracranial GBMs as in (A) were harvested at day 34 and analyzed for expression of HIF1 α , phosphorylated (p) PDK1 (pT346 Ab), or pPDHE1, by immunohistochemistry. Yellow lines were used to delineate the tumor mass within mouse brains. Scale bar, 100 μ m. Asterisks, mitotic cells; insets (H&E and pPDK1 panels), high-power magnification of mitotic cells. Scale bars, 25 μ m.

(D and E) PC3 cells transfected with control siRNA (Ctrl), Akt1- or Akt2-directed siRNA (D), or stably transduced with pLKO or PDK1-directed shRNA (E), were analyzed for cell proliferation in normoxia or hypoxia by direct cell counting ($n = 5$). Mean \pm SEM. *** $p < 0.001$, ** $p = 0.002$.

(F and G) PC3 cells stably transduced with pLKO or PDK1-directed shRNA were analyzed in normoxia or hypoxia for colony formation by crystal violet staining after 10 days (F) and quantified ($n = 3$) (G). Mean \pm SEM. ns, not significant. ** $p = 0.003$. For all panels, data were analyzed using the two-sided unpaired Student's t test. See also Figure S5.

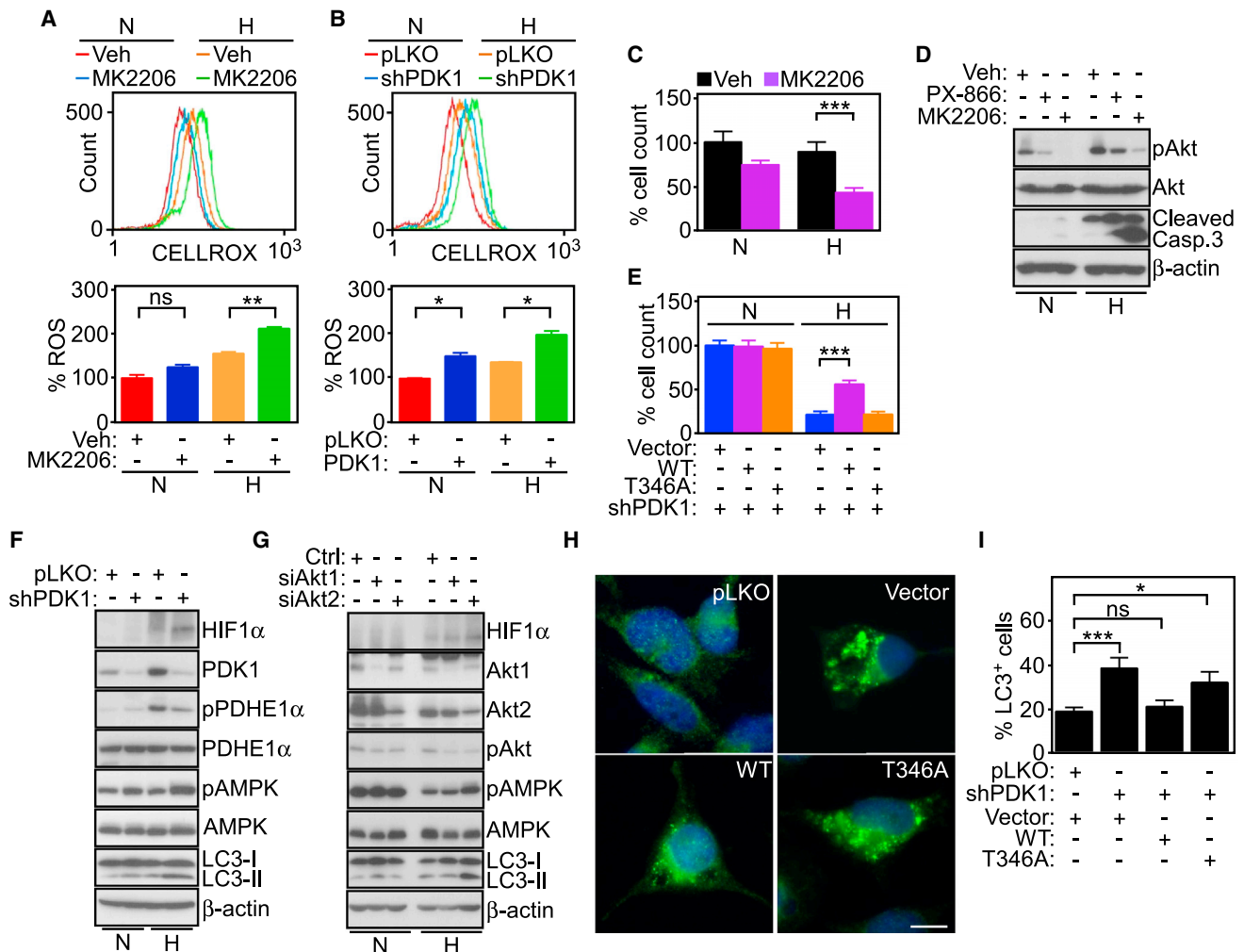


Figure 6. Mitochondrial Akt Regulation of Stress Signaling in Hypoxia

(A and B) PC3 cells in normoxia (N) or hypoxia (H) were treated with vehicle (Veh) or MK2206 (1 μ M) (A) or transduced with pLKO or PDK1-directed shRNA (B) and analyzed for ROS production by CellROX Green staining and flow cytometry. Upper panels, representative tracings. Bottom panels, quantification of ROS production under the various conditions tested (n = 2). Mean \pm SD for both datasets. *p = 0.01–0.02, **p = 0.004; ns, not significant.

(C) The experimental conditions are as in (A) and treated cells were analyzed for cell viability by direct cell counting relative to control (n = 3). Mean \pm SEM. ***p < 0.0001.

(D) PC3 cells in normoxia (N) or hypoxia (H) were incubated with vehicle (Veh) or small-molecule inhibitors of Akt (MK2206, 1 μ M) or PI3K (PX-866, 10 μ M) and analyzed by western blotting.

(E) PC3 cells stably silenced for PDK1 were reconstituted with vector, WT PDK1, or the T346A PDK1 mutant and analyzed for cell viability by direct cell counting relative to control (n = 3). Mean \pm SEM. ***p = 0.0002.

(F and G) PC3 cells in normoxia (N) or hypoxia (H) were transduced with pLKO or PDK1-directed shRNA (F), control siRNA (Ctrl), or Akt1- or Akt2-directed siRNA (G), and analyzed by western blotting.

(H and I) PC3 cells as in (E) were analyzed for LC3 reactivity by fluorescence microscopy. Scale bars, 10 μ m (H), and cells with LC3 puncta (>3) were quantified (n = 250–860 cells) (I). Mean \pm SEM. *p = 0.014, ***p = 0.0005; ns, not significant. For all panels, data were analyzed using the two-sided unpaired Student's t test. See also Figure S6.

a marker of tumorigenicity (Figures 5F and 5G), whereas normoxic growth was not significantly affected. Together, these data point to an important role of mitochondrial Akt-PDK1 signaling in maintaining tumor cell proliferation in hypoxia.

Mitochondrial Akt Regulation of Stress Signaling in Hypoxia

The downstream implications of defective mitochondrial Akt-PDK1 signaling were next investigated. First, inhibition of Akt

with MK2206 (Figure 6A) or stable shRNA silencing of PDK1 (Figure 6B) increased aberrant ROS production in tumor cells, especially in hypoxia. This was associated with decreased tumor cell viability (Figure 6C), and appearance of cleaved caspase 3 (Figure 6D), a marker of apoptosis. In normoxia, cleaved caspase 3 was undetectable. Confirming the specificity of this response, exposure of tumor cells to a small-molecule inhibitor of phosphatidylinositol 3-kinase (PI3K), PX-866, did not result in caspase activation (Figure 6D). Reconstitution of these cells with WT PDK1, but

not the T346A PDK1 mutant, partially rescued tumor cell viability in hypoxia (Figure 6E). Normoxic cultures were not affected, further supporting a role of PDK1 signaling selectively in hypoxia.

As a second downstream pathway of tumor maintenance modulated by bioenergetics, we next observed that stable knockdown of PDK1 (Figure 6F) or siRNA silencing of Akt1 or Akt2 (Figure 6G) in hypoxia increased the phosphorylation of the energy stress sensor, AMP-regulated kinase (AMPK). This response was associated with concomitant activation of autophagy, as determined by LC3 conversion to a lipidated form (Figures 6F and 6G) and punctate LC3 fluorescence staining (Figures 6H and 6I). Normoxic cultures showed a minimal level of autophagy induction after PDK1 silencing (Figures 6F, 6G, and S6A). In PDK1-depleted cells, re-expression of WT PDK1, but not the T346A PDK1 mutant, attenuated AMPK phosphorylation and reduced autophagy in hypoxia (Figures 6H, 6I, and S6B).

Requirement of Hypoxic Mitochondrial Reprogramming for Tumor Growth In Vivo

Next, we asked if mitochondrial Akt-PDK1 signaling was important for tumor growth in vivo. shRNA silencing of PDK1 significantly impaired the growth of PC3 xenograft tumors implanted in immunocompromised mice (Figure 7A). Re-expression of WT PDK1 in these cells restored tumor growth in vivo (Figures 7B and 7C), whereas the T346A PDK1 mutant further impaired tumor growth (Figure 7C). By immunohistochemistry, PC3 tumors harboring WT PDK1 showed increased cell proliferation, reduced apoptosis, and lower levels of autophagy compared with tumors reconstituted with the T346A PDK1 mutant (Figures 7D and 7E). In addition, tumors with loss of endogenous PDK1 showed a trend toward increased apoptosis and heightened autophagy in vivo, whereas tumor cell proliferation by Ki-67 staining was unchanged (Figures 7F and 7G). These results suggest that mitochondrial Akt-PDK1 signaling promotes tumor adaptation to hypoxia, and specifically enables continued tumor cell proliferation despite an unfavorable microenvironment (Figure 7H).

To test the relevance of this model in human cancer, we next looked at the prognostic impact of Akt phosphorylation of PDK1 in a clinically annotated cohort of 116 glioma patients (Table S3). Undetectable in normal brain parenchyma, the expression of Akt-phosphorylated PDK1 on T346 progressively increased in gliomas, with the highest reactivity observed in GBM (Figures 8A and 8B). PDK1 phosphorylation on T346 segregated with other markers of disease progression, including HIF1 α expression (Figure 8C), WT status of isocitrate dehydrogenase-1 (*IDH1*) (Figure 8D), and unmethylated O⁶-methylguanine-DNA methyltransferase (MGMT) promoter (Figure 8E). Consistent with this prognostic profile, elevated expression of Akt-phosphorylated PDK1, as determined by receiver operating characteristics (ROC) curves analysis (Figures S7A and S7B), was significantly associated with reduced overall survival in patients with gliomas ($p = 0.006$; hazard ratio [HR] = 2.2; 95% confidence interval [CI]: 1.17–4.12; Figure 8F) as well as patients with GBM ($p = 0.032$; HR = 2.03; 95% CI: 0.95–4.32; Figure 8G).

DISCUSSION

In this study, we have shown that hypoxia, a universal driver of malignancy, promotes the recruitment of active Akt to mitochondria

of tumor cells. In turn, mitochondrial Akt, in particular Akt2, phosphorylates the bioenergetics regulator PDK1 on a Thr346 target site, resulting in increased kinase activity and phosphorylation of its downstream substrate in the PDC, PDHE1 α . This pathway improves tumor fitness, stimulating glycolysis, countering autophagy and apoptosis, dampening oxidative stress, and enabling continued cell proliferation in face of severe hypoxia in vivo. Accordingly, mitochondrial Akt-PDK1 signaling emerged as a powerful negative prognostic factor in glioma patients, correlating with markers of unfavorable outcome and shortened survival.

Akt is an essential signaling node exploited in most cancers, integrating growth factor responses with mechanisms of cell proliferation, survival, and bioenergetics (Manning and Cantley, 2007). The role of this pathway as a regulator of tumor adaptation to hypoxia has not been previously described, and its spatial arrangement in subcellular compartments, in particular mitochondria, has only recently begun to emerge (Ghosh et al., 2015). Data presented here suggest that the recruitment of predominantly active Akt to mitochondria during hypoxia (Santi and Lee, 2010) may be part of a broader stress response in tumors, enabled by the chaperone function of cytosolic Hsp90 in mitochondrial preprotein import (Young et al., 2003) and mitochondrial ROS production, which may participate in subcellular trafficking of signaling molecules (Nakahira et al., 2006), including mitochondrial import (Fischer and Riemer, 2013).

In our phosphoproteomics screen, Akt recruitment to mitochondria was associated with a discrete Akt phosphorylation signature that included regulators of organelle homeostasis and glycolytic reprogramming in hypoxia, such as 6-phosphofructose-2-kinase/fructose-2,6-bisphosphatase 3 and PDK1 (De Bock et al., 2013). In the case of PDK1, Akt phosphorylation took place exclusively in hypoxia, did not involve other PDK isoforms, and targeted a unique Thr346 site in the “ATP lid” (Zhang et al., 2015), ideally positioned to affect ATP loading, and kinase activation (Patel et al., 2014). Thr346 did not affect PDK1 binding to the PDC, thus differently from another proposed post-translational modification of PDK1 involving Tyr phosphorylation of the “ATP lid” (Hitosugi et al., 2011).

Extensively studied as part of HIF1 signaling (Semenza, 2013), the tumor response to hypoxia has been linked to metabolic reprogramming (Kim et al., 2006; Papandreou et al., 2006), with suppression of mitochondrial respiration in favor of glycolysis (Denko, 2008). However, there is evidence that this pathway may extend well beyond bioenergetics, as PDK1 signaling has been implicated in senescence (Kaplon et al., 2013), metastatic tropism (Dupuy et al., 2015), and multiple mechanisms of tumor maintenance (McFate et al., 2008). The fact that this response is “druggable” and that small-molecule PDK1 inhibitors have entered clinical testing in cancer patients (Michelakis et al., 2010) adds to the relevance of PDK1 signaling as a potential driver of tumor progression.

Against this backdrop, the pathway of mitochondrial Akt-PDK1 signaling described here appears ideally poised to affect a plethora of downstream signaling mechanisms important for tumor adaptation and improved fitness. This involves suppression of apoptosis via mitochondrial Akt phosphorylation of hexokinase II at the outer membrane (Roberts et al., 2013) and cyclophilin D in the permeability transition pore (Ghosh et al., 2015), as

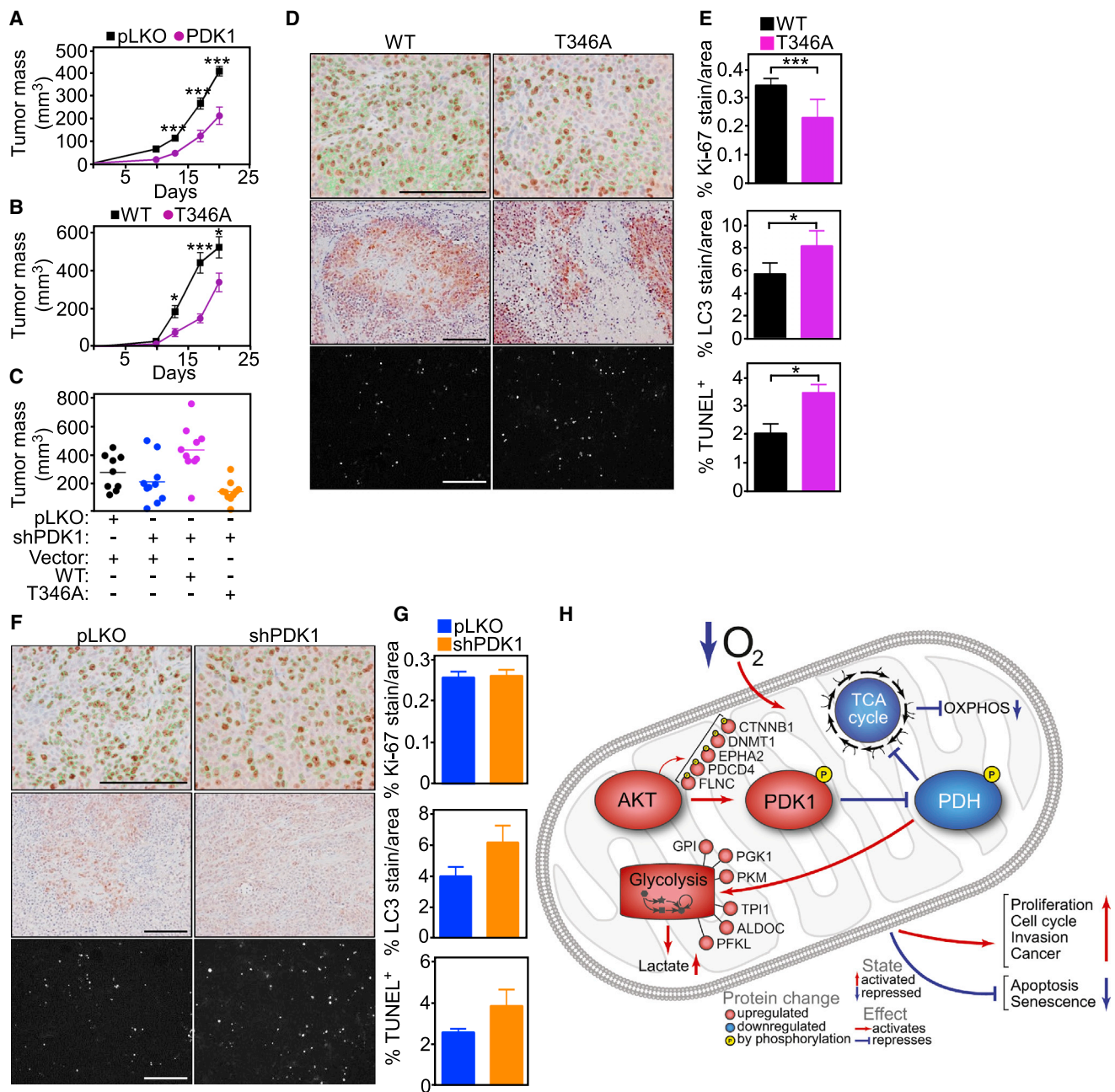


Figure 7. Mitochondrial Akt-Directed Hypoxic Reprogramming Supports Tumor Growth In Vivo

(A) PC3 cells transduced with pLKO or PDK1-directed shRNA were injected subcutaneously (s.c.) in the flanks of male NSG immunocompromised mice (three animals/group; two tumors/mouse), and superficial tumor growth was quantified with a caliper at the indicated time intervals for 20 days. Data were analyzed using the two-sided unpaired Student's t test. Mean \pm SEM. ***p < 0.0001.

(B) PC3 cells stably transduced with pLKO or PDK1-directed shRNA were reconstituted with WT PDK1 or the T346A PDK1 mutant and injected s.c. in the flanks of immunocompromised mice (five mice/group; two tumors/mouse). Tumor growth in the various groups was quantified at the indicated time intervals for 20 days. Data were analyzed using the two-sided unpaired Student's t test. Mean \pm SEM. *p = 0.01–0.02, ***p < 0.0001.

(C) PC3 cells stably transduced with pLKO or PDK1-directed shRNA were reconstituted with vector, WT PDK1, or the T346A PDK1 mutant and injected s.c. in immunocompromised mice with determination of tumor growth after 18 days. Each point corresponds to an individual tumor.

(D and E) Tumors harvested from the animals in (C) were analyzed for histology (D), and cell proliferation (top, Ki-67), autophagy (middle, LC3-II), or apoptosis (bottom, TUNEL) was quantified (E). The statistical analysis of the various groups by ANOVA is as follows: Ki-67, ***p < 0.0001; LC3, *p = 0.024; TUNEL, *p = 0.039. Scale bars, 100 μ m.

(F and G) Superficial flank tumors of PC3 cells transduced with control pLKO or PDK1-directed shRNA were harvested after 18 days and processed for immunohistochemistry (F) with quantification of reactivity for Ki-67 (top), LC3 (middle), or TUNEL (bottom) (H). Representative images per each condition are shown (n = 3, 10 images per mouse), Mean \pm SD. Scale bars, 100 μ m.

(H) Schematic model of a mitochondrial Akt-PDK1-PDH axis in hypoxic tumor reprogramming.

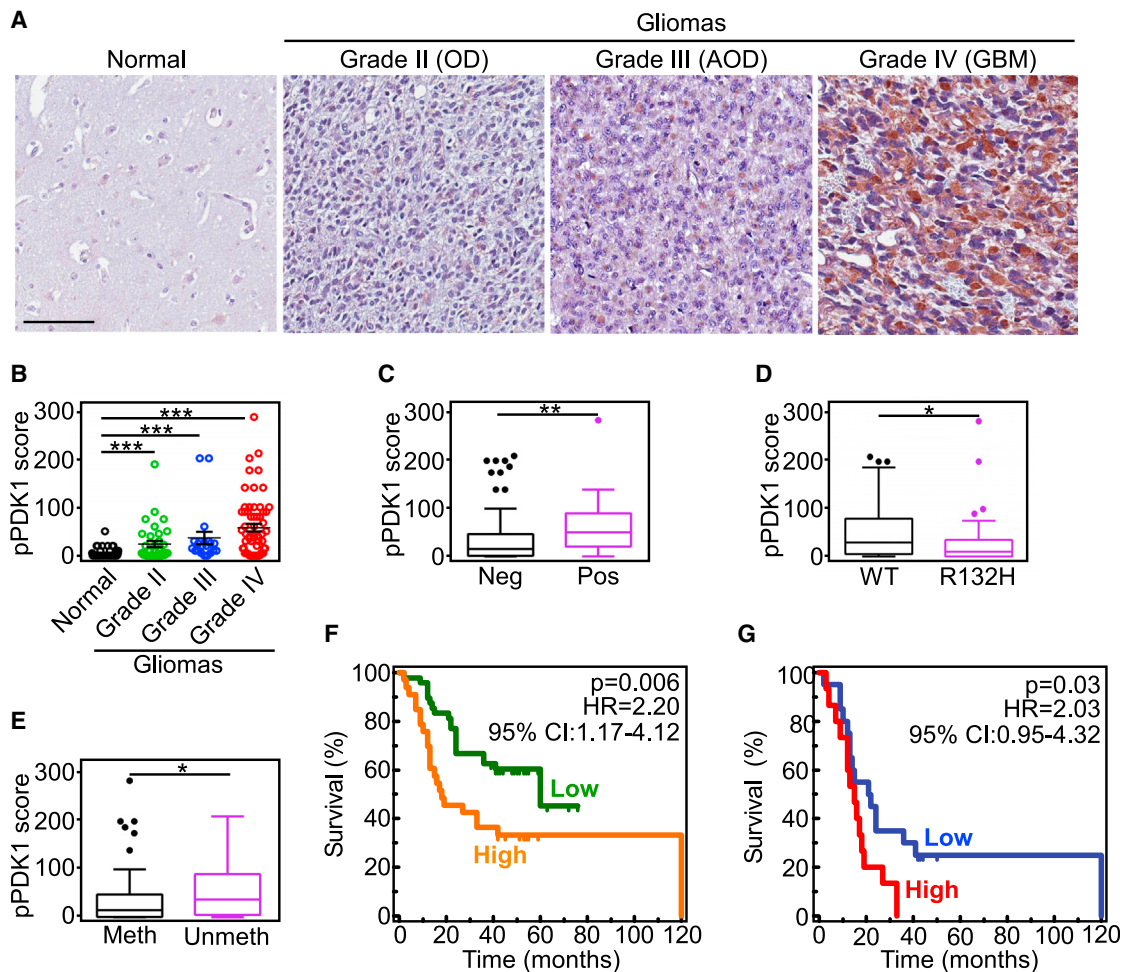


Figure 8. Mitochondrial Akt Phosphorylation of PDK1 Is a Negative Prognostic Marker in Human Gliomas

(A) Representative micrographs of immunohistochemical staining of non-neoplastic human brain parenchyma (normal) or grade II–IV gliomas (WHO classification) with PDK1 pT346 Ab. OD, oligodendroglioma; AOD, anaplastic OD. Scale bar, 100 μ m.

(B) Quantification of pT346 staining in a series of human brain tumors ($n = 116$) and 85 non-neoplastic brain parenchyma using a two-factor scoring system that considers the percentage of positive cells and the intensity of the staining (pPDK1 score). *** $p < 0.0001$ by Mann-Whitney U test. Each symbol represents an individual patient.

(C–E) Differences in pPDK1 score in human brain tumors as in (B) ($n = 116$) according to nuclear HIF1 α expression (C; ** $p = 0.008$ by Mann-Whitney U test), IDH1 mutation status (D; * $p = 0.02$ by Mann-Whitney U test), or MGMT promoter methylation (E; * $p = 0.01$ by Mann-Whitney U test). Data are presented as Tukey box-and-whisker plots. The bottom and top of the box represent the first and third quartiles, and the band inside the box represents the median (i.e., the second quartile). The bottom end of the whisker represents the lowest datum within the 1.5 interquartile range (IQR) of the lower quartile, and the top end of the whisker represents the highest datum within 1.5 IQR of the upper quartile. Outlier data, if any, are represented by single points.

(F and G) Kaplan-Meier curves were generated with either the complete series of glioma patients ($n = 116$; F) or with GBM cases only ($n = 61$; G) sorted into “Low” or “High” groups according to pPDK1 score. Cutoffs to rank patients in these two categories were generated using ROC curves and the Youden J statistic. Overall survival curves were compared using the log rank test. HR, hazard ratio; CI, confidence interval. See also Figure S7 and Table S3.

well as inhibition of oxidative phosphorylation through Akt phosphorylation of PDK1 and subsequent inhibition of the PDC (Patel et al., 2014). In turn, this lowers the production of toxic ROS, prevents the phosphorylation of the stress energy sensor, AMPK (Liang and Mills, 2013), and inhibits downstream activation of autophagy (White, 2012). Although these pathways have been implicated in both tumor suppression and oncogenesis (Liang and Mills, 2013; White, 2012), there is evidence that AMPK inhibition and suppression of autophagy may promote malignant expansion (White, 2012), and heightened metastatic competence (Caino et al., 2013), including in hypoxia (Liu et al., 2015),

further compounding the more aggressive traits of glycolytic tumors (Gatenby and Gillies, 2004).

Here, a pivotal feature of mitochondrial Akt-PDK1 signaling was its activation in mitotic cells and its requirement to support tumor cell proliferation in the face of hypoxia in vivo. Whether this response can be entirely attributed to the suppression of ROS or involves other mechanisms of mitochondria-to-nuclei retrograde signaling (Jazwinski, 2013) remains to be elucidated. On the other hand, hypoxic reprogramming may participate in cell cycle transitions via regulation of p27 expression (Gardner et al., 2001) or Myc transcriptional activity (Gordan et al.,

2007), and effector(s) of glycolysis have been linked selectively to chromosomal segregation and mitotic progression in hypoxia (Jiang et al., 2014). In line with the broad impact of mitochondrial Akt-PDK1 signaling on multiple mechanisms of tumor adaptation, this pathway was found to have significant implications for disease progression in humans. Accordingly, expression of PDK1 phosphorylated on T346 was undetectable in normal brain, but increased steadily in the hypoxic environment of gliomas, including GBMs, segregated with unfavorable prognostic markers, and was correlated with shortened overall survival in these patients. Although these results await further confirmation in larger patient cohorts, detection of Akt-phosphorylated PDK1 may provide an easily accessible biomarker for clinical decision making in patients with gliomas, including GBM (Wick et al., 2014).

Despite expectations for personalized, or precision medicine, small-molecule antagonists of Akt and its associated signaling nodes, PI3K and mammalian target of rapamycin (Manning and Cantley, 2007), have produced only limited responses in the clinical setting, hampered by drug resistance and significant toxicity (Fruman and Rommel, 2014). While these results may reflect mechanisms of tumor adaptation (Ghosh et al., 2015), including mitochondrial reprogramming (Caino et al., 2015), the identification of mitochondrial Akt (Ghosh et al., 2015) as a post-translational regulator of PDK1 activity and tumor progression may rationally repurpose Akt-directed molecular therapies as an approach to impair tumor adaptation to hypoxia. In this context, targeted inhibition of the mitochondrial pool of Akt may selectively disable a host of metabolic, survival, and proliferative requirements for tumor fitness (McFate et al., 2008) and reawaken endogenous tumor-suppressor mechanisms important for anticancer activity in patients.

EXPERIMENTAL PROCEDURES

Patients

All patient-related studies were reviewed and approved by an Institutional Review Board at Fondazione IRCCS, Ca' Granda Ospedale Maggiore Policlinico Milan, Italy. A first cohort of 26 patients diagnosed with de novo glioma were enrolled at Fondazione IRCCS Ca' Granda Ospedale Maggiore Policlinico (Milan, Italy) between 2010 and 2011, and described previously (Di Cristofori et al., 2015). All patients were treated with surgical resection with curative intent. Gliomas were staged according to the WHO classification (Louis et al., 2007), and the clinicopathologic and molecular characteristics of the patient series used in this study are described in Table S2. This cohort was used to evaluate the expression of phosphoT346-PDK1 (pPDK1), phosphoPDHE1 α (pPDHE1), phosphoT416-Src (pSrc), and nuclear HIF1 α reactivity, by immunohistochemistry. Tissue microarrays of glioma or normal brain tissues were carried out as described previously (Di Cristofori et al., 2015). Immunohistochemistry slides were digitalized using an Aperio scanner at 20 \times magnification, and HIF1 α nuclear staining was quantified using a nuclear-specific algorithm implemented in Genie Histology Pattern Recognition software (Aperio, Leica Microsystems). To specifically quantify nuclear HIF1 α expression in primary GBM culture, the Volocity algorithm that counts and displays red signals (HIF1 α) within the Hoechst signal (nuclei) in each z stack was used. A second series of 116 patients with de novo glioma who underwent surgery with curative intent between 2008 and 2009, and for whom complete clinical and follow-up records were available (Table S3), was retrieved from the archives of the Pathology Division. This cohort was used in the present study to correlate the expression of Akt-phosphorylated PDK1 on T346 with prognostic markers of glioma progression, including nuclear HIF1 α , MGMT promoter methylation and *IDH1* mutational status (WT/R132H), and patients' overall survival.

Xenograft Tumor Growth Studies

All experiments involving animals were approved by an Institutional Animal Care and Use Committee at The Wistar Institute in accordance with the Guide for the Care and Use of Laboratory Animals of the NIH, or, alternatively, at the University of Milan, in compliance with the Italian Ministry of Health. In a first set of experiments, PC3 cells stably transduced with control pLKO or PDK1-directed shRNA were reconstituted with vector, WT PDK1 or T346A PDK1 mutant cDNA at 80% confluency, suspended in PBS (pH 7.4), and injected (0.2 mL containing 2×10^6 cells) subcutaneously into the flank of 6–8-week-old male non-obese diabetic (NOD) severe combined immunodeficiency gamma (NSG, NOD.Cg-Prkdc^{scid} Il2rg^{tm1Wjl}/SzJ) immunocompromised mice (Jackson Laboratory, three mice per condition/two tumors per mouse). The width and length of superficial tumors were measured with a caliper at the indicated time intervals, and tumor volume was calculated according to the formula volume = width² \times length/2. After 21 days xenograft tumors were harvested, fixed, and processed for immunohistochemistry.

An orthotopic murine model of GBM was obtained by stereotactic injection (coordinates: 1.5 mm lateral to the bregma, 0 mm behind and 3.0 mm ventral to the dura) (Maes et al., 2009) of 1×10^5 U251-HRE-mCherry GBM cells in 2 μ L of PBS into 7–8-week-old female nude mice (Harlan Laboratories) at day 0 (Lo Dico et al., 2014). Following surgery, mice were monitored for recovery until complete awakening. Six animals per time point were used and mice were killed after 20 or 34 days. Intracranial GBM samples were harvested from the various groups and processed for differential expression of phosphorylated PDK1 or PDHE1, HIF1 α , or Ki-67 by immunohistochemistry on serial sections.

Statistical Analysis

Data were analyzed using the two-sided unpaired t or chi-square tests using a GraphPad software package (Prism 6.0) for Windows. Correlation parameters between immunohistochemical (IHC) scores in glioma patients and clinicopathologic variables were derived using Mann-Whitney U or chi-square tests for continuous or discrete variables, respectively, using GraphPad Prism or MedCalc statistical packages. The ROC curves method was used to test the accuracy of T346-phosphorylated PDK1 to correctly discriminate between glioma patients according to their survival status (alive or dead for the disease) and to generate cutoffs for phosphorylated PDK1 IHC score using the non-arbitrary criterion derived from the Youden J statistic (MedCalc Software) as described previously (Di Cristofori et al., 2015). The pPDK1 IHC score value that more accurately discriminated between patients who were alive or dead was >25 and >40 for glioma or GBM patients, respectively (Youden criterion). Glioma patients were then sorted into low- or high-expressor categories, and Kaplan-Meier survival curves were compared using the log rank test (MedCalc Software). Data are expressed as mean \pm SD or mean \pm SEM of replicates from a representative experiment out of at least two or three independent determinations. A p value of <0.05 was considered as statistically significant.

ACCESSION NUMBERS

The mass spectrometry proteomics data have been deposited in the MassIVE data repository (<http://massive.ucsd.edu>) and ProteomeXchange database (<http://www.proteomexchange.org>) with the accession numbers. MassIVE: MSV000079671 and ProteomeXchange: PXD004024.

SUPPLEMENTAL INFORMATION

Supplemental Information includes Supplemental Experimental Procedures, seven figures, and three tables and can be found with this article online at <http://dx.doi.org/10.1016/j.ccell.2016.07.004>.

AUTHOR CONTRIBUTIONS

Y.C.C. and D.C.A. conceived the project. Y.C.C., K.G.B., M.C.C., J.C.G., J.H.S., and S.L. performed experiments of Akt-PDK-PDHE1 phosphorylation, metabolic reprogramming, modulation of autophagy, mitochondrial localization, and cell proliferation and survival. I.B. and V.V. performed experiments with GBM neurospheres and patient-derived GBM samples. M.L. provided

primary, patient-derived GBM samples. L.O. performed experiments with an orthotopic mouse GBM model. H.Y.T. and D.W.S. performed proteomics experiments. B.K. performed molecular modeling of the PDK1 phosphorylation site. A.V.K. analyzed bioinformatics data of global phosphoproteomics and proteomics identification of PDK1 phosphorylation. S.B., L.R.L., D.W.S., and D.C.A. analyzed data, and Y.C.C., V.V., and D.C.A. wrote the paper.

ACKNOWLEDGMENTS

This work was supported by the NIH grants P01 CA140043 (D.C.A. and L.R.L.), R01 CA78810 and CA190027 (D.C.A.), R01 CA089720 (L.R.L.), F32CA177018 (M.C.C.), the Office of the Assistant Secretary of Defense for Health Affairs through the Prostate Cancer Research Program under Award No. W81XWH-13-1-0193 (D.C.A.), and a Challenge Award from the Prostate Cancer Foundation (PCF) to M.C.C., L.R.L., and D.C.A. V.V. is supported by an award from Fondazione Cariplo (2014-1148) and L.O. is supported by FP7-INSERT project (HEALTH-2012-INNOVATION-1, GA305311). I.B. is supported by a fellowship from the Doctorate School of Molecular and Translational Medicine at the University of Milan, Italy. Support for Core Facilities utilized in this study was provided by Cancer Center Support Grant CA010815 to The Wistar Institute.

Received: August 19, 2015

Revised: March 4, 2016

Accepted: July 1, 2016

Published: August 8, 2016

REFERENCES

- Caino, M.C., Chae, Y.C., Vaira, V., Ferrero, S., Nosotti, M., Martin, N.M., Weeraratna, A., O'Connell, M., Jernigan, D., Fatatis, A., et al. (2013). Metabolic stress regulates cytoskeletal dynamics and metastasis of cancer cells. *J. Clin. Invest.* 123, 2907–2920.
- Caino, M.C., Ghosh, J.C., Chae, Y.C., Vaira, V., Rivadeneira, D.B., Favarsani, A., Rampini, P., Kossenkova, A.V., Aird, K.M., Zhang, R., et al. (2015). PI3K therapy reprograms mitochondrial trafficking to fuel tumor cell invasion. *Proc. Natl. Acad. Sci. USA* 112, 8638–8643.
- Cox, T.R., Rumney, R.M., Schoof, E.M., Perryman, L., Hoye, A.M., Agrawal, A., Bird, D., Latif, N.A., Forrest, H., Evans, H.R., et al. (2015). The hypoxic cancer secretome induces pre-metastatic bone lesions through lysyl oxidase. *Nature* 522, 106–110.
- De Bock, K., Georgiadou, M., Schoors, S., Kuchnio, A., Wong, B.W., Cantelmo, A.R., Quaegebeur, A., Ghesquiere, B., Cauwenberghs, S., Eelen, G., et al. (2013). Role of PFKFB3-driven glycolysis in vessel sprouting. *Cell* 154, 651–663.
- Denko, N.C. (2008). Hypoxia, HIF1 and glucose metabolism in the solid tumour. *Nat. Rev. Cancer* 8, 705–713.
- Di Cristofori, A., Ferrero, S., Bertolini, I., Gaudioso, G., Russo, M.V., Berno, V., Vanini, M., Locatelli, M., Zavanone, M., Rampini, P., et al. (2015). The vacuolar H⁺ ATPase is a novel therapeutic target for glioblastoma. *Oncotarget* 6, 17514–17531.
- Du, J., Bernasconi, P., Clauser, K.R., Mani, D.R., Finn, S.P., Beroukhi, R., Burns, M., Julian, B., Peng, X.P., Hieronymus, H., et al. (2009). Bead-based profiling of tyrosine kinase phosphorylation identifies SRC as a potential target for glioblastoma therapy. *Nat. Biotechnol.* 27, 77–83.
- Dupuy, F., Tabaries, S., Andrzejewski, S., Dong, Z., Blagih, J., Annis, M.G., Omeroglu, A., Gao, D., Leung, S., Amir, E., et al. (2015). PDK1-dependent metabolic reprogramming dictates metastatic potential in breast cancer. *Cell Metab.* 22, 577–589.
- Fischer, M., and Riemer, J. (2013). The mitochondrial disulfide relay system: roles in oxidative protein folding and beyond. *Int. J. Cell Biol.* 2013, 742923.
- Fruman, D.A., and Rommel, C. (2014). PI3K and cancer: lessons, challenges and opportunities. *Nat. Rev. Drug Discov.* 13, 140–156.
- Gardner, L.B., Li, Q., Park, M.S., Flanagan, W.M., Semenza, G.L., and Dang, C.V. (2001). Hypoxia inhibits G1/S transition through regulation of p27 expression. *J. Biol. Chem.* 276, 7919–7926.
- Gatenby, R.A., and Gillies, R.J. (2004). Why do cancers have high aerobic glycolysis? *Nat. Rev. Cancer* 4, 891–899.
- Ghosh, J.C., Siegelin, M.D., Vaira, V., Favarsani, A., Tavecchio, M., Chae, Y.C., Lisanti, S., Rampini, P., Giroda, M., Caino, M.C., et al. (2015). Adaptive mitochondrial reprogramming and resistance to PI3K therapy. *J. Natl. Cancer Inst.* 107, <http://dx.doi.org/10.1093/jnci/dju502>.
- Gilkes, D.M., Semenza, G.L., and Wirtz, D. (2014). Hypoxia and the extracellular matrix: drivers of tumour metastasis. *Nat. Rev. Cancer* 14, 430–439.
- Gordan, J.D., Bertout, J.A., Hu, C.J., Diehl, J.A., and Simon, M.C. (2007). HIF-2alpha promotes hypoxic cell proliferation by enhancing c-myc transcriptional activity. *Cancer Cell* 11, 335–347.
- Graeber, T.G., Osmanian, C., Jacks, T., Housman, D.E., Koch, C.J., Lowe, S.W., and Giaccia, A.J. (1996). Hypoxia-mediated selection of cells with diminished apoptotic potential in solid tumours. *Nature* 379, 88–91.
- Hitosugi, T., Fan, J., Chung, T.W., Lythgoe, K., Wang, X., Xie, J., Ge, Q., Gu, T.L., Polakiewicz, R.D., Roesel, J.L., et al. (2011). Tyrosine phosphorylation of mitochondrial pyruvate dehydrogenase kinase 1 is important for cancer metabolism. *Mol. Cell* 44, 864–877.
- Hockel, M., and Vaupel, P. (2001). Tumor hypoxia: definitions and current clinical, biologic, and molecular aspects. *J. Natl. Cancer Inst.* 93, 266–276.
- Jazwinski, S.M. (2013). The retrograde response: when mitochondrial quality control is not enough. *Biochim. Biophys. Acta* 1833, 400–409.
- Jiang, Y., Li, X., Yang, W., Hawke, D.H., Zheng, Y., Xia, Y., Aldape, K., Wei, C., Guo, F., Chen, Y., et al. (2014). PKM2 regulates chromosome segregation and mitosis progression of tumor cells. *Mol. Cell* 53, 75–87.
- Kaplon, J., Zheng, L., Meissl, K., Chaneton, B., Selivanov, V.A., Mackay, G., van der Burg, S.H., Verdegaa, E.M., Cascante, M., Shlomi, T., et al. (2013). A key role for mitochondrial gatekeeper pyruvate dehydrogenase in oncogene-induced senescence. *Nature* 498, 109–112.
- Keith, B., Johnson, R.S., and Simon, M.C. (2012). HIF1alpha and HIF2alpha: sibling rivalry in hypoxic tumour growth and progression. *Nat. Rev. Cancer* 12, 9–22.
- Kim, J.W., Tchernyshyov, I., Semenza, G.L., and Dang, C.V. (2006). HIF-1-mediated expression of pyruvate dehydrogenase kinase: a metabolic switch required for cellular adaptation to hypoxia. *Cell Metab.* 3, 177–185.
- Liang, J., and Mills, G.B. (2013). AMPK: a contextual oncogene or tumor suppressor? *Cancer Res.* 73, 2929–2935.
- Liu, X.D., Yao, J., Tripathi, D.N., Ding, Z., Xu, Y., Sun, M., Zhang, J., Bai, S., German, P., Hoang, A., et al. (2015). Autophagy mediates HIF2alpha degradation and suppresses renal tumorigenesis. *Oncogene* 34, 2450–2460.
- Lo Dico, A., Valtorta, S., Martelli, C., Belloli, S., Gianelli, U., Tosi, D., Bosari, S., Degrossi, A., Russo, M., Raccagni, I., et al. (2014). Validation of an engineered cell model for in vitro and in vivo HIF-1alpha evaluation by different imaging modalities. *Mol. Imaging Biol.* 16, 210–223.
- Louis, D.N., Ohgaki, H., Wiestler, O.D., Cavenee, W.K., Burger, P.C., Juvet, A., Scheithauer, B.W., and Kleihues, P. (2007). The 2007 WHO classification of tumours of the central nervous system. *Acta Neuropathol.* 114, 97–109.
- Maes, W., Deroose, C., Reumers, V., Krylyshkina, O., Gijssbers, R., Baekelandt, V., Ceuppens, J., Debyser, Z., and Van Gool, S.W. (2009). In vivo bioluminescence imaging in an experimental mouse model for dendritic cell based immunotherapy against malignant glioma. *J. Neurooncol.* 91, 127–139.
- Manning, B.D., and Cantley, L.C. (2007). AKT/PKB signaling: navigating downstream. *Cell* 129, 1261–1274.
- Mazumdar, J., O'Brien, W.T., Johnson, R.S., LaManna, J.C., Chavez, J.C., Klein, P.S., and Simon, M.C. (2010). O2 regulates stem cells through Wnt/beta-catenin signalling. *Nat. Cell Biol.* 12, 1007–1013.
- McFate, T., Mohyeldin, A., Lu, H., Thakar, J., Henriques, J., Halim, N.D., Wu, H., Schell, M.J., Tsang, T.M., Teahan, O., et al. (2008). Pyruvate dehydrogenase complex activity controls metabolic and malignant phenotype in cancer cells. *J. Biol. Chem.* 283, 22700–22708.
- Michalakakis, E.D., Sutendra, G., Dromparis, P., Webster, L., Haromy, A., Niven, E., Maguire, C., Gammer, T.L., Mackey, J.R., Fulton, D., et al. (2010). Metabolic modulation of glioblastoma with dichloroacetate. *Sci. Transl. Med.* 2, 31ra34.

- Nakahira, K., Kim, H.P., Geng, X.H., Nakao, A., Wang, X., Murase, N., Drain, P.F., Wang, X., Sasidhar, M., Nabel, E.G., et al. (2006). Carbon monoxide differentially inhibits TLR signaling pathways by regulating ROS-induced trafficking of TLRs to lipid rafts. *J. Exp. Med.* 203, 2377–2389.
- Papandreou, I., Cairns, R.A., Fontana, L., Lim, A.L., and Denko, N.C. (2006). HIF-1 mediates adaptation to hypoxia by actively downregulating mitochondrial oxygen consumption. *Cell Metab.* 3, 187–197.
- Patel, M.S., Nemeria, N.S., Furey, W., and Jordan, F. (2014). The pyruvate dehydrogenase complexes: structure-based function and regulation. *J. Biol. Chem.* 289, 16615–16623.
- Ravi, R., Mookerjee, B., Bhujwalla, Z.M., Sutter, C.H., Artemov, D., Zeng, Q., Dillehay, L.E., Madan, A., Semenza, G.L., and Bedi, A. (2000). Regulation of tumor angiogenesis by p53-induced degradation of hypoxia-inducible factor 1alpha. *Genes Dev.* 14, 34–44.
- Roberts, D.J., Tan-Sah, V.P., Smith, J.M., and Miyamoto, S. (2013). Akt phosphorylates HK-II at Thr-473 and increases mitochondrial HK-II association to protect cardiomyocytes. *J. Biol. Chem.* 288, 23798–23806.
- Santi, S.A., and Lee, H. (2010). The Akt isoforms are present at distinct subcellular locations. *Am. J. Physiol. Cell Physiol.* 298, C580–C591.
- Semenza, G.L. (2013). HIF-1 mediates metabolic responses to intratumoral hypoxia and oncogenic mutations. *J. Clin. Invest.* 123, 3664–3671.
- Tredan, O., Galmarini, C.M., Patel, K., and Tannock, I.F. (2007). Drug resistance and the solid tumor microenvironment. *J. Natl. Cancer Inst.* 99, 1441–1454.
- White, E. (2012). Deconvoluting the context-dependent role for autophagy in cancer. *Nat. Rev. Cancer* 12, 401–410.
- Wick, W., Weller, M., van den Bent, M., Sanson, M., Weiler, M., von Deimling, A., Plass, C., Hegi, M., Platten, M., and Reifenberger, G. (2014). MGMT testing—the challenges for biomarker-based glioma treatment. *Nat. Rev. Neurol.* 10, 372–385.
- Young, J.C., Hoogenraad, N.J., and Hartl, F.U. (2003). Molecular chaperones Hsp90 and Hsp70 deliver preproteins to the mitochondrial import receptor Tom70. *Cell* 112, 41–50.
- Zhang, S.L., Hu, X., Zhang, W., Yao, H., and Tam, K.Y. (2015). Development of pyruvate dehydrogenase kinase inhibitors in medicinal chemistry with particular emphasis as anticancer agents. *Drug Discov. Today* 20, 1112–1119.